# Statistical Physics of Structural Design

Daniel Rayneau-Kirkhope, MSci

Thesis submitted to the University of Nottingham

for the degree of Doctor of Philosophy

May 2012

# Abstract

In this thesis, problems of structural optimisation are approached through analytic and computational techniques. A particular focus is the effect of hierarchical design.

The first chapter forms an introduction for the reader. Chapter 2 investigates the optimisation of elastic support on a buckling rod. A cost function is associated with the strength of the total elastic support provided to a beam of uniform cross-section supporting a compressive load. Through a perturbative method, it is found that for a low cost of support, a single, centrally placed support is optimal; furthermore it is found, using simulational and analytic methods, that the optimal support placement undergoes a series of bifurcations as the cost increases. The nature of these bifurcations is non-trivial and, although the analogy is not complete, there exist similarities between the solution to this problem and Landau theory of second-order phase transitions.

In Chapter 3, the theme of hierarchical design is introduced. By analysing all possible failure modes, it is shown that a hierarchical design is highly efficient for withstanding external pressure loading in the limit of low applied pressures. By changing the level of hierarchy, the scaling law for volume of material required for structural stability against the applied external pressure can be changed systematically. For a given applied pressure, a particular level of hierarchy is shown to be optimal. This optimal level of hierarchy increases without bound as the

pressure decreases. The Hausdorff dimension of the optimal structure and its dependence on applied pressure is found. Two example structures are presented, although the design is applicable to any convex shape.

The fourth chapter of this thesis investigates the use of hierarchical geometry for a highly efficient interface between two surfaces. It is proposed that for a given strength of surface interaction, alterations to the geometry of the interface play a strong role in determining the force that is required to separate the surfaces. In particular the case of two surfaces with one being very much more rigid than the second is investigated. Increasing the hierarchical order of the design is seen to change the scaling relationship between the interface interaction strength and failure load.

In Chapter 5, a hierarchical design for high mechanical efficiency under compressive loading is fabricated and mechanically tested. The particular design has previously been shown to be highly efficient under compressive loading. The scaling of material required to build a stable structure against a specific loading has previously been shown to be dependent on the level of hierarchy. A second order design is fabricated using rapid prototyping techniques. Additionally, a similar design based on hollow tubes rather than solid beams is proposed and is shown to make further savings on volume when compared to the original design.

The final investigation presented in this thesis focuses on the role of imperfections in determining the buckling load of a hierarchical design. A two-dimensional design is proposed before simple, single beam, imperfections are added to the structure. The dependence of the structure on the magnitude of the imperfections is calculated analytically for the generation-1 and 2 designs. In the generation-1 structure, the magnitude of the imperfection is related to the reduction in failure load by a one-half power-law. The behaviour of a generation-2 frame with a single beam perturbed in thickness is found to be dominated by the behaviour of the

generation-1 subframe. The behaviour found analytically is confirmed with finite element simulations for the generation-1 structure.

# Acknowledgements

Firstly, I would like to thank the EPSRC for financial support during the time spent as postgraduate at the University of Nottingham. Further funding for collaborative work in Chapter 5 was from the 'Bridging the Gaps' scheme at the University of Nottingham.

The thesis presented here would not have come to fruition had it not been for the support of my supervisors, Dr. Yong Mao and Dr. Robert Farr. Your guidance has always been appreciated.

The work presented here is interdisciplinary in nature, I count myself lucky to have worked closely with Dr. Cyril Rauch and Dr. Joel Segal on work presented in Chapters 4 and 5 respectively. I have also worked with numerous students: I would like to thank David Neal and Guang Yang who have undertaken physics projects with me and also Ranbir Singh and Fred Grillet who have worked on related engineering projects.

My time at the University of Nottingham would not have been the same without a number of people. Mary, Jen, Chris and Paul; Ed, Nick, Nick and Chris; Chris, Angus, Rich and Fajer and many more besides helped make my stay here long and enjoyable.

The postgraduate physics department football team, 'Dave Jephcotes XI', deserves special mention; I hope the team continues for a long time to come. Duncan, Lucy, James, Hector, Pete, Andy and Fintan have all contributed sig-

nificantly to my enjoyment of the last few years.

My family are a constant source of support in my life, my brothers, sisters, parents, step-parents, grand-parents and nephews have always been appreciated (even you, Ben).

Finally, without Arianna Casiraghi the last few years would not have been complete, thank you.

# Contents

# Chapter 1

# Introduction

From the first man-made structure dating back to the ice age, structural stability has presented man with all things from shelter from his environment, transportation of goods to methods of worshipping God. The construction of taller and more sophisticated structures have been a recurrent theme throughout history. Geometric precision unrivalled to this day is evident in ancient buildings such as the Parthenon in Athens demonstrating care and attention to dimensional accuracy [1]. Evidence of buildings in excess of ninety metres tall dating back thousands of years B.C. [2] and stunning medieval cathedrals with intricate arches and vaulted ceilings are testament to craftsmanship and understanding through the ages. It is then perhaps surprising that the first recorded scientific approach to problems of strength and stability was undertaken by da Vinci (1492-1519) [1].

While understanding of structures failing under tension can be traced back to Galileo [1, 3] (1564-1576) who found load at breaking to be proportional to the cross sectional area, the understanding of elastic failure under compression is attributed to Euler in 1759 [4]. Though his work was thought to be of academic interest only when it was first conceived [5], the "Euler load" now forms a fundamental tool in the understanding of how much material is required to support a

given load under compression [5]. It is from his work that the understanding of efficiency and optimisation of simple structures under compression can be framed [1].

Perhaps the most striking examples of structural optimisation are to be found within nature [5, 6, 7]. Acting over vast time-scales, evolution has found some of the most beautiful engineering solutions with intricacy that cannot be matched even by modern fabrications techniques. Examples of highly complex architecture, constructed to achieve specific physical properties are numerous: the tendon as an efficient tension bearing linkage [8], bone as a structural scaffold [9] and the cellulose aggregates in wood for structural stability [10], to name but a few. The functionality of all of these examples are dependent on hierarchical architectures [6]: the structure at one lengthscale is dependent on a substructure of a smaller lengthscale (this substructure may or may not have an internal, non-trivial substructure). The evolution of these designs has, in part, been in response to having a relatively limited range of materials available [10], for example biological tissues are primarily proteinaceous while natural rigid structures tend to be constructed from calcium carbonates, calcium phosphates and silica [10].

It is not just in nature that hierarchical structures are found as complex, highly efficient solutions to engineering problems. Hierarchical laminates are known to give extremal values of strength and stiffness [6, 11]; structural hierarchy can even be manipulated to give unusual material properties such as negative Poisson's ratio [12]. One widely cited example of a man-made hierarchical structure is the Eiffel Tower [6]: stability here is clearly dependent on a non-trivial substructure, which itself has two further levels of ordered hierarchy [13]. It is through this design that a remarkably low effective density of material is achieved [6]. Although the primary consideration may have been the ease of construction, Mandelbrot amongst others, postulated that Eiffel perceived the structural advantage [13, 14].

In 1966 Freeman Dyson presented an argument that hierarchical frameworks could be used in creating highly efficient, large scale structures in outer space [15]. Although hierarchical architecture was not at the centre of his study, Mikulus put forward further works on structural optimisation for outer space stiff frameworks [16]; one general conclusion of Mikulus' work was that the individual loading requirements on the component members of such a framework were very low when compared to earth based structures. It is in this regime of low loading that hierarchical designs could be the most efficient [17].

Within almost every type of engineering structure, beam-columns under axial compression are found [18]. It is often the case that the stability of these columns is fundamental to the stability of the structure. Thus, suppression of the buckling modes in a loaded beam-column is of fundamental importance to a multitude of structures we rely on every day [5]. One method of suppressing these buckling modes is to use rigid supports along the length of the column. This problem has been studied in depth and optimal positions for rigid supports have been found [19]. Furthermore, the minimum stiffness of a given distribution of supports which give the same buckling load as the rigid equivalent can be obtained [19, 20]. General numerical approaches for any number of deformable supports have also been studied [21] as have numerical methods for continuous distributions of elastic support [22]. Work focusing on the effect of one centrally placed elastic support has been undertaken revealing its effect on buckling load and post-buckling form [23]. In Chapter 2 of this thesis, the optimisation of position and stiffness of elastic support is studied further. A cost function is associated with the total stiffness of the elastic support (which can be either continuous or discrete in its distribution). The problem is formulated such that the distribution which leads to the highest buckling load of the beam for a given cost is desired. While for low values of total support, it is found that a single, centrally placed support is

optimal, bifurcations in the optimal placement of elastic support are found for higher values of cost. Analytical expressions for both the failure loading and the optimal distribution are found in the vicinity of the first bifurcation point. In addition, numerical simulations are undertaken to confirm these findings and investigate the regime of higher support costs.

In Chapter 3, the principle of self similar, hierarchical design is introduced. This principle is found throughout nature [6] and can be utilised to construct highly efficient structures under various loading conditions [17, 24, 25, 26].

The optimisation procedure utilised in Chapter 3, as with similar works, is that of naïve optimisation [27], making the assumption that the optimal structure is such that the failure of all component parts is simultaneous [28]. Despite the possibility of high sensitivity to imperfections for structures designed under such assumptions [29], optimisations of this nature are extremely useful as a theoretical bound. The particular problem investigated in Chapter 3 is that of the minimum amount of material that is required to build a structure stable under a given external pressure. The design is applicable to arbitrary convex shapes and illustrated with two examples. It is shown that the scaling of material required for stability against external pressure applied can be varied systematically. The optimal number of hierarchical levels is found to vary with the applied external pressure. It is shown that in the limit of low pressure the design becomes fractal and the fractal dimension of such structures is found.

The problem investigated in Chapter 4 is one of adhesion. A simple model is presented which describes an interaction between a deformable surface and an infinitely stiff surface via a specific interfacial interaction. The adhesion between two materials of differing stiffness is an important one in nature; natural composites of organic materials mixed with hard minerals are found to create materials with beneficial properties [30]. In some cases, the fracture toughness is found to

be three or four orders of magnitude greater than that of the single crystal of pure minerals [30]. This combination is also found to increase capacity of recovery after deformation [31]. The problem investigated here is one of designing a robust adhesion geometry for two materials of vastly differing stiffness. In particular the geometry investigated is inspired by an adhesive interface found in nature fixing the stiff equine hoof wall to soft organic material in a robust manner [32, 33]. This adhesion mechanism must not only support the weight of the horse but also the impulse bought about through locomotion [32]. Its robustness is central to equine health. A hierarchical geometry is defined using lamella as a structural feature recurrent on different length scales. A structural advantage is found with increasing hierarchical order when the interaction strength is small compared to the stiffness of the deformable surface.

In Chapter 5 an example structure is fabricated using rapid prototyping technologies. The frame constructed has previously been analysed theoretically [17] and it has been shown that the scaling of material required to create a stable structure under a given compressive force can be altered in a systematic way. Here, mechanism maps are created for generation-1 and 2 structures showing the active failure mode for a given geometry giving an intuitive insight into the optimisation procedure. The fabricated example structure is then mechanically tested before the results are compared to those obtained through finite element models and theoretical calculations. Furthermore, a design based on hollow tubing is presented which shows a further gain in efficiency when compared with a structure made from solid beams.

For hierarchical structures to be practical, the sensitivity of these structures to imperfections must be understood. This is the subject matter of the sixth chapter of this thesis. A 2-dimensional hierarchical model is introduced which shows highly efficient scaling of material for stability against applied loading.

Imperfections are then introduced into the system and are analysed using both analytic and computational methods. The imperfections considered are small perturbations to a single beam thickness. When these perturbations are introduced in a generation-1 structure the drop in failure load is related to the magnitude of the imperfection by a one-half power law. It is found analytically that for small imperfection magnitude, the effect of strengthening is equivalent to that of weakening the individual beam: in both cases it brings about a reduction in failure load. In the case of the generation-2 structure, the effect of a single perturbation is dominated by its affect on the generation-1 substructure. Again, a one-half power law is found. The case of the generation-1 structure with a single imperfection is investigated through computational means and good agreement is found with analytic predictions.

The aims of this thesis are to develop understanding into the optimisation of structural design and in particular the role of hierarchy in structural optimisation. A conventional optimisation of a single beam under compressive loading is undertaken before hierarchical designs are presented for three distinct loading situations; this illuminates the particular behaviour of the design principle and shows underlying trends. In order to assess the practicality of such designs and limitations of current manufacturing techniques an example hierarchical structure is fabricated and mechanically tested. Furthermore, to address the theoretical limits of applicability, the effect of single beam imperfections are investigated through analytic and simulation techniques.

# Chapter 2

# Bifurcations in the optimal elastic foundation for a buckling column

## 2.1 Introduction

In this chapter, a simply supported beam, of uniform cross section and subject to a compressive load applied at its end points, is considered. As early as 1759 it was shown by Euler that the beam will buckle when the loading reaches a critical value [4]. In the problem presented here, the buckling will be suppressed by a restoring force applied perpendicular to the beam's length which will be provided by an elastic foundation. It is of practical interest to investigate, for a given amount of elastic support, the best distribution of this foundation for the suppression of buckling.

A simple, intuitive case is illustrated in Fig. 2.1(a), where the restoring force is provided by a discrete set of springs, each with a given spring constant. These springs will provide a restoring force, proportional to the magnitude of the lateral

displacement of the beam. This model can be generalised by considering the elastic foundations to be spread over the beam's length. This case is illustrated in Fig. 2.1(b), where the elastic foundation is now described by a spring constant per unit length, which can be varied along the beam.

Before considering the optimisation procedure, a cost function for the elastic support is introduced. In the case of a discrete set of springs, this cost function is taken to be the sum of the spring constants, or, in the case of the continuous distribution, the integral of the spring constant per unit length over the whole of the beam. The optimisation procedure can thus be stated: for a given cost of elastic support, what distribution of elastic support will support the maximal load?

The effect of a centrally placed elastic support has been established [18, 23], it is found the effect can be summarised in three points: first, up to a given value of support strength, increasing the support strength increases the buckling load; secondly, above this value of support stiffness, the buckling load is unaffected by further increases; thirdly, the shape of the failed beam is dependent on the elastic support. Furthermore, optimisation of position for one or two infinitely stiff supports have been considered [19]. In contrast to these studies however, the work presented here in principle permits any distribution of elastic foundation.

Here, it is shown that, in the limit of weak support, the optimal distribution is a simple delta function placed at the centre of the beam. For greater values of support cost, a transfer matrix description for the beam with supports concentrated as delta functions at given positions is introduced. Numerically it is found that the optimal distribution of support undergoes a series of bifurcation events. Analytic expressions are obtained for the buckling load in the vicinity of the first bifurcation point, and a corresponding expression for the optimal placement of elastic support is found. The similarities between the nature of this bifurcation

event and those found in Landau theory of second order phase transitions [34] are compelling. The analogy is not complete however, there are important differences in the nature of the solution to the two problems, namely, the free energy in Landau theory is a smooth function of the order parameter and the control variable, while in our case the function analogous to free energy is non-analytic at certain points. The results of this analytic work are found to agree with those of numerical work.

## 2.2 Theory

A slender beam of length $L$, aligned with the $\tilde{x}-$axis, with simply supported ends, subjected to a compressive load, $F$, and with lateral force per unit length, $q(\tilde{x})$, is governed by the equation [21]:

$$YI\frac{d^4\tilde{y}}{d\tilde{x}^4} + F\frac{d^2\tilde{y}}{d\tilde{x}^2} = q(\tilde{x}), \tag{2.1}$$

where $\tilde{y}$ is the lateral displacement, $I$ is the second moment of area, $Y$ is the Young's Modulus of the material, $\tilde{x}$ is the distance along the beam. The end points of the beam are freely hinged, thus the boundary conditions $\tilde{y} = \tilde{y}'' = 0$ at $\tilde{x} = 0$ and $\tilde{x} = L$. Stating the elastic nature of our support explicitly, $q(\tilde{x})$ can be written,

$$q(\tilde{x}) = -k(\tilde{x})\tilde{y}(\tilde{x}). \tag{2.2}$$

Then, defining the non-dimensional quantities, $y \equiv \pi\tilde{y}/L$, $x = \pi\tilde{x}/L$, $f = FL^2/(YI\pi^2)$ and $\rho = k(\tilde{x})L^4/(YI\pi^4)$, Eq (2.1) becomes,

$$\frac{d^4y}{dx^4} + f\,\frac{d^2y}{dx^2} + \rho(x)y = 0 \quad \text{for} \quad x \in (0, \pi), \tag{2.3}$$

the boundary conditions become, $y(0) = y(\pi) = y''(0) = y''(\pi) = 0$, and $\rho(x)$ represents the strength of the elastic support at position $x$.

For a given distribution of elastic support Eq. (2.3) has a set of eigenvalues which represents the buckling loads for the beam being described. Of greatest engineering importance however is the minimum of these values, which will be denoted $f_{\min}$; it is this value that will be maximised through our choice of function for $\rho(x)$. For example, modelling a beam with no elastic foundation ($\rho = 0$) it can be shown that Eq. (2.3) has the solutions $f \in \mathbb{Z}^+$, and therefore buckling would occur when $f = 1$, or $F = \pi^2 YI/L^2$, the so called Euler limit of loading. Lateral support can be shown to increase the stability of the beam, increasing the value of $f_{\min}$. A constraint for the amount of this reinforcement that can be applied to the beam is introduced,

$$m \equiv \int \rho(x)\, dx, \tag{2.4}$$

and the problem can be fully defined: for a given value of $m$ what is the maximal value of $f_{\min}$ that can be obtained through optimisation of $\rho$?

The simplest choice that can be imagined is that $\rho$ takes the uniform value $m/\pi$, so that the form of deflection is $y(x) \propto \sin kx$, for some integer $k$, which represents a wave-number. This leads immediately to the result that in this case

$$f_{\min} = \min_{k \in \mathbb{Z}} \left[ k^2 + \frac{m}{\pi k^2} \right]. \tag{2.5}$$

Eq. (2.5) has a physical interpretation: the first term comes from the free buckling of the column which is most unstable to buckling on the longest allowed length scales (i.e. the smallest values of $k$), as demonstrated by Euler. The second term represents the support provided by the elastic foundation, which provides

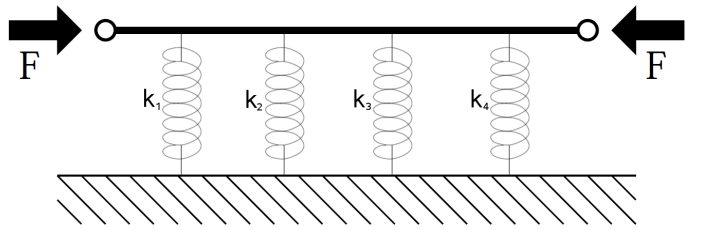


(a)

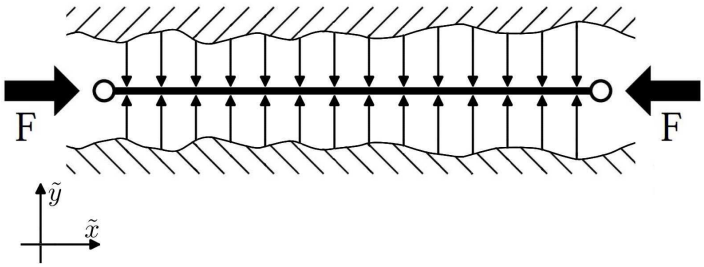


(b)

Figure 2.1: Schematic of a slender beam with elastic support, loaded under compression force $F$. (a) shows the case where the lateral restoring force per unit length along the beam $q(\tilde{x})$ is provided by linear springs of spring constant $\{k_i\}$ at discrete points $\{\tilde{x}_i\}$, so that $q(\tilde{x}) = \sum_{i=1}^{4} k_i \delta(\tilde{x} - \tilde{x}_i)\tilde{y}/L$. (b) shows schematically the case where there is a continuous support: the lengths of the arrows indicate the local spring constant.

the least support at the shortest length scales (largest values of $k$). The balance between these two terms means that as $m \to \infty$, the uniformly supported column buckles on a length scale of approximately

$$l_{\text{eff}} \approx (\pi/m)^{1/4} \quad \text{as} \quad m \to \infty, \tag{2.6}$$

and can support a load

$$f_{\text{uni}} \sim 2\sqrt{m/\pi}. \tag{2.7}$$

Now, although a uniform elastic support is easy to analyse, it is clear that this is not always optimal. Consider the case where $m$ is very small, so that $\rho$ provides a small correction in Eq. (2.3). In this case, the eigenvalues remain well-separated; the equation can be treated perburbatively: let

$$y = y_0 \sin x + y_1(x) \quad \text{and} \quad f = 1 + f_1, \tag{2.8}$$

then from Eq. (2.3), $\sin x$ (the lowest unperturbed eigenfunction) can be used as a multiplication factor and on integrating, it is found to leading order:

$$\int_0^\pi \left\{ \sin x \left[ \frac{d^4 y_1}{dx^4} + \frac{d^2 y_1}{dx^2} \right] + y_0 \sin^2 x \, [\rho - f_1] \right\} \mathrm{d}x = 0. \tag{2.9}$$

Repeated integrations by parts with the boundary conditions $y_1'' = 0$ at $x = 0, \pi$ establishes the self-adjointness of the original operator, and it is found that,

$$f_1 = \frac{2}{\pi} \int_0^\pi \rho(x) \sin^2 x \, \mathrm{d}x. \tag{2.10}$$

Therefore it is seen that in the limit $m \to 0$, the optimal elastic support is

$\rho(x) = m\delta(x - \pi/2)$, and for this case, $f_{\min} = 1 + (2m/\pi) + O(m^2)$.

The requirement for optimal support has therefore concentrated the elastic foundation into a single point, leaving the remainder of the beam unsupported.

## 2.3 Transfer Matrix formulation

Having shown that for small values of $m$ the optimal support distribution is one central delta function, higher values of $m$ can then be investigated through the examination of the case of $N-1$ delta functions placed at positions $\{x_n\}$. In the general formulation each spring constant takes an independent value of $\beta$, thus, to describe the system the set $\{\beta_n\}$ must be defined, the sum of which is $m$:

$$\rho(x) = \sum_{n=1}^{N-1} \beta_n \delta(x - x_n) \tag{2.11}$$

$$m = \sum_{n=1}^{N-1} \beta_n \tag{2.12}$$

This discrete set of supports divide the beam into $N$ segments, between these discrete positions, the Euler-Bernoulli Equation [Eq. (2.3)] with $\rho(x) = 0$ governs the deflection of the beam. This equation can be solved and thus, it is found that for $x \in (x_n, x_{n+1})$ the solution is given by:

$$y(x) = A_n \sin[f^{1/2}(x - x_n)] + B_n \cos[f^{1/2}(x - x_n)] + C_n(x - x_n) + D_n. \tag{2.13}$$

For convenience, $x_0 \equiv 0$ and $x_N \equiv \pi$ are defined. Integrating Eq. (2.3) over a small interval around $x_n$, it is found that,

$$\lim_{x \to x_n^+} y(x) = \lim_{x \to x_n^-} y(x), \qquad \lim_{x \to x_n^+} y'(x) = \lim_{x \to x_n^-} y'(x) \tag{2.14}$$

$$\lim_{x \to x_n^+} y''(x) = \lim_{x \to x_n^-} y''(x), \qquad \lim_{x \to x_n^+} y'''(x) - \lim_{x \to x_n^-} y'''(x) = \beta_n y(x_n) \tag{2.15}$$

Defining $\mathbf{v}_n \equiv (A_n, B_n, C_n, D_n)^T$, these continuity constraints on the piecewise solution of Eq. (2.13) can be captured in a transfer matrix

$$\mathbf{v}_n = T_n \cdot \mathbf{v}_{n-1}, \tag{2.16}$$

where $T_n$ is given by

$$\begin{pmatrix} \frac{\beta_n}{f^{3/2}} S_n + K_n & \frac{\beta_n}{f^{3/2}} K_n - S_n & \frac{\beta_n}{f^{3/2}} \Delta x_n & \frac{\beta_n}{f^{3/2}} \\ S_n & K_n & 0 & 0 \\ -\frac{\beta_n}{f} S_n & -\frac{\beta_n}{f} K_n & 1 - \frac{\beta_n}{f} \Delta x_n & -\frac{\beta_n}{f} \\ 0 & 0 & \Delta x_n & 1 \end{pmatrix} \tag{2.17}$$

where,

$$\begin{aligned} \Delta x_n &\equiv x_n - x_{n-1} \\ S_n &\equiv \sin[f^{1/2}(x_n - x_{n-1})], \\ K_n &\equiv \cos[f^{1/2}(x_n - x_{n-1})]. \end{aligned}$$

At the two end-points ($x = 0,\ \pi$), the boundary conditions state that $y$ and $y''$ vanish, this leads to the following four conditions

$$B_0 = D_0 = 0 \tag{2.18}$$

$$A_{N-1} S_N + B_{N-1} K_N = 0 \tag{2.19}$$

$$C_{N-1}(x_N - x_{N-1}) + D_{N-1} = 0. \tag{2.20}$$

Defining a matrix

$$\mathbf{R} = T_{N-1} T_{N-2} \ldots T_2 T_1 \tag{2.21}$$

then Eqs. (2.18 - 2.20) lead to

$$\mathbf{M} \cdot \begin{pmatrix} A_0 \\ \\ C_0 \end{pmatrix} = 0 \tag{2.22}$$

where

$$\mathbf{M} \equiv \begin{pmatrix} R_{11}S_N + R_{21}K_N & R_{13}S_N + R_{23}K_N \\ (\Delta x_N)R_{31} + R_{41} & (\Delta x_N)R_{33} + R_{43} \end{pmatrix} \tag{2.23}$$

The value of $f$ for which the beam will buckle, will be the smallest value such that either $A_0$ and/or $C_0$ take non-zero values. Simple linear mathematics dictates that this can only be achieved, while Eq. (2.23) is satisfied, if the determinant of $\mathbf{M}$ is zero. Thus, the maximum load which the beam can support before buckling is the smallest value of $f$, $f_{\min}$, at which $\det(\mathbf{M}) = 0$.

## 2.4 Equally spaced, equal springs

Before approaching the full optimisation problem the solution to a relatively simple distribution of springs is investigated, namely, $N-1$ equally strong springs, placed at regular intervals along the beams length. This will provide a lower bound on the solution of $f_{\min}$, and also provide us with insight into the problem. For this distribution, $\rho$ takes the form:

$$\rho_N(x) = \sum_{n=1}^{N-1} \frac{m}{N-1} \delta(x - \pi/n). \tag{2.24}$$

Through the transfer matrix formulated above, for a given $m$ it is straight-forward to obtain the lowest value for $f$ for which the initial configuration of the beam will be unstable. The results of these calculations are shown in Fig. 2.2. In general,

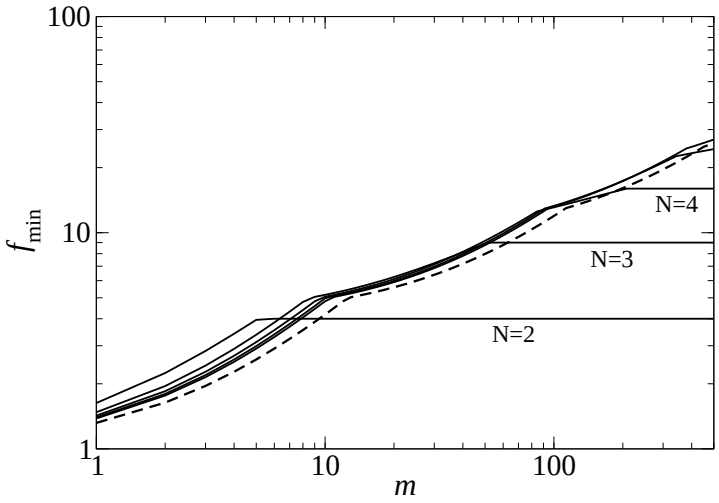


Figure 2.2: Value of $f_{\min}$ for $\rho$ constant (dashed line), and for equally spaced, equally strong delta functions ($N$ is the number of intervals, so $N-1$ is the number of delta-functions).

it is found that concentrating the supports into few supports is beneficial rather than spread the elastic support into a uniform support. It is seen that, for a given $N$, there is a threshold value of $m$, such that further increases in stiffness no longer yield increases in $f_{\min}$. For any finite value of $N$, there will be a buckling mode with $f = N^2$ that takes the value $y = 0$ at all points where $\rho(x)$ is non-zero. Thus, once this buckling mode is excited (or equivalently once $f > N^2$), further increasing $m$ will have no effect on $f_{\min}$.

## 2.5 Numerical optimisation of the support

A further, restricted problem can be investigated giving understanding of the interaction of the buckling beam with elastic support. Here the optimal set $\{x_n\}$ for a given number of equally strong supports is obtained. Thus:

$$\beta_n = \frac{m}{N-1} \quad \forall \quad n \tag{2.25}$$

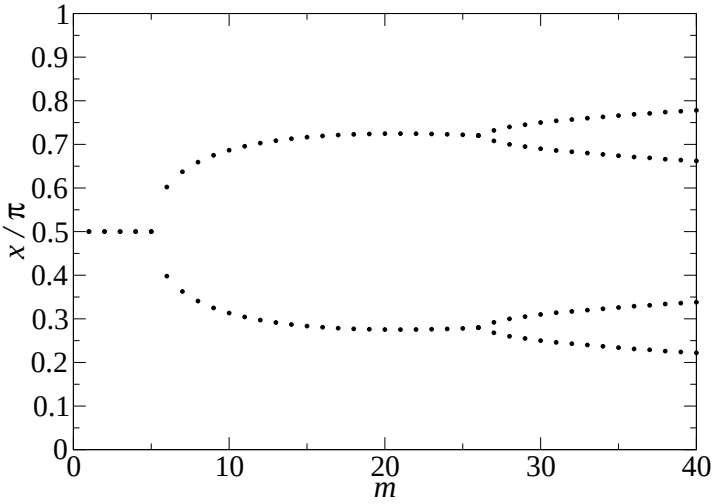


Figure 2.3: Results of the restricted optimisation, obtaining the set of positions, $\{x_n\}$, with constant $\beta_n = m/(N-1)$.

and the set $\{x_n\}$ which maximises $f_{min}$ is desired. A coarse-grained search was performed involving the evaluation of $f_{\min}$ for a set of design variables spanning the entire range of all parameters to establish the topology of the search environment; assuming continuity of the variable $f_{\min}$ the search boundaries were then refined before repeating the search with a finer variation of parameters. The results of this search are shown in Fig. 2.3, where two bifurcation points in the range $0 < m \leq 40$ are observed. A critical exponent, $\alpha$, of these bifurcation events can be defined through the expression,

$$x - x_0 = (m - m_0)^{\alpha}, \tag{2.26}$$

where $x$ is the optimal position for a given cost $m$, $x_0$ is the optimal position at the point of bifurcation which occurs at support cost $m_0$. The critical exponent of each has been obtained through simulation as,

$$\alpha_1 = 0.5 \pm 0.01, \tag{2.27}$$

$$\alpha_2 = 0.49 \pm 0.03, \tag{2.28}$$

for the first and second bifurcation respectively. Fig. 2.4 shows the data from which the exponents are taken, where values of $m_0$ and $x_0$ used are,

$$m_0 = 5.09,\ 26.99 \tag{2.29}$$

$$x_0 = 0.5,\ 0.281 \tag{2.30}$$

for the first and second bifurcation respectively. The value of $x_0$ for the lower branching event at $m = 26.99$ is related to the upper branch by symmetry about the midpoint of the beam. As discussed previously, the optimal solution must split further at higher values of $m$. Relaxing the restriction on all supports being equally stiff, the full optimisation problem is reached, that of finding the values $\{\beta_i\}$ as well as the positions $\{x_i\}$ which maximise $f_{\min}$. Using the transfer matrix the optimal elastic support using delta functions is found. Fig. 2.5 shows the best solutions, found using the search technique described above for four delta functions ($N = 5$), up to $m = 50$. It is seen in Fig. 2.6 that there are two bifurcation events, and one coalescence of the branches in the range $0 \leq m \leq 50$. It can be shown that for large $m$ there cannot be regions of of the beam with length greater than $m^{-1/4}$ with $\rho = 0$ [35], thus, in some sense for higher $m$ the support distribution becomes more evenly distributed. It is hypothesised that this transition to a more uniform distribution occurs through a series of bifurcation events.

## 2.6 First branch point

As has been shown, the optimal support distribution in the limit of small $m$ is a single delta function placed at $x = \frac{\pi}{2}$. However, numerical results indicate (see Fig. 2.6) that at some point the optimal distribution of $\rho$ bifurcates. This

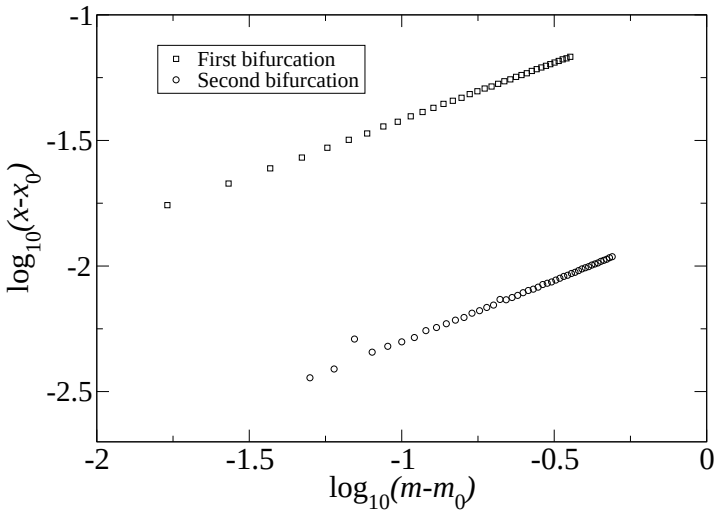


Figure 2.4: Showing the critical exponents for the first and second bifurcation in the restricted problem of $\beta_n = m/(N-1)$.

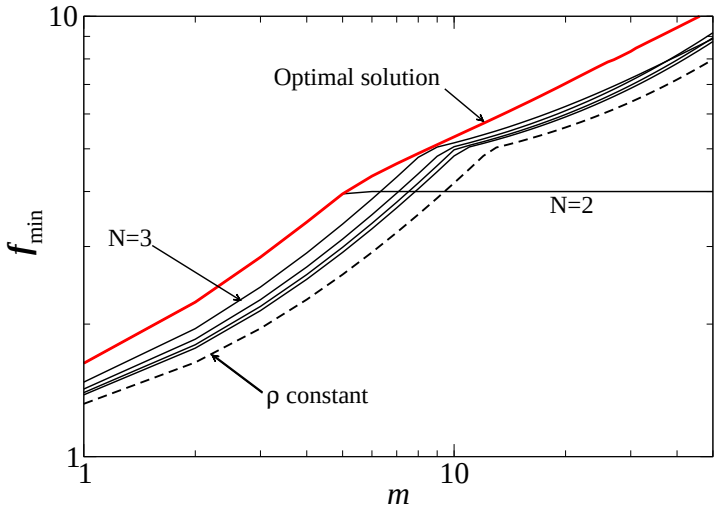


Figure 2.5: Value of $f_{\min}$ for the optimal form of $\rho(x)$ and also for comparison $\rho$ constant, and for equally spaced, equally strong delta functions.

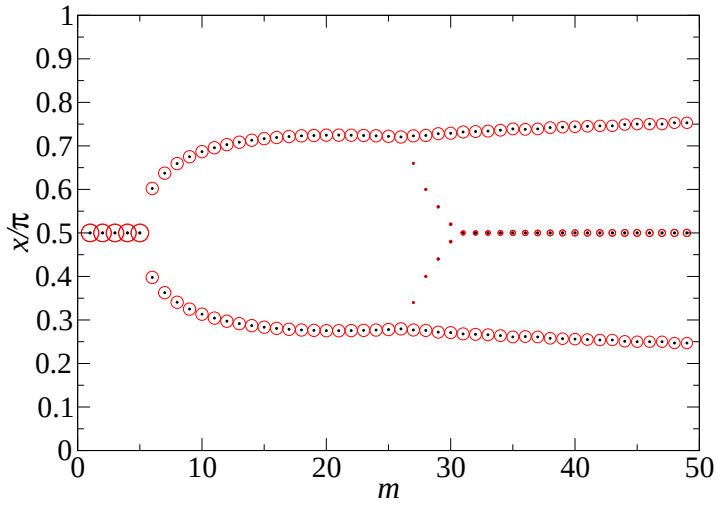


Figure 2.6: Position of optimal springs as a function of $m$. The area of each circle is proportional to the strength $\beta_i$ of the relevant support, with the total area of all the circles at each value of $m$ chosen to be a constant, independent of $m$.

bifurcation must occur at $f = 4$ because that is the point at which the first anti-symmetric mode is excited and further increases in $m$ yield no increase in buckling load. Despite the value of $f$ being clear at this point, the values of $m$ is not clear.

In order to clarify the behaviour at this first branch point, a perturbative expansion is performed: let us suppose that $N = 3$ and

$$\rho(x) = \frac{m}{2}\delta\left(x - \frac{\pi}{2} + \xi\right) + \frac{m}{2}\delta\left(x - \frac{\pi}{2} - \xi\right), \tag{2.31}$$

where $\xi$ and $-\xi$ are clearly equivalent, only the positive value will be quoted in later notation. Thus $\{x_0, x_1, x_2, x_3\}$ are given by $\{0, \pi/2 - \xi, \pi/2 + \xi, \pi\}$ and $\beta_1 = \beta_2 = m/2$. The matrix $\mathbf{M}$ in Eq. (2.23) must be evaluated and the smallest $f$ giving a zero determinant is desired. On performing a series expansion of the determinant for $f$ near 4, it is found that the critical value of $m$ is $16/\pi$.

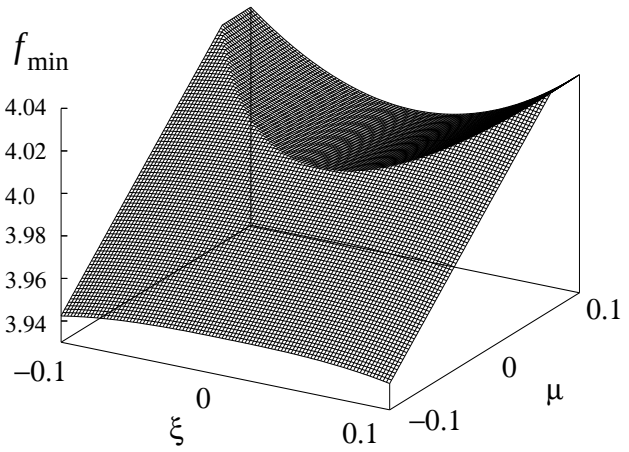


Figure 2.7: Three dimensional plot of $f_{\min}$ as a function of the position parameter $\xi$ and $\mu \equiv m - (16/\pi)$.

Furthermore, the small quantities $\mu$ and $\xi$ are defined through

$$m = \frac{16}{\pi} + \mu \equiv \frac{16}{\pi} + \mu'\epsilon \tag{2.32}$$

$$\xi \equiv \xi'|\epsilon| \tag{2.33}$$

where $\epsilon \ll 1$ and $\xi'$ and $\mu'$ are order 1 quantities and

$$f = f(\xi, \mu), \tag{2.34}$$

then a series expansion of $\det(\mathbf{M})$ in the neighbourhood of $\epsilon = 0$ can be performed, to obtain term by term a series expansion for $f$. It is found that there are two solutions, $f_+$ and $f_-$, which correspond to functions $y(x)$ symmetric and anti-

symmetric about $x = \pi/2$ respectively:

$$\begin{aligned} f_+ = \Bigg[4 + \frac{\pi}{6}\mu - \frac{\pi^2}{576}\mu^2 + \frac{\pi^3(6-\pi^2)}{124416}\mu^3 \\ + \frac{\pi^4(2\pi^2-21)}{11943936}\mu^4 \\ + \frac{\pi^5\left(315 - 15\pi^2 - \pi^4\right)}{4299816960}\mu^5 + O(\mu^6)\Bigg] \\ + |\xi|\left[0 + O(\mu^5)\right] \\ + \xi^2\left[\frac{2\pi}{9}\mu + \frac{\pi^2}{72}\mu^2 - \frac{\pi^3\left(3+\pi^2\right)}{93312}\mu^3 + O(\mu^4)\right] \\ + |\xi^3|\left[-\frac{128}{9\pi} - \frac{40}{27}\mu - \frac{\pi\left(15-\pi^2\right)}{486}\mu^2 + O(\mu^3)\right] \\ + \xi^4\left[0 + O(\mu^2)\right] + |\xi^5|\left[-\frac{1024}{135\pi} + O(\mu)\right] \end{aligned} \tag{2.35}$$

$$\begin{aligned} f_- = 4 + |\xi|\left[0 + O(\mu^5)\right] + \xi^2\left[\frac{32}{\pi^2} + \frac{2}{\pi}\mu + O(\mu^4)\right] \\ + |\xi^3|\left[0 + O(\mu^3)\right] \\ + \xi^4\left[-\frac{(128\pi^2+576)}{3\pi^4} - \frac{(8\pi^2+72)}{3\pi^3}\mu + O(\mu^2)\right] \\ + |\xi^5|\left[\frac{512}{3\pi^3} + O(\mu)\right]. \end{aligned} \tag{2.36}$$

The final value for $f_{\min}$ in this neighbourhood is then $f_{\min} = \min(f_+, f_-)$.

The results are plotted in Fig. 2.7, and it is observed that the behaviour of $f_{\min}$ around the bifurcation point is not analytic, since the transition between the two branches $f_+$ and $f_-$ leads to a discontinuity in the derivatives of $f_{\min}$. The maximal value of $f_{\min}$ (i.e the optimum that is desired), occurs for $\xi = 0$ when $\mu < 0$, and along the locus $f_+ = f_-$ when $\mu > 0$. From Eqs. (2.35) and (2.36), this leads to the optimal value of $\xi$ being

$$\xi_{\text{opt}} = \begin{cases} \frac{\pi^{3/2}}{8\sqrt{3}}\mu^{1/2} - \frac{\pi^4}{864}\mu + O\left(\mu^{3/2}\right) & \text{if } \mu \geq 0 \\ 0 & \text{if } \mu < 0 \end{cases} \tag{2.37}$$

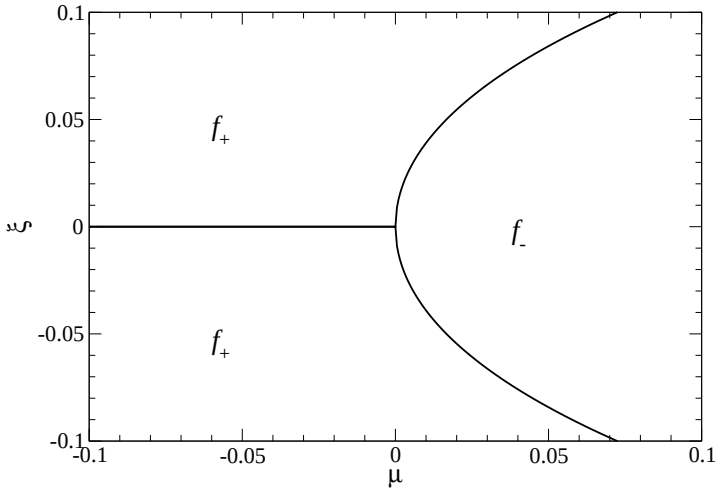


Figure 2.8: Curve shows the locus of optimal values for $\xi$ near the first bifurcation point. This divides the $\xi - \mu$ plane into three regions, in which $f_{\min}$ is given by either Eq. (2.35) or (2.36) as indicated.

This is shown in Fig. 2.8, together with the regions of the $\mu - \xi$ plane in which $f_+$ and $f_-$ apply. Good agreement is found between Eq. (2.37) and the computational work of the previous section, this is shown in Fig. 2.9

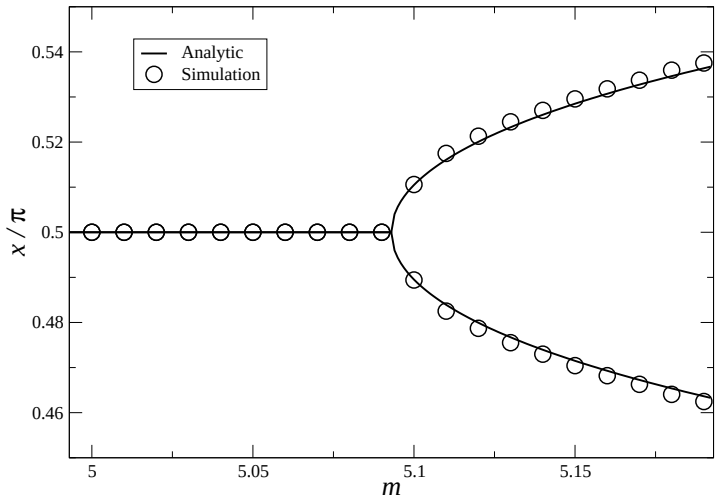


Figure 2.9: Analytic and computational findings for the optimal position of elastic support around the first bifurcation point at $m = \frac{16}{\pi}$.

## 2.7 Discussion

The optimal elastic support for the column appears to display complex behaviour: at small values of $m$ the support is a single delta function, and even at large values of $m$, it appears to be advantageous for $\rho(x)$ to be concentrated into discrete delta-functions rather than to be a smooth distribution.

Furthermore, the manner in which the system moves from a single to multiple delta functions is not trivial, and appears to be through bifurcation events. In the full optimisation problem it is found that the first bifurcation event occurs with critical exponent of one-half. Inverting Eq. (2.37) and substituting it into either Eq. (2.35) or (2.36) it is found that,

$$f_{\min} \approx \begin{cases} 4 + \frac{32}{\pi^2}\xi_{\text{opt}}^2 - \frac{64\left(2\pi^2-9\right)}{3\pi^4}\xi_{\text{opt}}^4 & \text{if } \mu \geq 0 \\ 4 + \frac{\pi}{6}\mu - \frac{\pi^2}{576}\mu^2 & \text{if } \mu < 0. \end{cases} \tag{2.38}$$

while to leading order,

$$\xi_{\text{opt}} = \begin{cases} \frac{\pi^{3/2}}{8\sqrt{3}}\mu^{1/2} & \text{if } \mu \geq 0 \\ 0 & \text{if } \mu < 0. \end{cases} \tag{2.39}$$

In this form, the mathematical similarities to Landau theory of second order phase transitions become apparent, with $\xi_{\text{opt}}$ playing the role of the order parameter, $\mu$ the reduced temperature and $-f_{\min}$ the free energy to be minimised.

However, there is an important difference. In Landau theory of second order phase transitions, the free energy $F_{\text{lan}}$ is assumed to be a power series expansion in the order parameter $\psi$ with leading odd terms missing:

$$F_{\text{lan}} = F_0 + a_2\psi^2 + a_4\psi^4 + ... \tag{2.40}$$

where $a_2 \propto (T - T_c)$, the reduced temperature. In our case, the buckling force $f$ has to be first optimised for even and odd buckling. Thus $-f_{\min}$ (which is the analogue of $F_{\text{lan}}$) is a minimum over two intersecting surfaces (Fig. 2.7) and so non-analytic at the point of bifurcation.

Nevertheless, the mathematical form of the solution in Eq. (2.39) is identical, including the critical exponent. Furthermore, our numerical results show that, for the equal support case, the critical exponent $\alpha$ is preserved for the next bifurcation.

The details of the behaviour for larger values of $m$ is as yet unclear: it is hypothesised that there will be a cascade of bifurcations, as seen in the limit set of certain iterated maps [36]; it remains an open question whether there is an accumulation point leading to potential chaotic behaviour.

Further investigation of this regime may shed light on structural characteristics required to protect more complex engineering structures against buckling instabilities.

# Chapter 3

# Fractal designs for efficient pressure bearing structures

## 3.1 Introduction

Ammonites are an extinct group of marine invertebrate animals, which derive their name from the spiral shape of their fossilised shells. The internal part of these shells are divided into chambers by the septa. Where the septa meet the shell wall they form suture lines. The evolution of complex suture line patterns in cephalopod ammonoids is one of the best documented trends towards higher degrees of structural complexity in the fossil record [37]. Hierarchical design and statistical self-similarity has long been appreciated within these architectures, and increasingly accurate measurements of fractal dimensions have been undertaken [38, 39, 40]. The functionality of these complex architectures is however a matter of debate. Numerous explanations link these complex geometries to metabolic function [41], buoyancy control [42] and increased mantle surface area [43]. Intriguingly, structural stability has also been proposed as a design driver [44]. Links between structural requirements and mineral deficiencies have led

to questions regarding structural efficiency being a design goal. Most recently, elastic fractal composite models have been created to directly investigate the role of structural hierarchy on stiffness, strength and failure modes finding that the order of hierarchy can be used to tailor mechanical properties non-linearly over a wide range of values for a given volume [45].

Here a fractal design is proposed, not directly related to the ammonites, for pressure bearing structures. Using a sphere and a cylinder as examples, it is demonstrated that the fractal design principle applies to multiple structures with both zero and non-zero Gaussian curvature. Bounds are obtained for the relationship between the volume of material required to create a stable structure and the applied external pressure. Finally, a non-trivial dependence on hierarchical order is shown and the fractal dimensions of such structures are found.

As a reference, a simple hollow cylinder of radius, $r$, and thickness, $t$, made from a material with Young's modulus $Y$, and Poisson ratio $\nu$, subject to an external pressure loading $P$ is first considered. In the limit $t \ll r$, mechanical stability requires that the inequality $P < 3Yt^3/12(1-\nu^2)r^3$ is satisfied [21]. Then, defining a non-dimensional volume as the volume of material used to make the structure scaled by the volume enclosed by the cylinder, $v \equiv V_{\text{req}}/V_{\text{enc}}$, and non-dimensional pressure $p \equiv P/Y$, it is found that the minimum volume necessary to create a stable cylinder is related to the pressure it must withstand by,

$$v_c\,(1) = \beta_c\, p^{\frac{1}{3}}, \tag{3.1}$$

where $\beta_c$ is a constant dependent on material properties. The notation $v_c(1)$ is used for coherence with later sections. In an analogous calculation, the stability of a sphere requires $P < 2Yt^2/\sqrt{3\,(1-\nu^2)}r^2$. In the same limit $t \ll r$, after normalising the volume required against that enclosed by the sphere, it is found

that the minimum volume required for stability is given by,

$$v_s\,(1) = \beta_s\, p^{\frac{1}{2}}, \tag{3.2}$$

where $\beta_s$ is a constant. These structures will be termed generation-1 in subsequent sections, and will serve as a reference. Most practical applications are found in the regime of $P \ll Y$ (i.e. $p \ll 1$), therefore larger powers of $p$ imply greater structural efficiency. In this sense, spheres are more efficient than cylinders ($\frac{1}{2}$ vs $\frac{1}{3}$).

## 3.2 Theory

The fractal structure that is proposed is generated through an iterative procedure in which solid shells get replaced by composite sheets; the generation, $G$, of the structure is given by the number of these iterations performed (plus one). The composite sheet is made up of three substructures, each identical up to a rotation of $\pm 2\pi/3$. Each of the substructures can be considered as an infinite set of

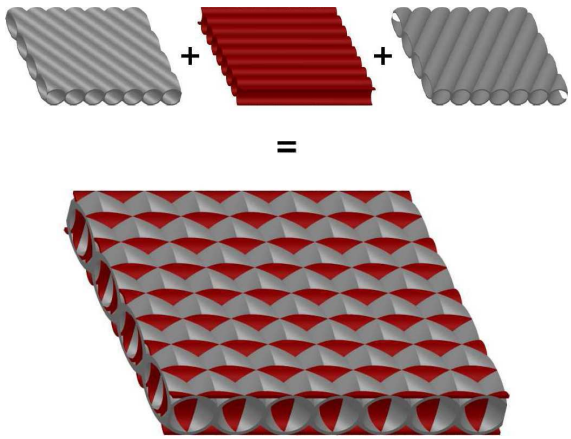


Figure 3.1: Composite sheet used as a basis for our fractal design shown below the three component substructures. One of the three substructures is shown in red. The exposed surface consists of three sets of curved diamond faces.

parallel circular cylinders with their axes in the $x$-$y$ plane, placed so that each touches two neighbours [24]. The resultant structure is shown in Fig. 3.1. It is assumed that when deformations in the structure occur, provided that the wavelength of the deformation is long in comparison with the thickness of the composite material, the plate behaves as a single entity. Through considerations of stretching and bending energies of the composite sheet and comparison with the general equations for a plate undergoing deformations [46], it can be shown [24] that the plate is at least as stiff as a solid plate with effective material properties and thickness:

$$Y_{\text{eff}} = (\pi/\sqrt{6})(t/r)Y, \tag{3.3}$$

$$\nu_{\text{eff}} = 1/3, \tag{3.4}$$

$$t_{\text{eff}} = \sqrt{6}r, \tag{3.5}$$

where $Y_{\text{eff}}$, $\nu_{\text{eff}}$ and $t_{\text{eff}}$ are the effective Young's modulus, Poisson ratio and thickness of the composite plate and $t$ and $r$ are the thickness and radius of the constituent cylindrical substructures. These relationships are derived as lower bounds for the material properties, they are obtained through the approximation that the constituent cylinders are able to move freely though one another while being required to follow the same deformation field. This approximation has previously been termed the 'ghost approximation' and is known to underestimate the stiffness of the structure and thus overestimate the volume of material required for stability [24]. It is noted that under pressure loading the actual structure will experience shear stresses in the surface membrane, particularly near the intersections of the curved surfaces. However, given that in plate girders [21], such stresses do not have a significant effect on the ultimate strength of the structures, and considering the nature of the interaction equation between shear and

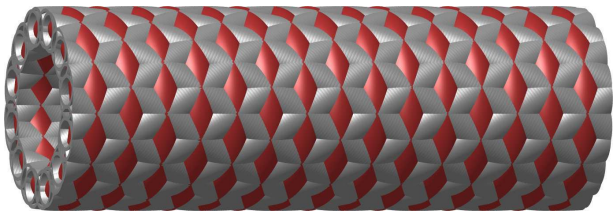

(a)

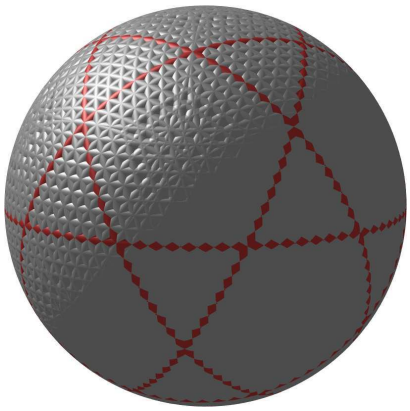

(b)

Figure 3.2: (a) Generation-2 cylindrical design for pressure bearing structure. The red tori have been oriented to carry the hoop stresses. (b) Generation-2 spherical design. The red tori are the edges of the spherical icosidodecahedron.

compression in a plate [47, 48], these shear stresses are neglected in what follows.

Replacing the solid material of a generation-1 cylinder with a curved composite sheet defines the generation-2 cylinder shown in Fig. 3.2(a). The large radius and effective shell thickness of this structure are denoted $r_{2,2}$ and $t_{2,2}$, while the effective material properties on this largest scale are written as $Y_{2,2}$ and $\nu_{2,2}$ for Young's modulus and Poisson ratio respectively. The properties of the cylindrical substructures are denoted $r_{2,1}$, $t_{2,1}$, $Y_{2,1}$ and $\nu_{2,1}$, where the symbols retain their original meanings. The material is wrapped around the cylinder such that one of the substructures is perpendicular to the long axis of the pressure bearing cylinder [see Fig. 3.2(a)].

The construction of the generation-2 sphere is more complex, as the Gaussian curvature poses a problem in creating a sphere that locally resembles the composite sheet shown in Fig. 3.1. An alternative construction is therefore proposed for the fractal design. A spherical icosidodecahedron made up of hollow tori is taken, and on either side of these great circles, bands of parallel tori are created, each band wide enough to meet, but not cross the nearest vertex. The design does not retain the simple periodicity over the whole structure, instead where the number of intersecting substructures is minimal the sphere locally resembles the composite sheet. The design is such that the weakest part of the structure has the material properties bounded by Eqs. (3.3 - 3.5); elsewhere it is stronger. The design is shown in Fig. 3.2(b). The notation for the dimensions of the structure and substructures follows that of the cylinder.

The same procedure is applied iteratively to construct higher generation numbers, $G$, by replacing the curved shells of the smallest substructure with curved composite sheets. For $G \geq 2$ these smallest substructures are made of cylinders (even when the large shape is a sphere), and it is chosen that the orientation of the composite sheets to have one set of cylinders parallel to the axis of the

cylinders in these substructures. For a generation-$G$ structure, the geometric and material properties are defined by $r_{G,m}$, $t_{G,m}$, $Y_{G,m}$ and $\nu_{G,m}$ where the first index $G$ denotes the generation of the structure and the second index, $m \in \{1, \ldots, G\}$, refers to the specific level in the structure, with $m = 1$ representing the smallest substructures. These parameters take the values (G$\geq$ 2),

$$Y_{G,m} = (\pi^{m-1}/\sqrt{6})(t_{G,1}/r_{G,m-1})Y, \tag{3.6}$$

$$\nu_{G,m} = 1/3, \tag{3.7}$$

$$t_{G,m} = \sqrt{6} r_{G,m-1}. \tag{3.8}$$

These results are used to calculate an upper bound for the material required to make a stable structure under a given external pressure. A straightforward calculation shows that the volume required to make a generation-$G$ structure of (largest) radius $r_{G,G}$, divided by the volume enclosed by the cylinder is given by,

$$v_c\,(G) = 2\,(3\pi)^{G-1}\, t_{G,1}/r_{G,G}, \tag{3.9}$$

while the volume of material used to create the sphere is not greater than

$$v_s(G) = (\pi/5)\,(3\pi)^{G}\, t_{G,1}/r_{G,G}. \tag{3.10}$$

For convenience the parameters

$$\hat{v}_c\,(G) \equiv \log_{10}[v_c\,(G)\,(3\pi)^{1-G}\,/2], \tag{3.11}$$

$$\hat{v}_s\,(G) \equiv \log_{10}[5v_s\,(G)\,(3\pi)^{-G}\,/\pi], \tag{3.12}$$

$$\hat{p} \equiv \log_{10} p, \tag{3.13}$$

$$\hat{r}_m \equiv \log_{10}\,(r_{G,m}/t_{G,1})\,, \tag{3.14}$$

are defined so that all of the buckling constraints below become linear inequalities. Using this notation Eqs. (3.1 - 3.2) become,

$$\hat{v}_c(1) = (\hat{p}/3) + \hat{\beta}_c, \tag{3.15}$$

$$\hat{v}_s(1) = (\hat{p}/2) + \hat{\beta}_s, \tag{3.16}$$

where greater efficiency in the limit $p \to 0$ is now represented by larger coefficients of $\hat{p}$.

At all levels $m < G$ there are two possible modes of failure: the exposed curved surfaces may be crushed by the applied pressure, and the cylindrical substructures at this level may buckle locally (Koiter buckling [49]) under the axial load they carry. The crush pressure failure mode causes long wavelength deformations in the structure, it is thus assumed that when the composite structure fails due to crush pressure the plate behaves as a single entity [24]. By contrast, the Koiter buckling is characterised by short wavelength deformation on failure. Here, to obtain an upper bound on the material required to construct a stable structure, it is assumed that the individual components of the composite plate fail due to Koiter buckling at the same value of loading as they would if they were isolated from the rest of the structure. At level $G$, there is only one failure mode, that is where the direct pressure makes the whole structure unstable to small perturbations from its original configuration. A cylindrical shell, subtending an angle $2\alpha$ at its axis is stable, provided [21]

$$P < \frac{Y_{\text{eff}} t_{\text{eff}}^3}{12\left(1-\nu_{\text{eff}}^2\right) r^3}\left(\frac{\pi^2}{\alpha^2} - 1\right). \tag{3.17}$$

For the composite cylinder on the largest length scale $\alpha_{G,G} = \pi/2$ (which encapsulates the required symmetry about the two inflection points). Thus, using

Eqs. (3.6 - 3.8) it is seen that $p$ must be bounded by:

$$p < \frac{27\pi^{G-1}}{16} \frac{t_{G,1} r_{G,G-1}^2}{r_{G,G}^3}. \tag{3.18}$$

Then using the notation of Eqs. (3.13-3.14), Eq. (3.18) yields the first restriction our cylindrical structure must satisfy:

$$\hat{p} < -3\hat{r}_G + 2\hat{r}_{G-1} + a_G, \tag{3.19}$$

where $a_G$ is a constant. The spherical design has an analogous failure mode at this level; the stability of the whole sphere requires:

$$P < \frac{2Y_{\text{eff}} t_{\text{eff}}^2}{\sqrt{3(1-\nu_{\text{eff}}^2)} r^2}. \tag{3.20}$$

Through use of Eqs. (3.6 - 3.8), for our composite structure on the largest length-scales the restriction,

$$p < 3\pi^{G-1} \frac{t_{G,1} r_{G,G-1}}{r_{G,G}^2}, \tag{3.21}$$

is found to apply, which, when transformed into an alternative form through Eqs. (3.13-3.14), it is obtained,

$$\hat{p} < -2\hat{r}_G + \hat{r}_{G-1} + c_G, \tag{3.22}$$

where the $c_G$ is a constant. Each level of the hierarchical structure for $G > 1$ has a series of exposed diamond surfaces that the pressure acts upon. Each diamond shaped surface subtends a maximum angle of $2\alpha$, as they are subsets of the section of cylinder subtending the constant angle $2\alpha$ in Fig. 3.3. It can be assumed that

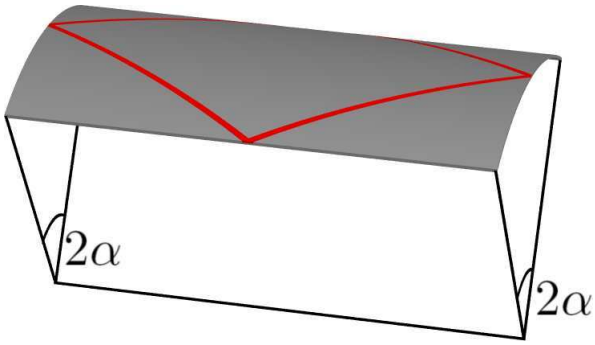


Figure 3.3: Diamond-shaped portion of the cylindrical substructures which is exposed to the external pressure. This diamond [outlined in red] subtends an angle $2\alpha$ at the cylinder axis, which is independent of the hierarchical level in the structure.

if this larger surface is stable under the pressure loading, the smaller exposed diamond shaped shell is also stable. In the limit of $r_m \gg r_{m-1}$ in either the case of the sphere or the cylinder, this angle approximates to

$$\alpha_{G,m} = \tan^{-1}(2/\sqrt{5}) \quad \text{for} \quad 1 \leq m \leq G-1. \tag{3.23}$$

The limit $r_m \gg r_{m-1}$ is equivalent to the case of gentle pressure. In this regime, both the cylinder and the sphere have to satisfy the same inequalities. Taking Eqs. (3.17 & 3.6 - 3.8), it is straightforward to find that for stability of length-scales $2 \leq m \leq G-1$ the inequalities

$$p < \frac{9\pi^{m-1}}{16} \frac{t_{G,1} r_{G,m-1}^2}{r_{G,m}^3} \left( \frac{\pi^2}{\alpha_{G,m}^2} - 1 \right) \tag{3.24}$$

hold; while considering the stability of the smallest features against crush failure, it is seen that,

$$p < \frac{1}{12(1-\nu^2)} \frac{t_{G,1}^3}{r_{G,1}^3} \left( \frac{\pi^2}{\alpha_{G,1}^2} - 1 \right). \tag{3.25}$$

Then, creating a set of linear inequalities incorporating stability requirements

under crush pressure using Eqs. (3.13 - 3.17, & 3.23) it is found that,

$$\hat{p} \;<\; -3\hat{r}_m + 2\hat{r}_{m-1} + a_m \quad \text{for} \quad 2 \leq m \leq G-1, \tag{3.26}$$

$$\hat{p} \;<\; -\hat{r}_1 + a_1, \tag{3.27}$$

where the $a_m$ are constants and are independent of shape.

The next mode of failure that must be protected against is caused by hoop stresses: in loading our cylinder or sphere (on the largest scale) symmetrically, a compressive force running circumferentially is generated proportional to the pressure loading and inversely proportional to the radius of the structure, $r_{G,G}$. This force, when acting on the hollow substructures, can lead to local buckling [49]. In the case of the cylinder, this stress is parallel to one of the substructures in our composite sheet and, in order to obtain an analytic upper bound for volume required for stability, is assumed to load only this substructure axially. In the case of the sphere the largest substructures form continuous cylindrical hoops or tori running around the sphere. It is assumed that they are all loaded uniformly with the maximum possible stress and that they fail under the same conditions as an isolated cylinder. For generation-3 and above, the failure that can be caused through the axial loading of this cylinder being transmitted through to all the lower hierarchical levels must be included. These lower level structures were chosen to have a substructure running parallel with this axial loading and again, this substructure alone is assumed to take the load: contributions to stability from the other substructures being neglected. These conservative approximations on stability are expected to provide a robust upper bound on the required amount of material. It can be shown that for all levels $1 \leq m \leq G-1$, the maximal

loading on any component cylinder in the case of the cylinder is,

$$F_{G,m} = 2Pr_{G,G}\pi^{m+1-G}r_{G,m} \tag{3.28}$$

while the maximal compressive load in the case of the sphere is one quarter of this loading. The maximal axial force that can be withstood by the composite cylinders before local buckling is caused [25] is,

$$F_{G,1} < \frac{2\pi Y_{G,1}t_{G,1}^2}{\sqrt{3(1-\nu^2)}}, \tag{3.29}$$

$$F_{G,m} < 3\pi^m Y t_{G,1} r_{G,m-1}. \tag{3.30}$$

Then, combining these expressions and using Eqs. (3.13 - 3.14), for stability against these failure modes it is found:

$$\hat{p} < -\hat{r}_m - \hat{r}_G + \hat{r}_{m-1} + b_m \quad \text{for} \quad 2 \leq m \leq G-1, \tag{3.31}$$

$$\hat{p} < -\hat{r}_1 - \hat{r}_G + b_1, \tag{3.32}$$

where the $b_m$ are constants. These inequalities are valid for both the case of the sphere and the cylinder. However the values of the constants $b_m$ are shape dependent; those for the sphere being a factor of four greater than those for the cylinder.

## 3.3 Results

The stability of a fractal object under external pressure loading with multiple failure modes has been encapsulated into a simple set of linear inequalities. These can then be solved numerically (by linear programming methods) for a given pressure to find the minimum required volume of construction material for stability.

However, the same results can be found analytically: the assumption is made that on larger length scales [specifically, $m > k(G)$, where $k(G)$ is an integer value, depending only on generation number and the shape] the structure is vulnerable to crush pressure buckling, while at smaller length scales [$m \leq k(G)$], the structure becomes unstable due to Koiter buckling. Thus, there is only one crossover point between the two failure modes, which occurs between levels $k$ and $k+1$. To obtain values of $\hat{r}_m$ a naïve optimisation strategy is used: using Eqs. (3.31 - 3.32), it is found that

$$\hat{r}_m = -m(\hat{p} + \hat{r}_G) + \sum_{i=1}^{m} b_i \quad \forall \quad 1 \leq m \leq k \tag{3.33}$$

where the $b$'s are shape dependent. Now the remainder of the constraints for crush pressure of the substructures are used as equalities, i.e. Eqs. (3.26 - 3.27), to obtain,

$$\begin{aligned} \hat{r}_m &= \left(\frac{2}{3}\right)^{m-k} \hat{r}_k + \hat{p}\left[\left(\frac{2}{3}\right)^{m-k} - 1\right] \\ &+ \frac{1}{3}\sum_{i=1}^{m-k}\left[\left(\frac{2}{3}\right)^{m-k-i} a_{k+i}\right] \; \forall\, k < m < G. \end{aligned} \tag{3.34}$$

Then, using Eq. (3.33 - 3.34) and Eq. (3.19) or Eq. (3.22) for the cylinder and sphere respectively, expressions for $\hat{r}_G$ are obtained, these [Eqs. (3.9, 3.10)] differ from $-\hat{v}$ by only a constant. In the analysis it has been assumed that every level of the structure to be on the limit of collapse, the scaling relationship obtained above can then only be stable against all modes of failure if the volume used is maximised on every level. This equates to choosing $k$ such that the coefficient of $\hat{p}$ in our expressions for $\hat{v}_s$ and $\hat{v}_c$ is maximised. It is found that the coefficient of $\hat{p}$ in the case of the cylinder has only one extremum for $k \in [1, G-1]$ and this

corresponds to a minimum at

$$k = G - 2.23, \tag{3.35}$$

however, $k$ is limited to integer values and through substitution it is seen that the minimum is $k = G - 2$. This leads to a minimum for $\hat{v}$ as,

$$\hat{v}_c\left(G\right) = \frac{4G-3}{4G+1}\hat{p} + \hat{\kappa}_c\left(G\right) \quad \text{for} \quad G \geq 2, \tag{3.36}$$

where $\hat{\kappa}_c\left(G\right)$ is independent of pressure and is given by:

$$\hat{\kappa}_c(G) = \frac{1}{4G+1}\log_{10}\left[\frac{768\pi^{-4G^2+7G-1}\left(1-\nu^2\right)^2}{\left(\frac{\pi^2}{\alpha_{G,1}^2}-1\right)^2}\left(\frac{16}{81}\right)^G\right] \tag{3.37}$$

In the case of the sphere, the same procedure is followed and the value of $k$ in this case is found to be $G - 1$. Thus all diamond surfaces retain stability to a value of $\hat{p}$ greater than that taken to induce local buckling through hoop stress. The minimum non-dimensional volume is therefore found to be:

$$\hat{v}_s\left(G\right) = \frac{G}{G+1}\hat{p} + \hat{\kappa}_s\left(G\right) \quad \forall \quad G \geq 2 \tag{3.38}$$

where,

$$\hat{\kappa}_s(G) = -\frac{1}{G+1}\log_{10}\left[\frac{6^G\pi^{G^2+G-1}\sqrt{\frac{3}{4}}}{\sqrt{1-\nu^2}}\right]. \tag{3.39}$$

For a given $\hat{p}$ there will be an optimal value of $G$, and for $\hat{p} \to 0$ this optimal $G$ will be large. For most practical applications the optimal value of $G$ will not exceed four. Nevertheless the changed scaling law represents a considerable gain in efficiency over the generation-1 structure. In Fig. 3.4 the values of $\log_{10}\left(v\right)$ for

both the sphere and the cylinder [(a) and (b) respectively] are plotted against $\log_{10}(p)$ for the values of $\hat{p}$ where $r_{G,m+1} \gg r_{G,m}$.

Below the crossover from crush pressures [$m > k(G)$] to Koiter buckling [$m \leq k(G)$], for sufficiently high generation of structures, the fractal dimension can

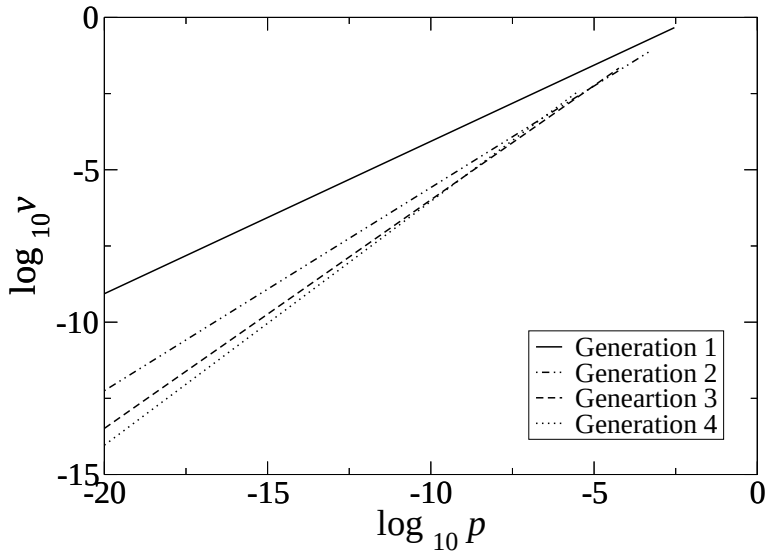


(a)

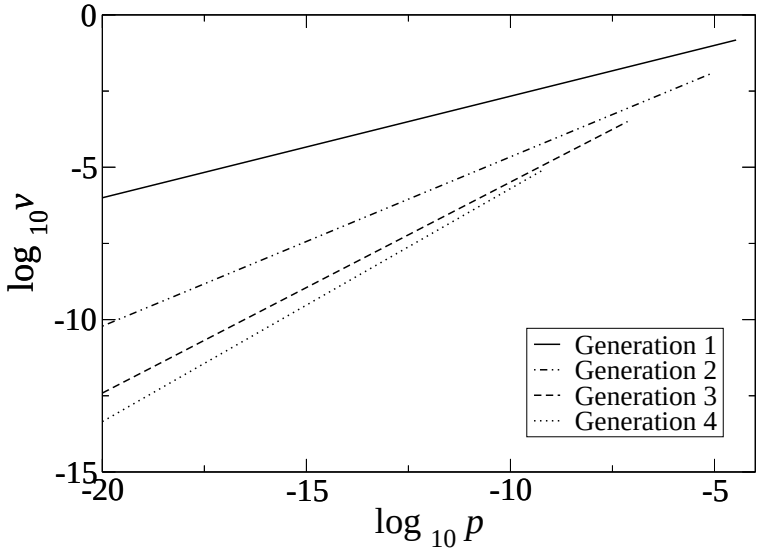


(b)

Figure 3.4: Plot of $\log_{10} v$ versus $\log_{10} p$ for the optimal structures for the sphere (a) and the cylinder (b) in generations 1 to 4. Material properties are taken to be close to steel, $\nu = 0.29$ and $E = 210GPa$. Plots are limited to the range $\hat{r}_m - \hat{r}_{m-1} > \log_{10} 20$, $m \in [G, 2]$ and $\hat{r}_1 > \log_{10} 20$ in accordance with our approximations

be defined. It is found that the fractal dimension is not length dependent (in other words, the structure has a single Hausdorff dimension); Fig. 3.5 shows the Hausdorff dimension for the optimal structure for a given value of loading for both the sphere and the cylinder.

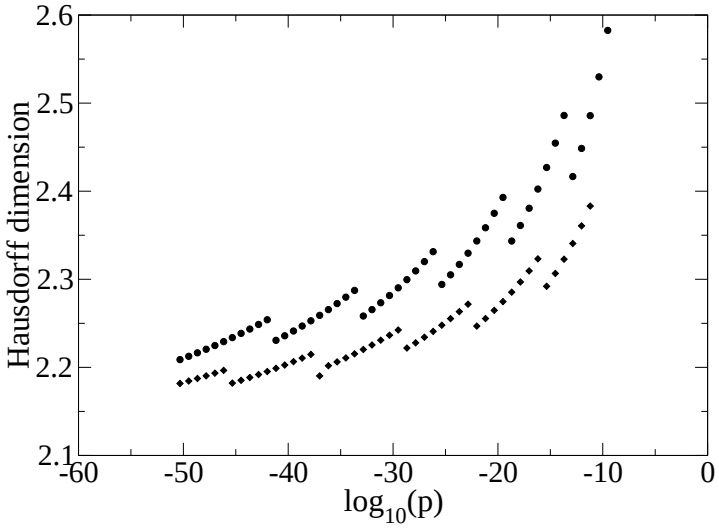


Figure 3.5: The fractal dimension below the crossover from crush pressure failure mode to Koiter buckling for the cylinder (diamonds) and the sphere (circles) of the optimised structures for a given pressure. Discontinuities represent a change in the number of hierarchical levels in the optimal design.

## 3.4 Conclusion

It has been shown that fractal design can produce a structure that is highly efficient under gentle pressure loadings. The design was illustrated with example structures of a cylinder and a sphere, but the approach is generally applicable to other shapes. The results obtained in terms of scaling relations appear to be universal and robust. In general, fractal design increases structural complexity which requires sophisticated manufacturing techniques, such as rapid prototyping [50]. In addition, the optimal generation number decreases with increasing pressures, thus in all terrestrial applications, the optimal generation does not exceed 4. This

puts some constraint on, but does not negate, the engineering challenges, which will consist in balancing improved efficiency against both increased manufacturing costs, and potential fragility of the structures under material and geometrical imperfections [51]. The trade-off between robustness and efficiency in particular merits further investigation.

# Chapter 4

# Hierarchical structure for robust adhesion of two surfaces

## 4.1 Introduction

In this chapter, the effect of geometry on adhesion between two surfaces for a given interaction strength is investigated. A particular focus is on the use of hierarchical geometry for creating a robust, irreversible adhesion between surfaces. Hierarchical structures for increasing the adhesion between two surfaces have been well documented in nature; for example, geckos and many insects have evolved special tissue on the bottom of their feet to support their weight on vertical walls and ceilings [52]. While other contributions have been proposed [52, 53], it is understood that the primary interaction responsible for this adhesion is the van der Waals interactions between the animal's foot and the contact surface [54, 55, 56, 57]. It has been found that the structure responsible for making this adhesion possible, through use of the very weak van der Waals interaction, is fractal-like with features from nanoscale up [52]. Interestingly this structure must not only create reliable adhesion between the foot and the unpredictably rough

surface, but it must also be releasable to allow for locomotion. This structure has been emulated in order to produce a man-made, self cleaning, re-attachable adhesive tape [58]. More recently the same structure has been constructed using multi-wall carbon nano-tubes with greater adhesive potential [59].

The design proposed here is dependent on being able to modify both sides of the interface and, unlike the gecko's foot structure, is non-releasable. The geometry of the interacting surfaces relates to another natural example. Within the equine hoof the distil phalanx (pedal bone) is suspended from the hoof wall by way of hierarchical structure [32, 33]. The adhesive interaction between the two materials is dependent on the basement membrane, where the basal cells of the epidermis join to the soft connective tissue emanating from the pedal bone [32]. This interface is responsible for creating a robust, non-detachable, load-bearing connection between two materials of vastly different stiffness. A particular motivation for this work is equine laminitis, a condition whereby the hoof wall separates from the pedal bone resulting in lameness. While much work has been done on the biological causes of laminitis [32], the effect of the geometry has not been understood. The naturally occurring hierarchical structure is shown in Fig. 4.1 where a 2-dimensional slice through the equine hoof is shown through micrograph techniques. The stiff hoof wall is directly attached to the bottom set of lamellae, the primary epidermal lamellae (labelled P.E.L. in the right hand side of Fig. 4.1), while the tips of the P.E.L. are orientated towards the pedal bone. Between the P.E.L. and the pedal bone is soft connective tissue. The geometry of the interface between the primary and secondary epidermal lamellae (P.E.L. and S.E.L.) and the primary and secondary dermal lamellae (P.D.L. and S.D.L.), shown in Fig. 4.1, is responsible for amplifying the effect of the interaction between the two surfaces to give a stable adhesive connection. Although the work presented in this thesis does not incorporate the intricacies of the biological

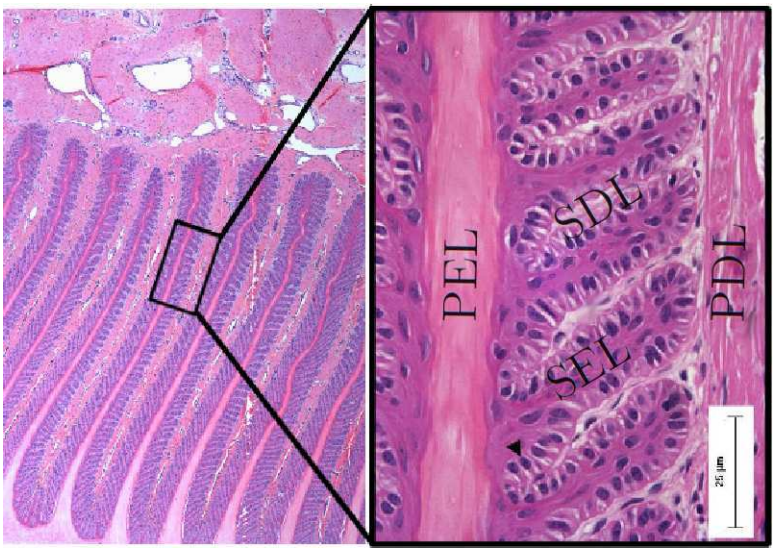


Figure 4.1: The interface between two materials responsible for amplifying the effect of an inter-surface interaction between the two materials. The structure with lamellae tips pointing up in the image on the left shows the set of lamellae termed primary and secondary epidermal lamellae (P.E.L. & S.E.L.) while the interlocking structure is termed primary and secondary dermal lamellae (P.D.L. & S.D.L.).

structure, the trends resulting from the investigation into this structural hierarchy are expected to apply to the naturally occurring structure.

## 4.2 Model

The model used here is simple in its formulation: both sides are modelled as a discrete set of nodes. These nodes, before deformation, create a uniform square lattice of unit spacing. Here the assumption is made that the two surfaces have vastly different Young's moduli; this allows for one side of the interface to be modelled as being infinitely stiff. Between the nodes, springs are placed with a spring constant that characterises either the deformable material's stiffness or the strength of the interaction between the surfaces, these springs have no resistance to rotation about the nodes; such a model is often referred to as a lattice spring model [60, 61]. A set of fixed nodes are specified which make up the

geometry of the infinitely stiff structure. The stiffness of the deformable material is characterised by the spring constant $K_s$ (regardless of spring length) and springs are placed between a node and its nearest and second nearest neighbours. The strength of interaction between the two surfaces is then characterised by the second set of springs, these are attached between nodes of the deformable and non-deformable surfaces, all with spring constant $K_i$, again, connecting nearest and second nearest neighbours. An applied load is then placed on the deformable surface. For an example lattice connecting two simple planar surfaces see Fig. 4.2.

## 4.3 Geometries

The geometry of the interface between the two materials being modelled here can be generated through an iterative procedure, as in the previous chapter, the term generation will refer to the number of iterations taken to generate the structure. A generation-0 structure can be thought of as being the interface of two planar surfaces.

The generation-1 structure can be thought of as a generation-0 structure with lamellae of a given length placed at regular intervals along its length, see Fig. 4.3.

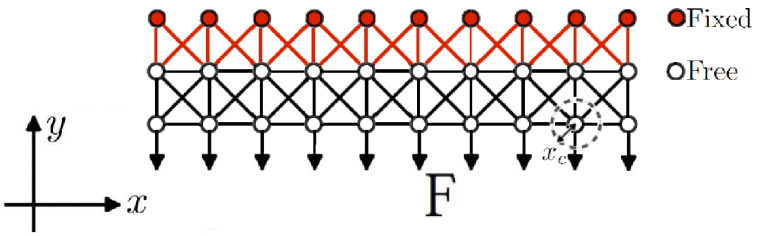


Figure 4.2: The generation-0 surface. Black lines indicate springs with spring constant of $K_s$ while red indicate those with spring constant $K_i$. Also in the diagram is the displacement at which separation is assumed to occur with the value $x_c$. The distance between the lamellae is fixed at 2 unit lengths.

Along the surface of the generation-1 lamellae, another set of lamellae can be placed at regular intervals creating the generation-2 structure (see Fig. 4.4); performing $n$ iterations of this same procedure results in a generation-$n$ structure. At each iteration, all lamellae introduced are assumed to be equal in length, however the lamellae at different hierarchical levels are not necessarily equal. The lengths of the lamellae at each hierarchical level of the structure will be denoted $L_{G,i}$; the first subscript in this notation denotes the generation of the structure while the second denotes the iteration that produced that set of lamellae. Also introduced is an angle, $\theta_{G,m}$, to define in which direction the lamella point with respect to the surface it protrudes from, for $i > 2$, $\theta < \frac{\pi}{2}$ denotes lamella facing away from the base of the $i-1$ level lamella while $\theta > \frac{\pi}{2}$ means the lamella are pointing back towards the base of the level $i-1$ lamella, this is shown in Fig. 4.4.

The effect of this geometry primarily increases the interaction surface area [32]. If the aspect ratio of the $i$-th level lamellae in a generation-$G$ structure are denoted $a_{G,i}$ it is easy to show that the surface area, $A$ increases proportionally

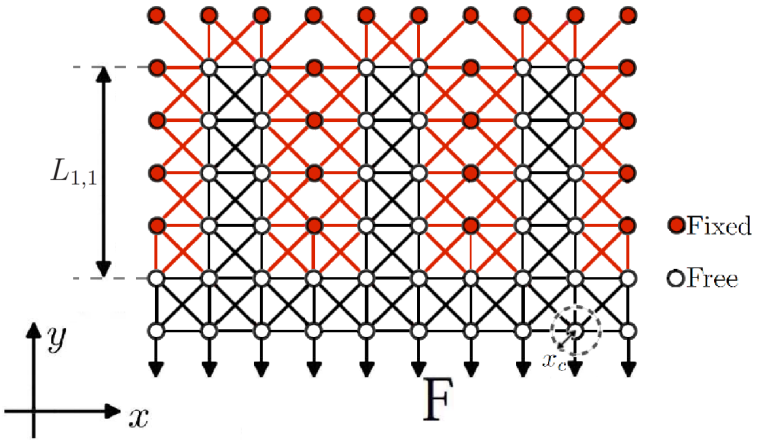


Figure 4.3: The generation-1 interface. A set of lamella protrude from the generation-0 interface in order to increase the surface area.

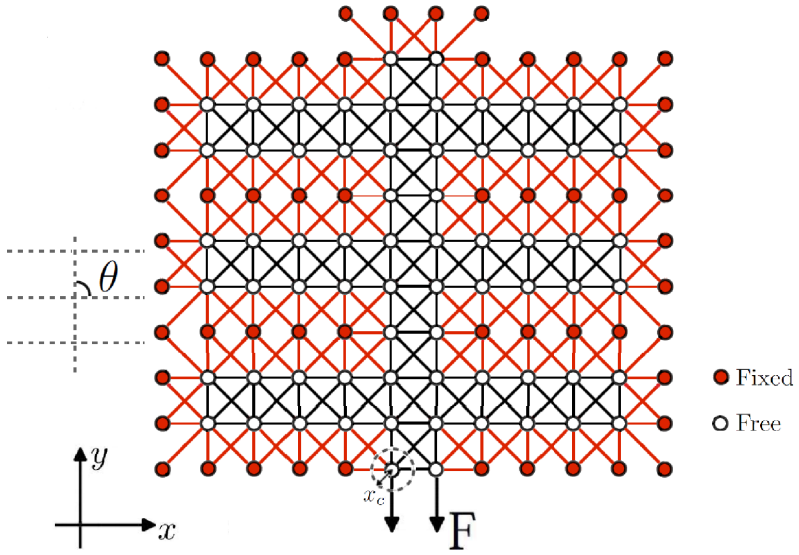


Figure 4.4: The generation-2 structure, a series of these structures joined in the $y$ direction could be used to create an interface between two surfaces. Shown is the definition of $\theta$ which describes how the second order lamella extend from the primary lamella, in the diagram $\theta = \frac{\pi}{2}$.

to the product of the aspect ratios:

$$A \sim \prod_{i=1}^{G} a_{G,i}. \tag{4.1}$$

It is straightforward to show that for two infinitely stiff surfaces with a given inter-surface interaction, the force required to separate the two surfaces depends on this scaling. However, for the adhesion of one rigid surface and one deformable surface the force required to separate the two is less straightforward to calculate.

## 4.4 Results

The results in this section are primarily obtained using computational methods. The method used in these simulations is the spherical arc-length method of finite element analysis, see appendix B or references [62, 63, 64].

### 4.4.1 Generation-0

As shown in Fig. 4.2, the generation-0 geometry is a simple planar interface. A set of nodes are linked by springs with spring constant $K_s$ representing the stiffness of the deformable surface and a second set of springs with spring constant $K_i$ link the deformable surface with the infinitely stiff surface. The ratio of the two spring constants introduced is defined as:

$$k \equiv \frac{K_i}{K_s}. \tag{4.2}$$

The failure load, $F_c$, of the structure is defined to be the force acting on the surface when any node making up the deformable surface has been displaced by an amount $x_c$, in this work $x_c$ is fixed to be half a unit length. A non-dimensional load,

$$f \equiv \frac{F}{K_s L_n}, \tag{4.3}$$

is defined, where $L_n$ is the distance between nodes and $f_c$ is the value of $f$ at the failure loading. Fig. 4.6 shows the dependence of critical force on the ratio $k$ for the generation-0 geometry; for $k \ll 1$ there is a linear dependence of $f_c$ on $k$. In this limit, all the deformation occurs in the inter-surface region and therefore this dependence is expected. In the region $k > 1$, a considerable proportion of the deformation before failure occurs in the deformable material, thus, the linear dependence is no longer present. In the limit $k \gg 1$, all the deformation occurs before the interface and, given the scaling of $f_c$, the non-dimensional load at failure tends to a constant value.

Through considering only displacements in the $y$-direction, an approximation for the energy required to move the upper, free, nodes in Fig. 4.2 by displacement

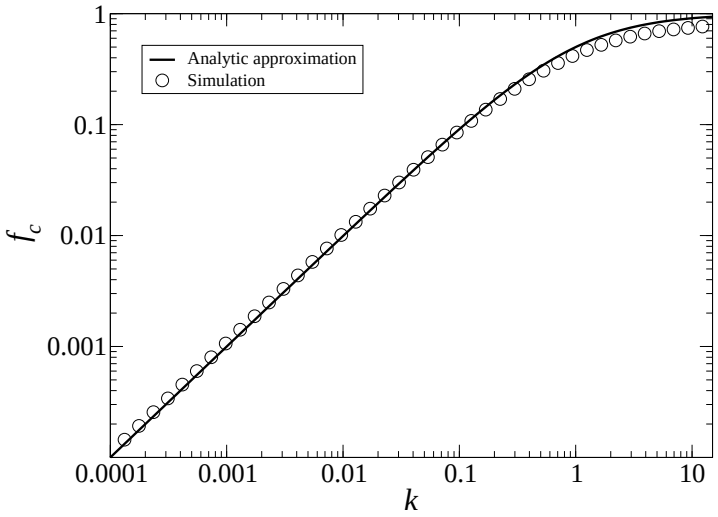


Figure 4.5: Results of simulation and analytic approximation for the generation-0 interface showing the dependence of $f_c$ on $k$.

$h_2$ and the lower set by an amount $h_1$ is found to be:

$$U = \frac{1}{2}(2N_1 + 1)K_i h_2^2 + \frac{1}{2}(2N_1 + 1)K_s(h_1 - h_2)^2 - Fh_1(N_1 + 1), \tag{4.4}$$

where $N_1$ is the number of nodes making up the surface in the $x$-direction. This approximation neglects the changes in geometry that occur during the loading procedure that are taken into account in the computational work. Requiring that,

$$\frac{\partial U}{\partial h_i} = 0 \qquad \text{for } i = 1, 2 \tag{4.5}$$

it can be shown that,

$$h_2 = \frac{h_1}{1 + k}, \tag{4.6}$$

$$(2N_1 + 1)K_s(h_1 - h_2) = F(N_1 + 1). \tag{4.7}$$

Thus, to cause a displacement of $x_c$ in any of the directly loaded nodes, the

non-dimensional load that must be applied is given by,

$$\frac{2N_1+1}{N_1+1}\frac{x_c}{L_s}(1-\frac{1}{1+k})=f_c \tag{4.8}$$

This confirms that for large $k$, $f_c$ tends to a constant dependent only on $K_i$, while for $k \to 0$, $f_c$ tends to zero. Good agreement is found between Eq. (4.8) and the finite element simulation (see Fig. 4.5).

### 4.4.2 Generation-1

In the transition from generation-0 to 1, assuming the width of the lamellae to be unity, the surface area of interaction is increased by a factor proportional to $L_{1,1}$. Therefore two important parameters must be investigated, $L_{1,1}$ and $k$. Plotted in Fig. 4.6 is the dependence of $f_c$ on $k$ for various values of $L_{1,1}$. It is seen that for a range of $k$ a half power-law is found relating $f_c$ and $k$:

$$f_c \sim k^{0.5}. \tag{4.9}$$

Thus for small values of $k$, $f_c$ will be greater for the generation-1 structure when compared to the generation-0 surface. The range of this one-half power-law can be extended by increasing the value of $L_{1,1}$. For finite values of $L_{1,1}$ in the limit $k \to 0$ the linear dependence of $f_c$ on $k$ is found to reappear. This occurs when the deformable surface is stiff enough such that it experiences little or no deformation in the loading procedure: all deformation occurs in springs with spring constant $K_i$ and thus, linear dependence of $f_c$ on $k$ is expected. In the region $k > 0.1$ the generation-0 interface requires a greater force to separate the surfaces than the generation-1 design. In the limit of large $k$ it is noted that the generation-1 design is considerably weaker than the equivalent generation-0 interface. In this

limit, the interface springs will resist extension more than the springs making up the surface, thus, the reduction in the number of interface interactions close to point of loading will reduce the force at failure.

It is possible to derive analytically the force that is required to create a given displacement at the bottom of a generation-1 lamella. This approach can be generalised to higher generation structures but for the purposes of this thesis only the generation-1 structure will be approached in this manner. Neglecting the contribution to energy from displacements in the $x$ direction and taking only

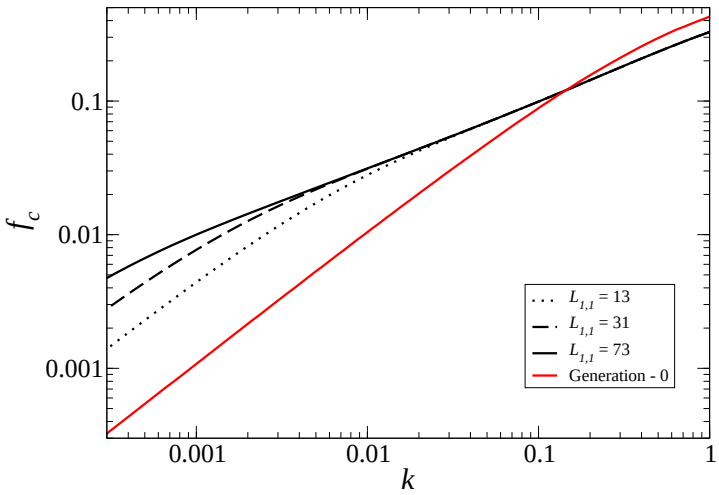


Figure 4.6: Showing the dependence of $f_c$ on $k$ for the generation-1 structure for various values of $L_{1,1}$, also shown for comparison is the generation-0 structure in red.

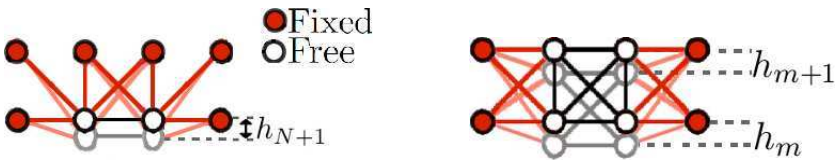


(a) (b)

Figure 4.7: The assumed shape of deformation for sections of the generation-1 lamella; left: the end points of the lamella; right: the mid-section of the lamella, $h_{m+1}$ and $h_m$ are not necessarily equal in magnitude.

highest order terms, the total energy can be written as:

$$U_{\text{tot}} = \sum_{m=1}^{N} \frac{1}{2} K_i (h_m^2 + h_{m+1}^2) + \sum_{m=1}^{N} \frac{3}{2} K_s (h_m - h_{m+1})^2 + 2K_i h_{N+1}^2 - F h_1. \quad (4.10)$$

where $h_m$ are illustrated in Fig. 4.7. Then, for the displacements $\{h_m\}$ to be those taken under loading, it is required that,

$$\frac{\partial U_{\text{tot}}}{\partial h_m} = 0 \; \forall \; m. \quad (4.11)$$

From the solution to the above equation, it can be shown that,

$$h_m = \begin{cases} \left(1 + \frac{5K_i}{3K_s}\right)^{-1} h_N & \text{for } m = N+1 \\ \left(2 + \frac{K_i}{3K_s}\right)^{-1} (h_{m+1} + h_{m-1}) & \text{for } 2 \leq m \leq N \\ \frac{2F}{K_i + 3K_s} + \frac{3K_s}{K_i + 3K_s} h_2 & \text{for } m = 1 \end{cases} \quad (4.12)$$

Then, using the notation [65],

$$\underset{i=1}{\overset{M}{\mathrm{K}}} = a_0 + \cfrac{b_1}{a_1 + \cfrac{b_2}{a_2 + \cfrac{b_3}{\ddots + \frac{b_M}{a_M}}}} \quad (4.13)$$

it can be shown that,

$$h_2 = h_1 \underset{i=1}{\overset{N-1}{\mathrm{K}}} \quad (4.14)$$

where,

$$a_n = \begin{cases} 2 + \frac{K_i}{3ks} & \text{if } n < N-1 \\ 2 + \frac{K_i}{3ks} - \frac{3K_s}{5K_i+3K_s} & \text{if } n = N-1 \end{cases} \qquad b_n = \begin{cases} 1 & \text{if } n = 1 \\ -1 & n > 1. \end{cases} \tag{4.15}$$

Using Eq. (4.12) and the values of $a_i$ and $b_i$ from Eq. (4.15), it is seen that,

$$F = \frac{K_i h_1}{2} + \frac{3K_s h_1}{2} + \frac{3}{2} K_s \overset{N-1}{\underset{i=1}{\mathrm{K}}} h_1. \tag{4.16}$$

Thus, $f_c$ can be obtained by substituting the value for $x_c$ into the above equation and normalising. Then, the results of this approximation can be compared to simulations, see Fig. 4.8.

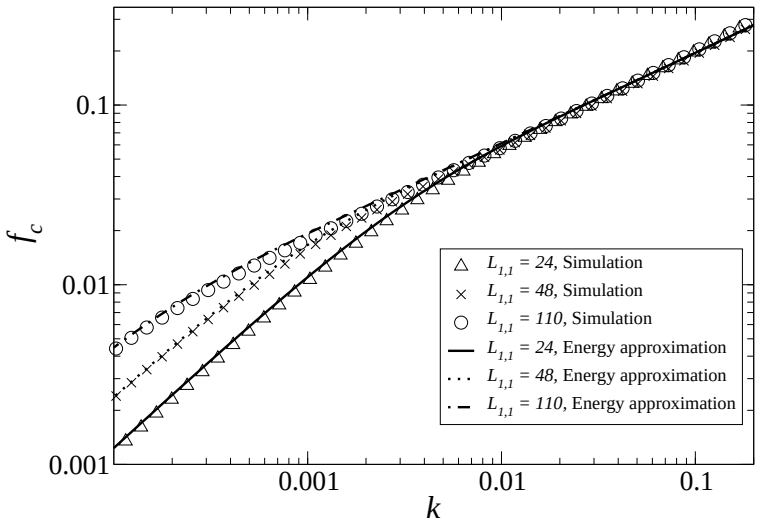


Figure 4.8: The dependence of $f_c$ on $k$ for a single lamella of various lengths. Good agreement is found between Eq. (4.16) and results of simulation. $f_c$ varies as $k^{0.5}$ for a range of $k$ before a linear relationship returns. Using Eq. (4.16) it can be shown that the half power-law region can be extended to infinitely small $k$ by taking $L_{1,1} \to \infty$.

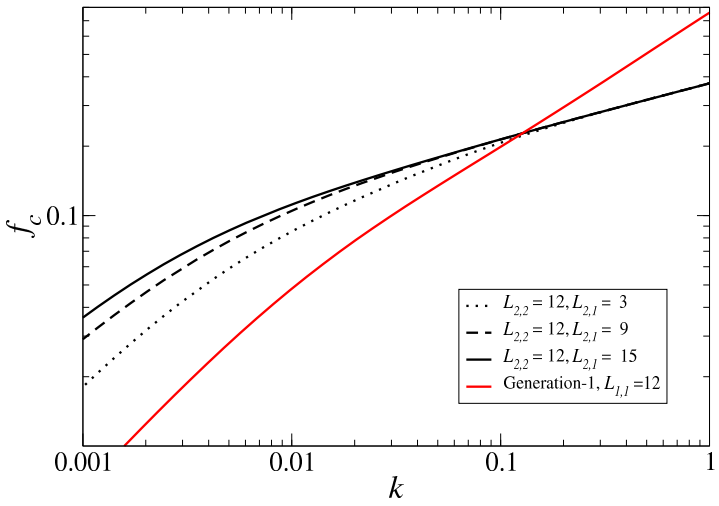


Figure 4.9: The dependence of $f_c$ on $k$ for the generation-2 structure for various values of $L_{2,1}$, also shown for comparison is the generation-1 structure in red.

### 4.4.3 Generation-2

In the case of higher generation structures, only a single lamella (rather than a surface of many, linked, lamellae) is considered. This reduces the computational power required to investigate the higher order structures while still retaining an accurate comparison between generations. In Fig. 4.9 it is seen the effect of adding the second generation lamella of length $L_{2,1}$, at a fixed angle $\frac{\pi}{4}$, on to the first order structure. Again an improved scaling law is found, here,

$$f_c \sim k^{0.25}. \tag{4.17}$$

In the limit of $k \to 0$ the linear relationship between $k$ and $f_c$ is observed. For comparison in Fig. 4.9 the curve of $f_c$ against $k$ for a single lamella of the generation-1 structure is shown with the primary lamella length the same as that of the generation-2 structure. It is again found that for $k > 0.1$ the lower generation structure is superior in terms of force required for separation. The range over which the one-quarter scaling-law is evident can be seen to increase with

increasing second order lamella length.

The restricted case of $L_{G,i} = \text{const}\,\forall\, i$ can also be investigated, this is shown in Fig. 4.10. It is found that with increasing values of $L_{2,1}$ and $L_{2,2}$ the functional dependence remains the same as in Eq. (4.17).

## 4.5 Discussion

It has been shown that the transition towards higher orders of hierarchy the scaling law relating the applied load at separation and value of $k$ can be altered in a systematic fashion. The structural advantages of the hierarchical design presented here are to be found in the region $k \ll 1$. The range of $k$ over which the improved scaling law can be observed is dependent on the length of lamellae at the interface. This work suggests that when engineering an interface to join two materials of differing Young's moduli, a hierarchical design may be beneficial in the limit of small adhesive interaction. Future work should investigate the effect of the hierarchical interface on the robustness of the structure. Although it is not expected to alter the results presented here, future work should also decrease the lattice spacing while keeping the dimensions of the structures constant to ensure isotropic material properties. Furthermore, dynamic simulations could be performed to give further insight into the behaviour of the interface in the equine hoof under locomotion.

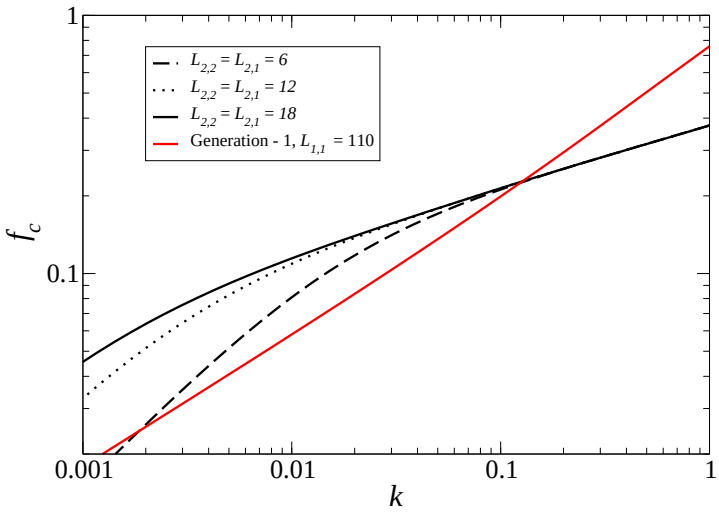


Figure 4.10: The dependence of $f_c$ on $k$ for the second generation lamella with various values of $L_{2,2} = L_{2,1}$. Also shown is the generation-1 structure for comparison of scaling. The generation-2 structure can be seen to exhibit scaling of $f_c$ with $k^{0.25}$ for a range of $k$, for $L_{2,2} = L_{2,1} \to \infty$ this scaling is expected to continue for all $k < 1$.

# Chapter 5

# Hierarchical design for efficient compression bearing structures: Fabrication and mechanical testing

## 5.1 Introduction

The two preceding chapters have shown two examples of creating efficient structures, under various loading conditions, using the principle of hierarchical design. Here, a design previously analysed [17] which has been shown to be a highly efficient compression bearing structure is fabricated. Nature has led the way in creating hierarchical materials for efficient load bearing structures; the structure of compact bone, for example, shows structural hierarchy over a range of length scales [9, 66]. In some cases it is found that this hierarchy is formed through the tissue's ability to restructure itself in response to prevailing stresses [66]. Through its hierarchical construction, high mechanical efficiency is retained while meeting

requirements of stiffness [67] and toughness [68].

Recent theoretical works, including that described in Chapter 3, have shown that through the use of hierarchical design, high mechanical efficiency can be obtained for structures under a range of loading conditions [17, 24, 25, 26]. In the limit of light loading, the optimal number of hierarchical levels increases without bound and the structure becomes fractal on all length scales. Experimental work on hierarchical sandwich panels has confirmed theoretical predictions that second order panels exhibit strength ten times greater than their first order counterparts of the same relative density [69].

Here, through simulation, the fundamental path of the structure is followed throughout the loading process to analyse the failure of the structure. The results of these simulations support the previously found scaling relationship between volume of material required to make a stable structure and applied compressive loading [17]. The relationship between failure mode and geometry of a structure is discussed and failure maps are presented for structures with one and two levels of structural hierarchy. Using rapid prototyping technologies an example frame is then constructed and its failure under compressive loading is compared to both freely hinged models and full finite element simulations. The differences between theory and experiment are discussed. Finally an additional design is proposed of a similar geometry to those fabricated here. The design of a fractal spaceframe constructed from hollow tubes is shown to yield further efficiency gains when compared with its solid beam counterpart.

## 5.2 Design and Basic Scaling Laws

The structure under investigation is a space frame, constructed through an iterative procedure where the generation, $G$, of the structure is defined as the number

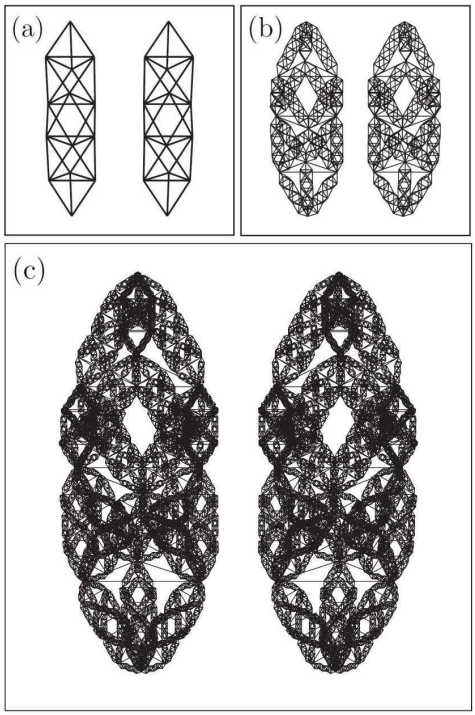


Figure 5.1: Example frames of (a) generation-1; (b) generation-2 and (c) generation-3. To view the stereograms in 3D hold the page 20cm away (30cm for the lower image) and look through the page, until the images merge.

of iterations performed [17]. The generation-1 structure is simply made up of two tetrahedra with $n$ octahedra between them, see Fig. 5.1(a). The generation-1 structure, when compressively loaded (and initially assuming all beams are pin jointed), has some of its component beams under compression and some under tension. More specifically, the horizontal beams are under tension while all others are under compression. The generation-2 structure is then constructed by replacing all beams in the generation-1 structure that are under compression with scaled generation-1 frames. This procedure is repeated to construct higher order frames, and Figs. 5.1(b)-(c) show example generation-2 and 3 structures. As in previous chapters, the naming convention for the parameters that are repeated on different length scales is such that $X_{G,i}$ refers to parameter $X$ in a frame of generation-$G$ at the $i$th level. For example, $n_{2,2}$ is the number of octahedra in a generation-2 frame on the longest length scale (which is in part made up of

generation-1 substructures), $n_{2,1}$ is the number of octahedra in the substructures of the generation-2 frame (which is constant for all the substructures used at this level). The parameters denoted in this way are number of octahedra in any frame or component structure, $n_{G,i}$; the length of a component beam or structure, $L_{G,i}$; the spring constant of a beam or substructure, $k_{G,i}$ and the force placed through a beam or substructure, $F_{G,i}$. In this notation when $i = 0$ the parameter refers to the simple beams that make up the smallest components. Making the assumption that all the component beams are freely hinged at their ends, the failure of each hierarchical level in this structure is decoupled entirely from all others. Thus, under this approximation, the only modes of failure that can interact are those within a single stack of octahedra; in the analytic formulation of this problem, it is assumed either buckling of a single component beam or buckling of the entire (sub)frame occurs first [17]. In this formulation, therefore, the generation-1 frame has two primary failure modes: failure of a component beam or failure of the entire frame, while a generation-2 frame has three failure modes: failure of an individual component beam, failure of a subframe of length $L_{2,1}$ or failure of the entire generation-2 frame. Using this approach, through iteration, optimisation of the whole structure can be achieved. The assumption that the failure of each hierarchical level occurs independently of its own substructure can be referred to as a 'continuum' model of the structure [69]. After the optimisation of the structure for the number of octahedra at each hierarchical level and the radius of the component beams, it can be shown that the minimum volume of material (scaled against the length, $L$, of the structure cubed: $v \equiv V/L^3$) required to create a space frame stable under compressive loading $F$ (scaled by the Young's modulus, $Y$, times by the length of the structure squared: $f \equiv F/YL^2$) scales as

[17]

$$v = \kappa_1(G) f^{\frac{G+1}{G+2}}, \tag{5.1}$$

where $\kappa_1(G)$ is a number which depends only on the generation of the structure.

Due to the nature of the $\kappa_1(G)$ dependence on $G$, it is found that, for a given value of loading, there is an optimal generation number for the structure which brings about the design of minimal mass. With a decrease in the loading parameter $f$, the optimal generation number is increased. The optimal generation in practical situations does not exceed four, and this, combined with the simple truss construction, makes the implementation of these designs plausible.

## 5.3 Scaling Laws

A computational model was constructed, assuming freely hinged joints, to calculate displacement caused in the frame by a compressive load. This model splits each component generation-1 (sub)frame into 3 constituent parts, the end tetrahedra, the octahedra connected to the end tetrahedra, and all other octahedra which were assumed to act identically, the number of degrees of freedom of the structure are reduced through considering the symmetry of the perfect structure. The model increments the force applied to the frame and calculates the displacement of each constituent part of the frame before incrementing the force further. Repeating this iteratively it is possible to obtain the idealised displacement of a generation-$n$ frame under the above assumptions. Such a method establishes whether the change in loading on the constituent beams is enough to invalidate the continuum assumption and therefore change the scaling law. Plotted in Fig. 5.2 are the results of these simulations alongside the analytic optimisations

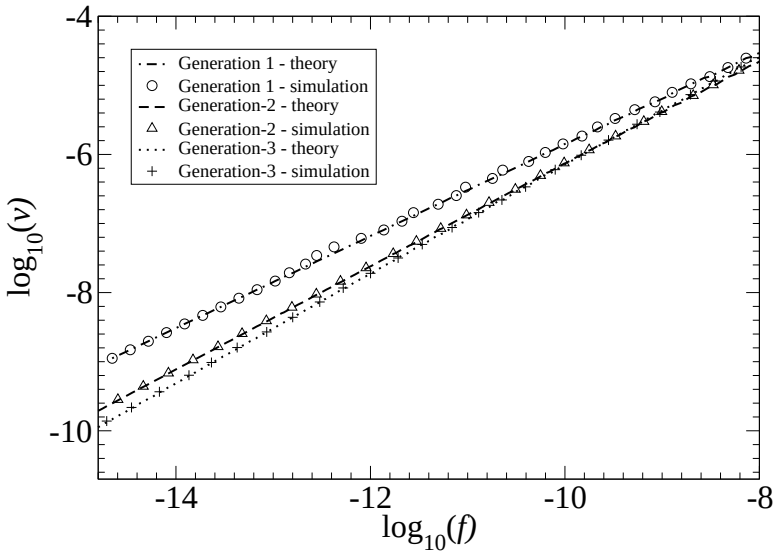


Figure 5.2: Scaling of non-dimensionalised volume $v$ versus the maximum non-dimensionalised loading $f$ for space frames with different generation numbers $G$. The theoretical results assume that the deformation prior to buckling is very small, while the simulations take this deformations into account, but still yield the same power-law scaling.

against loading showing the dependence of volume with loading and generation as described in Eq. (5.1). The results of a numerical study in Fig. 5.2 show that, though the individual beams are found to fail at a lower loading than that predicted analytically, the scaling law is still intact. The results shown in Fig. 5.2 are for spaceframes as shown in Fig. 5.1, while the frames fabricated in later sections of this work have the end tetrahedra removed at the highest hierarchical level. It is expected that, under the freely hinged approximation, the geometry changes under loading will not change this scaling relationship, since the change from pin jointed to essentially clamped boundary conditions only affects the largest hierarchical level, and introduces a single pre-factor in the Euler buckling criterion.

The previous analyses [17] assume that all component beams in the structure fail due to Euler buckling, and that yield of the material is not important in the optimisation procedure. This assumption is shown to be valid in Fig. 5.3

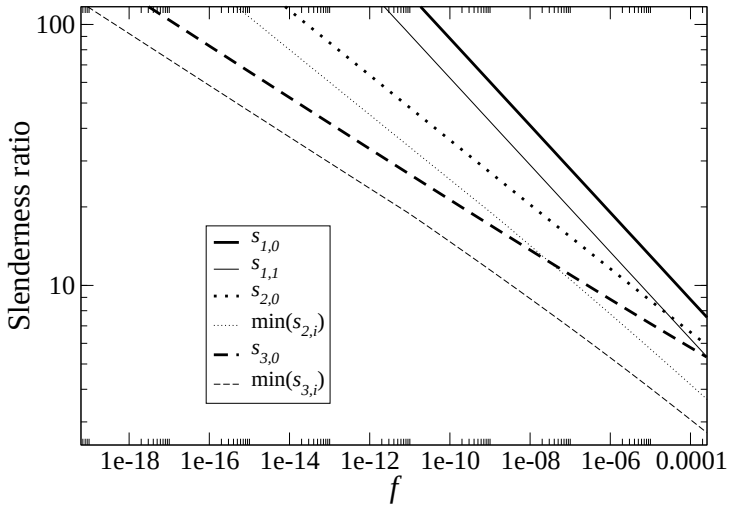


Figure 5.3: Slenderness ratio of frames for generation-1 to 3 against loading parameter for which the frame is optimised. As the loading decreases, the slenderness ratio increases. This implies where the frames are most efficient it is possible to discount yield as a source of failure of the component beams

where the slenderness ratio of the smallest beams, $s_{G,0}$, is plotted against the loading parameter for which the frame is optimised. Also plotted in Fig. 5.3 is $\min_{i>0}(s_{G,i})$, where $s_{G,i}$ is the maximal distance from the neutral axis of a (sub)frame to any component part of that (sub)frame for the hierarchical level $i$ divided by $L_{G,i}$: $s_{G,i}$ represents the slenderness of the (sub)frames. As the loading parameter becomes smaller, and thus where the frames are most efficient, it is observed that the substructures become more slender.

## 5.4 Failure mode

A generation-$G$ structure will have $G+1$ types of failure mode from Euler buckling at each structural level, and it is assumed in the optimisation that each failure mode is independent of the features on different length scales - this is a result of the freely hinged approximation which decouples the failure of one hierarchical level from all others in this class of structures. Through simulation a failure map

of the structures can be constructed in order to predict which failure mode will be active for a given geometry. As discussed previously, the generation-1 structure has only two primary modes of failure (buckling of the whole structure treated as a single column, and buckling of the individual component beams). Furthermore for a given length $L_{1,1}$ of structure, the geometry is fully defined by $r_{1,1}$ and $n_{1,1}$. Thus, by plotting $\frac{r}{L_{G,0}}$ against $n_{1,1}$ one can obtain a map for which failure mode is likely to be active for any given geometry. Through consideration of volume for these geometries, the unique optimal design parameters for a given loading can be obtained. Fig. 5.4 shows the evolution of the optimal design with varying loading criteria: as the value of loading decreases, the number of octahedra in the optimal design increases and the radii of the beams decrease.

The generation-2 structure has three classes of failure mode. For a given volume, $V$, and length of structure, $L_{2,2}$, the parameters $n_{2,2}$ and $n_{2,1}$ fully define the structure; it should be noted in the resulting plot, Fig. 5.5, that the parameter $r$ varies in order to keep $V$ constant. For a given volume the optimal construction is found when the structure is on the point of failure on all length scales, and contours of constant loading failure are also shown in the figure.

## 5.5 Fabrication and Testing

To test the structure, the largest length scale tetrahedra at each end are replaced with planar surfaces, which provides a more suitable mechanical coupling: through this adaptation loading eccentricities are reduced. The structure was fabricated through rapid prototyping on an EnvisionTEC perfactory machine (EnvisionTEC, 45968 Gladbeck, Germany) using EnvisionTEC RC25 (NanoCure) material; a second set manufactured on the same machine using EnvisionTEC R05 material. Each structure has dimensions of approximately 40mm x 11mm x

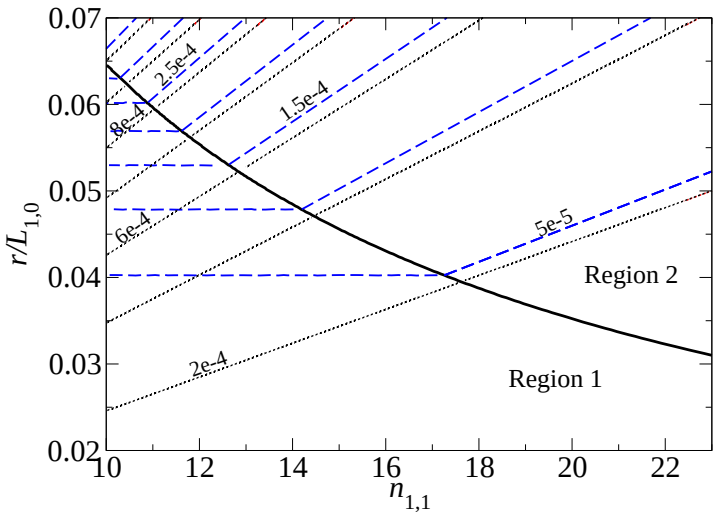


Figure 5.4: Through plotting $n_{1,1}$ and $r/L_{1,0}$ a failure map for the generation-1 structure valid for all values of $L_{1,1}$ is obtained. The figure is split into two regions: region 1 shows the geometries which lead to failure of the smallest beams in the structure, while region 2 shows where the structure is predicted to fail due to global failure of the frame. The black curve shows the set of optimal geometries. Also shown are contours of constant non-dimensional failure loading ($F/(YL_{1,0}^2)$) separated by values of $5 \times 10^{-5}$ indicated with blue dashed lines and constant non-dimensional volume, $V/L_{1,1}^3$, separated by values of $2 \times 10^{-4}$ shown in red dotted lines. Though here $n_{1,1}$ is shown to take a continuous set of values, in reality only integers values can be realised.

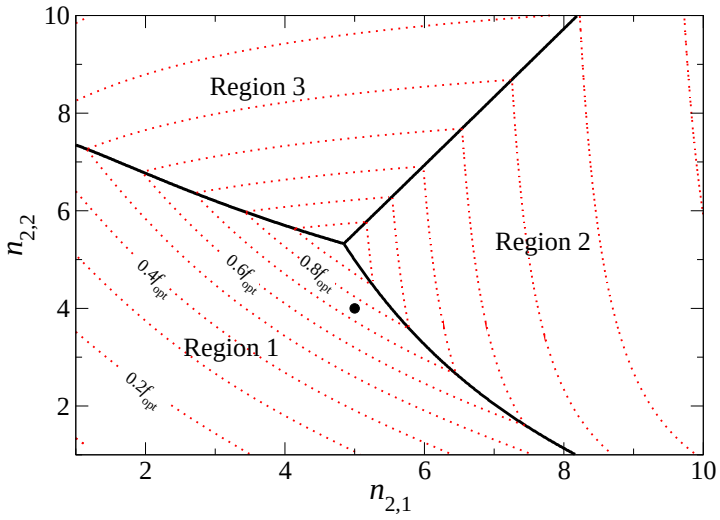


Figure 5.5: Showing the predicted mode of failure for an adapted generation-2 structure with non-dimensional volume of $v = 9.3 \times 10^{-3}$ and an optimal failure loading parameter of $f_{\text{opt}} = 3.07 \times 10^{-3}$. The area of the plot is separated into three regions: region 1 shows the values of $(n_{2,1}, n_{2,2})$ where the smallest solid beams in the structure will fail first, region 2 is such that the substructure generation-1 frames will fail first, and region 3 shows the parameters which put the generation-2 frame of length $L_{2,2}$ fail first. The red dotted lines show the contours of constant failure at loading which are separated by 0.1 times the optimal loading value. The black circle shows the geometry of the structure manufactured here. In the construction of space frames, $n_{2,2}$ and $n_{2,1}$ are restricted to integer values.

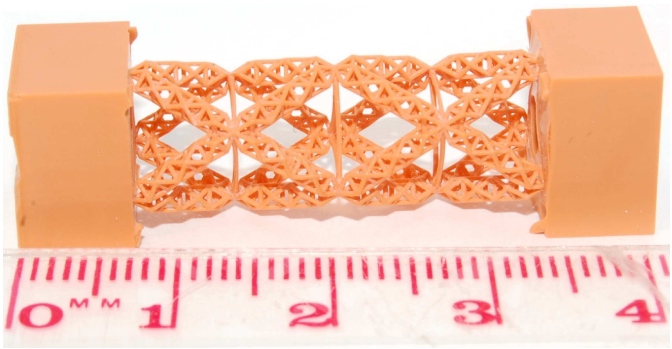


Figure 5.6: The generation-2 frame. The final frame was built without the top tetrahedron and with a plate attached to both top and bottom to allow reliable compression tests to be undertaken.

11mm including the end plates. The dimensions of the smallest struts within the structure were approximately 1.35mm long with radius of 0.15mm, Fig. 5.6 shows an example structure. The build process using the RC25 (NanoCure) material was undertaken using two different layer thicknesses, 35$\mu$m and 50$\mu$m while the R05 material was manufactured using a layer thickness of 25$\mu$m. The difference in performance of the structures is analysed in the Discussion section. The compression tests are undertaken at a constant compression rate while the reaction forces are measured; the compression rate for all compression tests is 1.2$\mu$m s$^{-1}$ using an Instron 5569 machine, Fig. 5.8 shows the set up used.

## 5.6 Fabrication

The structures tested here were fabricated using a modified EnvisionTEC Perfactory ® type III mini system. This mask-projection based photopolymerisation system has a 2800 $\times$ 2100 pixel digital light processing projector allowing a resolution of 5$\mu$m. The structure manufactured here was first modelled as an STL file as a 3D structure, before being split into its component 2D layers of a given thickness and stored as a job file using Perfactory RP proprietary software. Light with wavelength approximately 475nm is then passed through the projector and focused onto the resin surface for polymerisation of the exposed areas. The sample is then washed using ispropanol in an ultrasonic bath and left to dry. For the structures made from R05 a postcuring procedure is followed using an EnvisionTEC Otoflash System to harden the material.

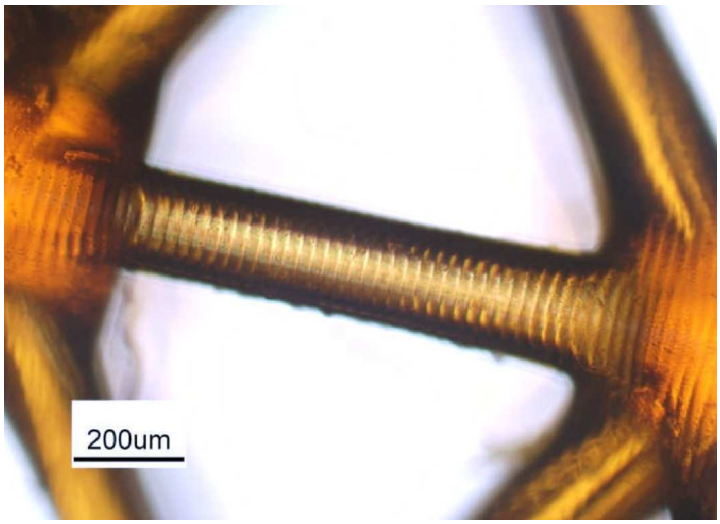


Figure 5.7: Close-up of the structure of Fig. 5.6. The layering of the R05 material is clearly visible in this microscope image. Image taken using a Nikon Optiphot at a magnification of x10. The image also clearly shows the extra material deposited around the joints

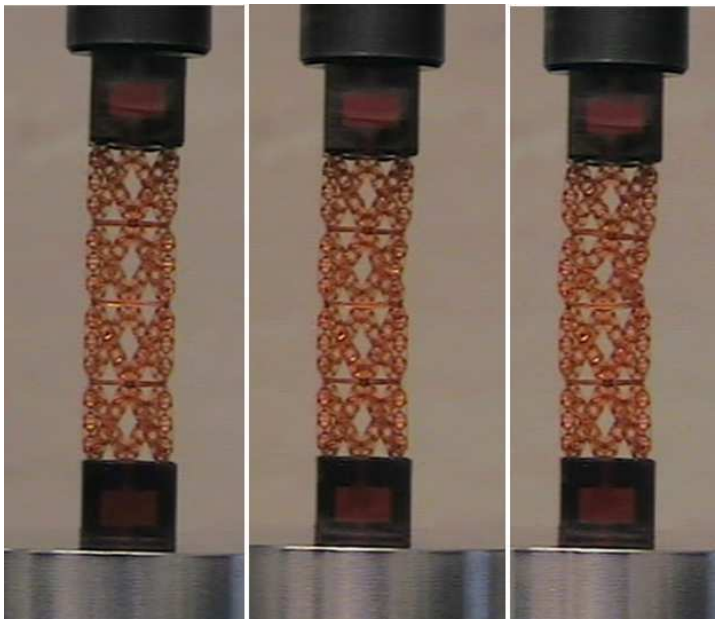

Figure 5.8: The set-up used for the compression tests and the modified structure with end tetrahedra replaced by planar surface. Structures in compression tests shown are those made out of R05 and images taken at 3 different time intervals (from left to right): the first is before loading; the second at the point of first failure, where the second substructure from the top is seen to be deformed (due to failure of a smaller component beam); in the third image the deformation is seen throughout the top half of the structure.

## 5.7 Results

Due to the manufacturing process, the material has a clearly visible layered texture (see Figs. 5.7, 5.13). This leads to anisotropic material performance under stress and different behaviour of the material to that observed when testing its bulk properties [70, 71, 72]. In analysing our compression results an 'Effective Young's Modulus', $Y_{\text{eff}}$ is introduced for the material to compensate for the altered performance of the structure due to the layering effect. The Effective Young's Modulus is taken such that the deformation of the structure at very small displacements is in line with the results of finite element simulations. The normalised results are then plotted in Figs. 5.9 & 5.10 for frames manufactured in both the R05 and the RC25 (NanoCure) materials alongside the theoretical result with a linear displacement assumption, the freely hinged model which neglects bending effects of the beam, and a full finite element simulation of the structure. This finite element simulation was undertaken using ANSYS 13.0. Using this commercial package a linear buckling analysis precedes a full non-linear analysis using in built routines. A model of the structure was constructed using linear beam element (BEAM118 - based on Timoshenko beam theory) using automatic meshing with the mesh size varied to ensure convergence. Boundary conditions were taken such that all degrees of freedom (translation and rotation) were restricted at one end of the frame (missing the tetrahedral end cap) while all rotations and displacement in the $x$-$y$ plane were restricted at the loaded end, only translations in the $z$-direction were permitted. The difference between the linear analysis and the maximum loading of the path shown in Figs. 5.9 & 5.10 is found to be approximately 35%. The scaling of $f$ and $x/L$ is such that the finite element analysis curves plotted in Figs. 5.9 & 5.10 do not change between the materials with different $Y$ values, the Poisson ratio of the material is taken to be 0.3. In

both cases, the failure point of the finite element curve indicates a loss of elastic stability. In mechanical testing, it is found that for the frame constructed using the RC25 (NanoCure) material the failure occurs through breaking of the longer tension beams in the structure, these breaks are represented by vertical steps in the path of displacement against load for the compression tests in Fig. 5.9. Taking into account the failure under tension at 2.5% elongation (bulk material properties) it is shown that this failure mode is predicted to occur first in the freely hinged model (see Fig. 5.9) however it is not predicted in the finite element simulations (the finite element simulation predicts a maximal elongation of these tension beams of 1.8%). It is understood that the layered nature of the material due to the manufacturing process will have a greater effect on failure due to tension, as any lack of adhesion between the layers will have an amplified effect when placed under tension. The R05 material can withstand an elongation great enough to test the failure mode predictions from buckling made previously. Fig. 5.5 shows that failure due to the smallest beams should be the active mode. This is indeed found to be the case in experiment giving qualitative agreement between theory and experiment. The value of $Y_{\text{eff}}$ differs depending on the layer thickness. The values of $Y_{\text{eff}}$ for the RC25 (nanocure) material are found to be:

$$Y_{\text{eff}} = 2.2GPa \pm 0.1 \tag{5.2}$$

$$Y_{\text{eff}} = 1.5GPa \pm 0.05 \tag{5.3}$$

for layer thicknesses of 50$\mu$m and 35$\mu$m respectively. While the value of $Y_{\text{eff}}$ for the R05 material with layer thickness of 25$\mu$m is found to be

$$Y_{\text{eff}} = 0.5GPa \pm 0.1. \tag{5.4}$$

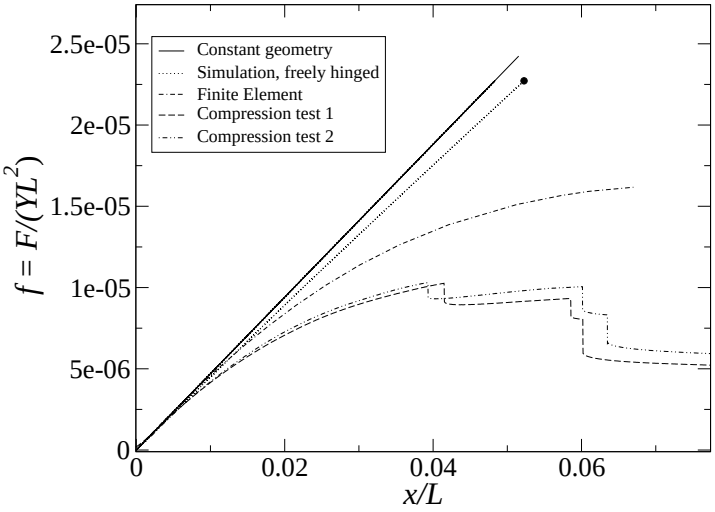


Figure 5.9: The results of the compression tests for two structures made from the RC25 (nanocure) material with layer thickness 35$\mu$m against theory and simulations. The black circle indicates where the freely hinged model would fail due to fracture of the tension beams of length $L_{2,1}$ in accordance with the material properties; the structure reaches the point of failure due to the breaking of the long tension beams before the smallest beams in the structure buckle.

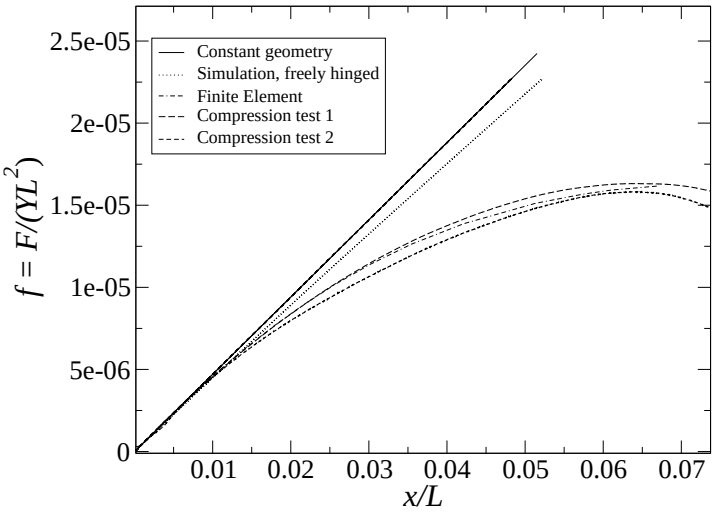


Figure 5.10: The results of the compression tests for two structures manufactured using R05 with layer thickness 25$\mu$m against theory and simulations. The failure here is due to the smallest beams in the structure failing by buckling.

## 5.8 Further Applications

Here it is investigated whether further gains in efficiency can be obtained through constructing a frame with the same geometry as above out of hollow tubing. The construction of frames using a photosensitive polymer can be used in conjunction with other techniques such as electroless nickel plating and etching to create frames of the same geometry but using hollow, metallic tubing [73, 74, 75].

### 5.8.1 Generation-0

To serve as a reference the amount of material that is required to construct a simply supported beam of length $L$, stable under a compressive load $F$ is considered. As before we define non-dimensional loading and volume parameters:

$$f \equiv \frac{F}{Y L_{G,G}^2}, \tag{5.5}$$

$$v \equiv \frac{V}{L_{G,G}^3}, \tag{5.6}$$

where $Y$ is the Young's Modulus of the material, and $V$ is the volume of the structure. It is important to note that in all practical applications, both these non-dimensional parameters are much smaller than 1. If the beam is made up of solid material the only restriction to loading is given by Euler [4],

$$F < \frac{\pi^2 Y I}{L^2}, \tag{5.7}$$

where $I$ is the second moment of area. Given a circular cross section of beam ($I = \frac{\pi r^4}{4}$) it is straightforward to show,

$$v \sim f^{\frac{1}{2}}. \tag{5.8}$$

If instead the circular beam is taken to be hollow, two restrictions are seen to apply to the loading: first, that of Eq. (5.7) with $I = \frac{\pi((r+t)^4 - r^4)}{4}$ where $t$ is the thickness of the cylinder wall and secondly, a short wavelength failure mode must be considered, Koiter buckling [49], giving a second inequality:

$$F < \frac{2\pi Y t^2}{\sqrt{3(1-\nu^2)}}, \tag{5.9}$$

where $\nu$ the Poisson ratio. Setting the geometry of the beam to be such that Euler buckling and Koiter buckling occur at the same value of loading, it is straightforward to show that

$$v \sim f^{\frac{2}{3}}. \tag{5.10}$$

In the regime $f \ll 1$ this change in scaling law represents a saving in material over the solid beam. In this section, it is the hollow beam that will be termed the generation-0 design.

### 5.8.2 Scaling for hollow generation-1 structure

As stated previously, the generation-1 structure is a simple space-frame made up of $n_{1,1}$ octahedra and two end tetrahedra and is shown in Fig. 5.1 (a). Defining the length of the whole structure to be $L_{1,1}$, and the length of a constituent beam to be $L_{1,0}$, it is seen that

$$L_{1,1} = \sqrt{\frac{2}{3}}(n_{1,1} + 2)L_{1,0}. \tag{5.11}$$

Assuming all beams in the structure to be made up of identical beams which perform in a Hookean manner for loading less than the Euler limit and whose

spring constant is given by,

$$k_{1,0} = \frac{YA}{L_{1,0}}, \tag{5.12}$$

where $A$ is the cross-sectional area of the beam, the whole frame can be seen to have a bending stiffness ($YI$) and spring constant given by:

$$YI = BL_{1,0}^3 k_{1,0}, \tag{5.13}$$

$$k_{1,1} = \frac{36k_{1,0}}{11n_{1,1} + 43}, \tag{5.14}$$

respectively, where $B$ is a constant found to be $B = 0.254 \pm 0.001$ [17]. The structure is oriented such that the end points of the tetrahedra are aligned along the $z$-axis in Cartesian coordinates and on loading these end points with a force $F_{1,1}$ in a compressive manner, it is found that that all beams parallel with the $x - y$ plane are under tension. Assuming $n \geq 2$ the beams under tension making up the end tetrahedra support a load of $\frac{F_{1,1}}{2\sqrt{6}}$ while other tension members support a load of $\frac{F_{1,1}}{3\sqrt{6}}$. It is found that all other beams support a compressive load. The beams connected to the end points are acted on by a force of

$$F_{1,0} = \frac{F_{1,1}}{\sqrt{6}}, \tag{5.15}$$

while, all other beams under compression take half this loading each. Defining

$$f_0 = \frac{F_{1,0}}{YL_{G,0}^2}, \tag{5.16}$$

and stating that the beams connected to the loading points of the structure are on the point of failure due to both Euler and Koiter buckling, through use of

Eqs. (5.7, 5.9, 5.15 & 5.16) it follows that:

$$t = L_{G,0}\left(\frac{\sqrt{3\left(1-\nu^2\right)}f_0}{2\pi}\right)^{\frac{1}{2}}, \tag{5.17}$$

$$r = L_{G,0}\left(\frac{2f_0}{\pi^5\sqrt{3(1-\nu^2)}}\right)^{\frac{1}{6}}. \tag{5.18}$$

Then, using Eqs. (5.11 - 5.13 & 5.15 - 5.18) and setting the whole space-frame to be on the point of Euler buckling, it is found that

$$n_{1,1} = -2 + \left\lfloor \frac{6^{\frac{1}{4}}\pi^{\frac{5}{6}}B^{\frac{1}{2}}\left(3\left(1-\nu^2\right)\right)^{\frac{1}{12}}f_0^{-\frac{1}{6}}}{2^{\frac{2}{3}}} \right\rfloor, \tag{5.19}$$

where $\lfloor\cdot\rfloor$ is the floor function ($\text{floor}(x)$ is largest integer not greater than $x$). Then, using Eqs. (5.11 & 5.15) it is found that,

$$f = \frac{3\sqrt{6}}{2}(n_{1,1}+2)^{-2}f_0, \tag{5.20}$$

and using Eqs. (5.11, 5.18, 5.17), the non-dimensional volume is found to be,

$$v = 27\sqrt{6}\frac{(n_{1,1}+1)f_0^{\frac{2}{3}}\left(3\left(1-\nu\right)\right)^{\frac{1}{6}}}{\pi^{\frac{1}{3}}2^{\frac{4}{3}}\left(n_{1,1}+2\right)^3}, \tag{5.21}$$

thus,

$$v = \kappa_1 f^{\frac{3}{4}}. \tag{5.22}$$

### 5.8.3 Generation-$n$ optimisation

As described in Sec. (5.2) the generation-$n$ structure can be created through an iterative procedure. In creating the generation-1 structure, the simple, hollow beam that makes up the generation-0 structure is replaced with a space-frame. It is an

analogous step that takes us from the generation-1 structure to the generation-2 structure: all simple beams in the structure under compression are replaced by (scaled) generation-1 frames. The generation-2 and 3 structures are shown in Fig. 5.1 (b) and (c).

Following the notation introduced in Sec. (5.2), for $i > 1$, it can be shown that the properties of the frame are given by [17]:

$$L_{G,i} = \left(\frac{2}{3}\right)^{\frac{1}{2}} (n_{G,i} + 2) L_{G,i-1} \tag{5.23}$$

$$YI_{G,i} = BL_{G,i-1}^3 k_{G,i-1} \tag{5.24}$$

$$k_{G,i} = \frac{36 k_{G,i-1}}{11 n_{G,i} + 43} \tag{5.25}$$

$$F_{G,i} = \sqrt{6} F_{G,i-1}. \tag{5.26}$$

It is seen that to avoid Euler buckling at each hierarchical length scale, the constraint,

$$F_{G,i} < \frac{\pi^2 Y I_{G,i}}{L_{G,i}^2}, \tag{5.27}$$

must be imposed for all $i$. Given that the smallest beams are made of hollow tubes, the possibility of Koiter buckling must be taken into account, this constraint on loading provides us with the inequality stated in Eq. (5.9).

Then, defining the geometry such that Euler buckling and the short wavelength Koiter buckling occur simultaneously in the beams of length $L_{G,0}$, through use of Eqs. (5.9, 5.16 & 5.27), with $i = 0$ it can be shown that the expressions for $t$ and $r$ given in Eqs. (5.17 & 5.18) are still valid for the higher generation structures. Then using Eqs. (5.16 - 5.18, 5.23, 5.24, 5.26 & 5.27), setting all (sub)frames to be on the point of failure due to Euler buckling, it can be ob-

served that,

$$n_{G,1} = -2 + \left\lfloor \frac{6^{\frac{1}{4}} \pi^{\frac{5}{6}} B^{\frac{1}{2}} \left(3\left(1-\nu^2\right)\right)^{\frac{1}{12}} f_0^{-\frac{1}{6}}}{2^{\frac{2}{3}}} \right\rfloor, \tag{5.28}$$

and, for $i > 1$,

$$n_{G,i} = -2 + \left\lfloor \left( \frac{\sqrt{6}}{2^{\frac{4}{3}}} \pi^{\frac{5}{3}} B (3(1-\nu^2))^{\frac{1}{6}} f_0^{-\frac{1}{3}} \right. \\ \left. 12^{i-1} \prod_{j=1}^{i-1} \frac{n_{G,j}+2}{11 n_{G,j}+43} \right)^{\frac{1}{2}} \right\rfloor. \tag{5.29}$$

It is chosen that the radius of the beams under tension at each hierarchical level are such that the spring constant of the simple beams of length $L_{G,i}$ are equal to the spring constant of the space-frame of an equal length ($t$ remains constant for the whole structure). Therefore, using Eqs. (5.12, 5.23 & 5.25) it can be seen that

$$s_{G,i} = (12\sqrt{6})^i \prod_{j=1}^{i} \frac{n_{G,j}+2}{11 n_{G,j}+43} r \tag{5.30}$$

where $s_{G,i}$ is the value of the radius of the beams of length $L_{G,i}$ under tension. For $G > 1$, it is found that,

$$f = \left(\frac{27}{2}\right)^{\frac{G}{2}} f_0 \prod_{j=1}^{G} \left(n_{G,j}+2\right)^{-2} \tag{5.31}$$

$$v = \left(\frac{9\sqrt{6}}{2}\right)^{G} \frac{f_0^{\frac{2}{3}} (3(1-\nu^2))^{\frac{1}{6}}}{2^{\frac{1}{3}} \pi^{\frac{1}{3}}} \prod_{k=1}^{G} \frac{n_{G,k}+1}{(n_{G,k}+2)^3} \\ \left[ 3 + \sum_{q=1}^{G-1} 4^q \prod_{j=1}^{q} \frac{(n_{G,j}+2)^2}{(11 n_{G,j}+43)(n_{G,j}+1)} \right] \tag{5.32}$$

Where, to obtain the former equation, Eqs. (6.3, 5.23, 5.26 & 5.16) were used, and in the latter, Eqs. (5.6, 5.17, 5.18 & 5.23). The scaling of material required to

make a stable structure out of hollow tubes, to leading order, is therefore shown to obey:

$$v = \kappa_2(G) f^{\frac{G+2}{G+3}}. \tag{5.33}$$

For $f \ll 1$, this design shows gain in scaling efficiency over the structure described in section 5.2 equivalent to raising the generation of a structure by one. These scalings are demonstrated in Fig. 5.11 for various values of loading.

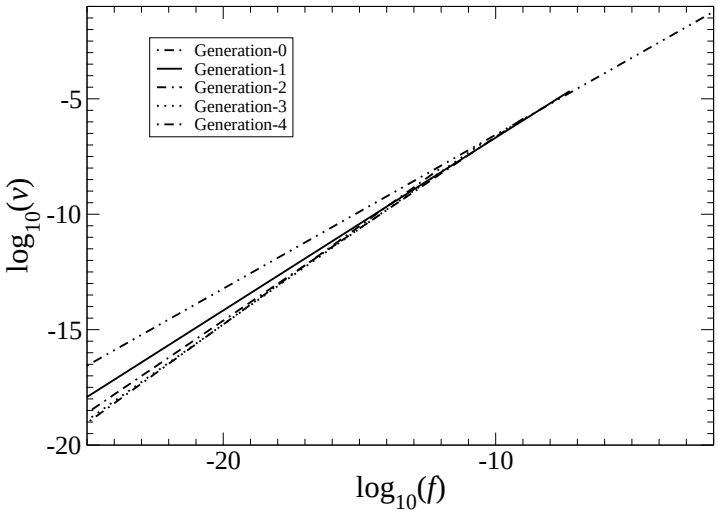


Figure 5.11: Volume required for structural stability against loading for which the structure is optimised, showing generation-0 to 4. Higher generations become optimal as the force decreases.

## 5.9 Discussion

It is seen from Fig. 5.10 that the deformation of the R05 structure is very close to that predicted by the finite element simulation; in the case of the RC25 (Nano-Cure) material, Fig. 5.9, both the strain at failure and the deformation at failure is much lower than predicted by these models. This difference in behaviour can be attributed to the different nature of the failure in the two materials and the

layered texture of the material giving inhomogeneous behaviour under tension in particular [70, 71]. The loading at failure in both cases differs significantly from the freely hinged results. This difference must be investigated further to establish whether the addition of bending moments at the beam ends is enough to invalidate the previously found scaling laws.

It is noted that the deformation of the structure as predicted by the simple freely hinged model method agrees with the full finite element model very well until the loading reaches a threshold value and the effects of bending moments at the end of the beams become important. When the structure is tested physically it is seen that this proportional limit is shifted to a lower value of the loading parameter for the RC25 (NanoCure). This can be explained through the presence of excess material around the joint and the non-uniform beam thickness. The difference between the freely hinged model and the finite element simulation is down to the beams being modelled as free to hinge at the joints in the former and not in the latter. The difference between the actual testing can, in part, be attributed to an amplification in this effect due to the excess material where beams meet. This excess material is shown clearly in Fig. 5.12. Good agreement is obtained between the finite element simulation and the physical testing of the structure made using R05 material. It is also important to note that any imperfections in the material will be amplified by the structure's dependence on structural elements much smaller than its own length. The nature of the RC25 (NanoCure) material is such that failure is due to the breaking of the beams loaded under tension rather than any of the compression beams failing - this does not invalidate the 'continuum' approximation.

In summary, optimal hierarchical space frames have been designed based on freely hinged couplings between component beams. Then finite element simulations and physical measurements have been performed on structures to find the

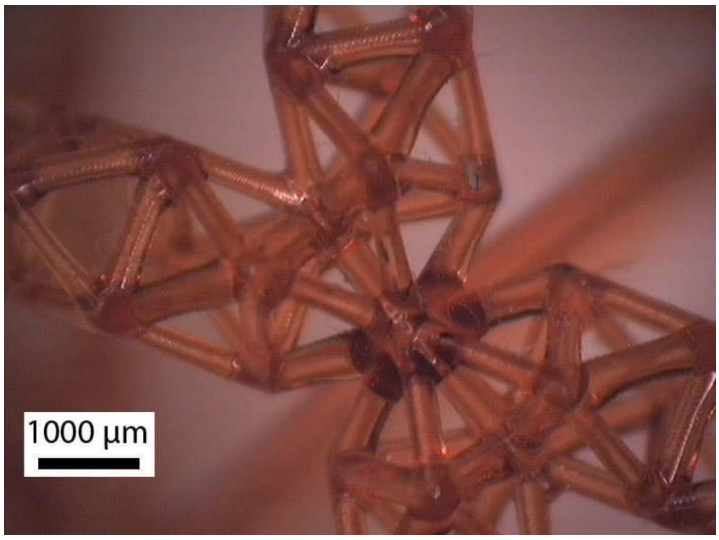


Figure 5.12: The joints of the frame have excess material around them which contributes the differences between simulation and the test results. A structure constructed using the R05 material is shown in this figure.

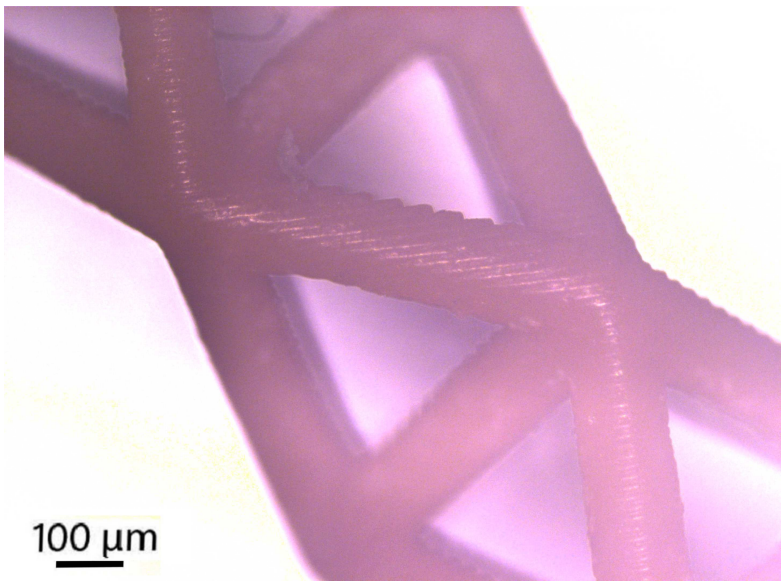


Figure 5.13: The RC25 (nanocure) material clearly showing the layering effect of the manufacturing process on the structures surface and a more opaque appearance than the R05 material.

failure modes once this freedom at the joints is removed. Despite potential non-uniformity of the resins used to make the physical structures, the finite element analysis agrees well with the experimental results on the R05 material (although R25 is brittle under tension and so gives less good agreement). However, the analysis of freely hinged structures predicts that they will fail at higher compression forces and lower strains than those obtained by finite element analysis (and experiment) without freely hinged joints. In future therefore investigations into the optimal form of non-freely hinged hierarchical space frames should be undertaken, to determine whether the scaling laws for the material required to support a given compression force that apply to the freely hinged case still hold true. A further design, based on that fabricated here has been proposed. It has been shown that through constructing the frame out of hollow tubing, the relationship between material required for stability and force withstood can be altered in a beneficial manner. A proven fabrication method has also been put forward for such a construction.

# Chapter 6

# The Effect of Imperfections in a Hierarchical Structure

Uncertainties are inherent in any engineering problem: the deviation of parameters describing a structure from their theoretical ideal is inevitable [76]. In attempting to create structures of high efficiency, these inevitable initial imperfections can result in problems of reliability [77]. The technique of naïve optimisation, used in previous chapters, is a useful tool in creating theoretical bounds for efficiency of structures; it is often the case, however, that through its implementation high imperfection-sensitivity is introduced [77]. It is therefore essential that the imperfection-sensitivity of the hierarchical designs presented previously are investigated before their use becomes practical [17, 78].

Here a two-dimensional example of a hierarchical frame is presented before the effect of a perturbation to a single, central beam is analysed. The effect of this imperfection is found for a generation-1 and 2 structure. The two-dimensional frame, while not itself of engineering significance, is seen to have many of the attributes of its three-dimensional counterpart (for example, that fabricated in Chapter 5). Thus, understanding its behaviour in load bearing situations illumi-

nates the probable behaviour of more practical structures.

The structures considered in this chapter are typically referred to as imperfection-insensitive [79], this classification also applies to its 3-dimensional counterpart constructed in Chapter 5. Such structures exhibit behaviour whereby, while the perfect structure encounters a critical point at some point along the path of equilibrium, the fundamental path of the imperfect structure remains stable throughout the loading process [77, 79]. These designs are often limited by excessive deflection [79]. It is found that in the case of the optimised structures considered here, the deflection of the imperfect structure on a global scale causes extra loading on the substructures and thus causes a local failure. While the structure is, globally, imperfection insensitive, local buckling gives an alternative, natural, failure definition.

## 6.1 Optimisation of perfect hierarchical frame

The notation in this chapter will follow that used in the previous 3 chapters, $X_{G,i}$ represents the parameter $X$ at the $i$-th hierarchical level (0-th being the smallest and $G$-th being the largest) of a generation-$G$ structure.

### 6.1.1 Generation-0

For the purposes of comparison, a simple beam, in 2-dimensions, of length $L_{0,0}$, will be termed a generation-0 structure. A freely hinged beam will fail when the applied load, $F$, on the beam reaches the Euler buckling load [4, 21],

$$F = \frac{\pi^2 Y I}{L^2}, \tag{6.1}$$

where, as before, $Y$ is the Young's Modulus, $I$ is the second moment of area and $L$ is the length of the beam. A beam of thickness $t$ in two-dimensions can be seen to have a second moment of area,

$$I = \frac{t^3}{12}. \tag{6.2}$$

Then, defining:

$$f \equiv \frac{F}{Y L_{G,G}}, \tag{6.3}$$

$$v \equiv \frac{V}{L_{G,G}^2}, \tag{6.4}$$

it is straightforward to show that in the case of a simple generation-0 structure the scaling of material required to make a stable structure ($v$), under the non-dimensional load ($f$) is

$$v \sim f^{1/3}. \tag{6.5}$$

In all practical applications $f \ll 1$, thus, higher powers in the above equation lead to a decrease in the required volume to create a stable structure under a given non-dimensional value loading.

### 6.1.2 Generation-1

Here the generation-1 structure is a simple spaceframe, with end-points at $(0, 0)$ and $(0, L_{1,1})$, the length of each constituent vertical beam is $L_{1,0}$ (see Fig. 6.1). The compressional loading of the entire spaceframe is $F_{1,1}$, thus, on one of the vertical constituent beams of length $L_{1,0}$ the loading (in the limit of zero loading)

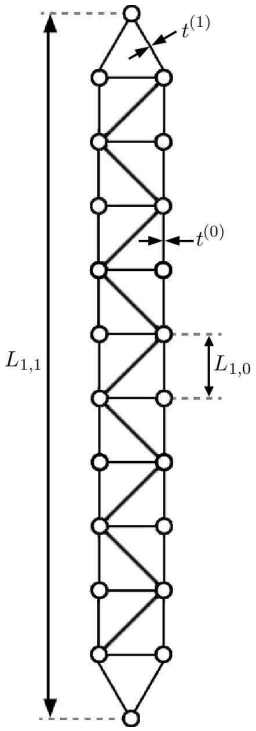


Figure 6.1: The generation-1 structure and the notation used throughout this chapter.

is simply

$$F_{1,0} = \frac{F_{1,1}}{2}. \tag{6.6}$$

It can be seen that the generation-1 structure has two modes of failure: the first, a local failure of a constituent beam; the second, a global failure of the whole structure. Here, for convenience

$$f_0 \equiv \frac{F_{G,0}}{Y L_{G,0}}. \tag{6.7}$$

is defined. Using Eqs. (6.1, 6.2, 6.6 & 6.7), it is found that the thickness of the constituent vertical beams such that they are on the point of failure by Euler

buckling is given by,

$$t^{(0)} = L_{1,0}\left(\frac{12f_0}{\pi^2}\right)^{\frac{1}{3}}. \tag{6.8}$$

Due to the geometry of the frame, the end beams support an increased loading when compared to the vertical beams. They also span a greater length, so an increased value of $t$ is required for stability,

$$t^{(1)} = L_{1,0}\left(\frac{15\sqrt{5}}{2}\frac{f_0}{\pi^2}\right)^{\frac{1}{3}}. \tag{6.9}$$

Given the length of the vertical beams is related to the length of the generation-1 frame by,

$$L_{G,1} = (n_{G,1} + 2)L_{G,0}, \tag{6.10}$$

and the second moment of area is approximated by,

$$I_{G,1} \approx \frac{tL_{G,0}^2}{2}, \tag{6.11}$$

where $t$ is the thickness of the central, vertical beams in the frame, using Eqs. (6.1, 6.9), it can be shown that for the whole structure to be on the point of global failure,

$$n_{1,1} = -2 + \sqrt{\frac{\pi^{4/3}12^{1/3}}{4f_0^{2/3}}}. \tag{6.12}$$

Then, using Eqs. (6.3, 6.6, 6.7 and 6.10), it is found that,

$$f = \frac{4f_0^{4/3}}{\pi^{2/3}12^{1/6}}, \tag{6.13}$$

and using Eqs. (6.4, 6.8, 6.9 and 6.12),

$$v = \frac{2\left(3+\sqrt{2}\right)2^{1/3}3^{1/6}}{\pi^{4/3}} f_0^{2/3} - \frac{8(1-\sqrt{2})+4\sqrt{5}}{\pi^2} f_0. \tag{6.14}$$

Thus, to leading order,

$$v \sim f^{1/2}, \tag{6.15}$$

showing greater efficiency in the limit of light loading when compared to the generation-0 structure.

### 6.1.3 Generation-2

The generation-2 frame can be thought of as a simple generation-1 frame, with all components that are under compression when the frame is loaded with a small force, made up of scaled generation-1 frames. It is seen that all the scaled generation-1 subframes are under one of two loading conditions. For the component beams in the vertical subframes to be on the point of failure, using Eqs. (6.1, 6.2 and 6.7), their thicknesses must be given by:

$$t^{(0)} = \left(\frac{12 f_0}{\pi^2}\right)^{\frac{1}{3}} L_{2,0}, \tag{6.16}$$

$$t^{(1)} = \left(\frac{15\sqrt{5}}{2}\frac{f_0}{\pi^2}\right)^{\frac{1}{3}} L_{2,0}, \tag{6.17}$$

where $t^{(0)}$ and $t^{(1)}$ are the thicknesses of the central and end beams respectively (as shown in Fig. 6.2). Then, through stating that the central subframes must be on the point of failure, through use of Eqs. (6.1, 6.11, 6.10 and 6.16), $n_{2,1}$ is

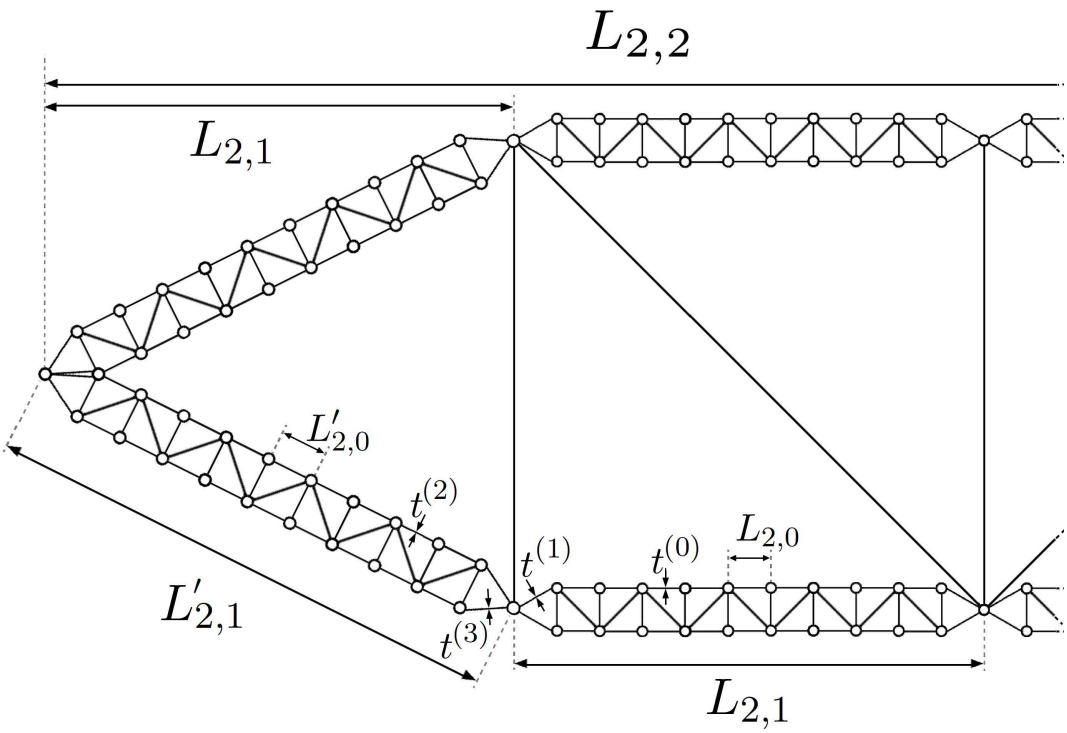


Figure 6.2: A section of the generation-2 frame and the parameters that describe it. Here the frame has been rotated through $\frac{\pi}{2}$ compared to Fig. 6.1.

found to be,

$$n_{2,1} = -2 + \sqrt{\frac{\pi^{4/3} 12^{1/3}}{4 f_0^{2/3}}}. \tag{6.18}$$

For the subframes connected directly to the loading points of the generation-2 frame two parameters are introduced: first $L'_{2,0}$ is the length of the shortest beams that make up the subframe and $n'_{2,1}$ is the number of unit cells that make up the subframe. Then, using Eqs. (6.1, 6.2 & 6.7), it is found that,

$$t^{(2)} = \left(\sqrt{\frac{5}{4}}\frac{12 f_0}{\pi^2}\right)^{\frac{1}{3}} \left(L'^2_{2,0} L_{2,0}\right)^{\frac{1}{3}}, \tag{6.19}$$

$$t^{(3)} = \left(\frac{75}{4}\frac{f_0}{\pi^2}\right)^{\frac{1}{3}} \left(L'^2_{2,0} L_{2,0}\right)^{\frac{1}{3}}. \tag{6.20}$$

By stating that the end frames must also be on the point of failure, and noting that $L_{2,1} = (n_{2,1} + 2)L_{2,0} = \frac{2}{\sqrt{5}}(n'_{2,1} + 2)L'_{2,0}$ it can be shown that,

$$n'_{2,1} = n_{2,1}. \tag{6.21}$$

Therefore, Eqs. (6.19 & 6.20) become:

$$t^{(2)} = t^{(1)}, \tag{6.22}$$

$$t^{(3)} = \left(\frac{375}{16}\frac{f_0}{\pi^2}\right)^{\frac{1}{3}} L_{2,0}. \tag{6.23}$$

Defining:

$$k_{2,0}^{(i)} = \frac{Yt^{(i)}}{L_{2,0}^{(i)}}, \tag{6.24}$$

as the spring constant for beams with thickness $t^{(i)}$, and denoting the spring constant for the central and end subframes as $k_{2,1}^{(0)}$ and $k_{2,1}^{(1)}$ respectively, it is found that,

$$k_{2,1}^{(i)} = \frac{12k_{2,0}^{(2i)}k_{2,0}^{(2i+1)}}{(4\sqrt{15} + \sqrt{3})k_{2,0}^{(2i)} + 12nk_{2,0}^{(2i+1)}}. \tag{6.25}$$

Given that,

$$L_{2,2} = (n_{2,2} + 2)L_{2,1}, \tag{6.26}$$

$$I_{2,2} = L_{2,1}^2 t, \tag{6.27}$$

$$F_{2,2} = 2F_{2,1}, \tag{6.28}$$

it can be shown that for the whole generation-2 structure to be on the point of failure,

$$n_{2,2} = n_{2,1}. \tag{6.29}$$

Setting the thickness of the end, horizontal beams of length $L_{2,1}$ such that the spring constant is equal to that of the end subframes, and all other beams of length $L_{2,1}$ or greater to have thickness $t_0$ it is possible to calculate the volume of a generation-2 frame. Defining $n \equiv n_{2,1} = n_{2,2}$,

$$\begin{aligned} v &= \frac{1}{2\ 2^{5/6}(2+n)4\pi^{2/3}} 3^{1/3} f_0^{1/3} \Bigg( \frac{120\sqrt{10}(2+n)2}{\sqrt{3}\left(20+\sqrt{5}\right)+30n} \\ &\quad + \left(2+3\sqrt{2}\right) n \left(5+4\sqrt{5}n\right) + 4(2+n)\left(-\sqrt{2}+\left(2+\sqrt{2}\right)n\right) \\ &\quad + \sqrt{2}\left(5\left(4+\sqrt{5}\right)+4\left(10+\sqrt{5}\right)n\right)\Bigg). \end{aligned} \tag{6.30}$$

Using Eqs. (6.3, 6.6, 6.7, 6.10, 6.26 - 6.28), it is found that,

$$f = \frac{16}{\pi^{4/3}12^{1/3}} f_0^{5/3}. \tag{6.31}$$

Thus, it is seen that, to leading order,

$$v \sim f^{3/5}. \tag{6.32}$$

which shows a further gain in efficiency when compared to the generation-1 structure in the limit of light loading.

### 6.1.4 Generation-$n$

The generation-$n$ structure can be created using an iterative process. The generation-2 spaceframe is created by taking a generation-1 frame and replacing all

beams that are under compression when the frame is lightly loaded with scaled generation-1 frames. This procedure is repeated to get to higher order structures. The generation of the structure, $G$, is defined as the number of iterations of this procedure that have taken place. It can be shown that for the central subframes at each hierarchical level:

$$L_{G,i} = (n_{G,i} + 2)L_{G,i-1}, \tag{6.33}$$

$$I_{G,i} = 2^{i-2}L_{G,i-1}^2 t, \tag{6.34}$$

$$F_{G,i} = 2F_{G,i-1}. \tag{6.35}$$

It can be seen that in a generation-$n$ structure there will be a set of beams under compression when the frame is initially loaded with a small compressive load. Setting,

$$n_{G,i} = -2 + \sqrt{\frac{\pi^{4/3}12^{1/3}}{4f_0^{2/3}}} \quad 1 \leq i \leq G, \tag{6.36}$$

for all frames regardless of $i$ and position in the frame, these beams will have lengths within the set $\{L_{G,0}^{(n)}\}$ where,

$$L_{G,0}^{(n)} = \left(\frac{\sqrt{5}}{2}\right)^n L_{G,0} \quad 0 \leq n \leq G, \tag{6.37}$$

where $L_{G,0}$ is the minimum length of all beams. Each simple beam of length $L_{G,0}^{(n)}$ will take the loading of:

$$F_{G,0}^{(n)} = \left(\frac{\sqrt{5}}{2}\right)^n F_{G,0}, \tag{6.38}$$

where $n$ takes the same value as in Eq. (6.37). It can therefore be shown that for every beam under compressive loading to be on the point of failure,

$$t^{(n)} = \left(\frac{\sqrt{5}}{2}\right)^n \left(\frac{12 f_0}{\pi^2}\right)^{\frac{1}{3}}. \tag{6.39}$$

Furthermore, through use of Eqs. (6.33 - 6.36, 6.37, 6.39), it is found that this puts all (sub)frames on the point of failure. It can then be shown that,

$$\begin{aligned} V(G) &= (2n+5)^{G-1}\left(\left(3+\sqrt{2}\right)n+4\right)L_{G,0}t^{(0)} + \sum_{i=1}^{G-1}\left(2\sqrt{5}\right)^{G-i} 2 s_{G,i} L_{G,i} \\ &+ \sum_{i=0}^{G-1}\left(2n+2\sqrt{5}\right)^{G-i-1}\left(\left(1+\sqrt{2}\right)n-1\right)L_{G,i}t^{(0)}, \end{aligned} \tag{6.40}$$

where $s_{G,i}$ is the thickness of the simple beams connected to the end frames such that the two have an equal spring constant. It can be shown that, for all $G > 1$,

$$f = 2^G \left(\frac{4}{\pi^{4/3} 12^{1/3}}\right)^{\frac{G}{2}} f_0^{1+\frac{G}{3}}. \tag{6.41}$$

Then, through use of Eq. (6.4, 6.33 - 6.36, 6.39, 6.40) it is seen that, to leading order,

$$v \sim f^{\frac{G+1}{G+3}}, \tag{6.42}$$

which shows in the limit of small $f$, increasing the hierarchical order of the structure leads to an increase in efficiency. In Fig. 6.3 a log-log plot of $v$ against $f$ is shown for generation-0 to 4.

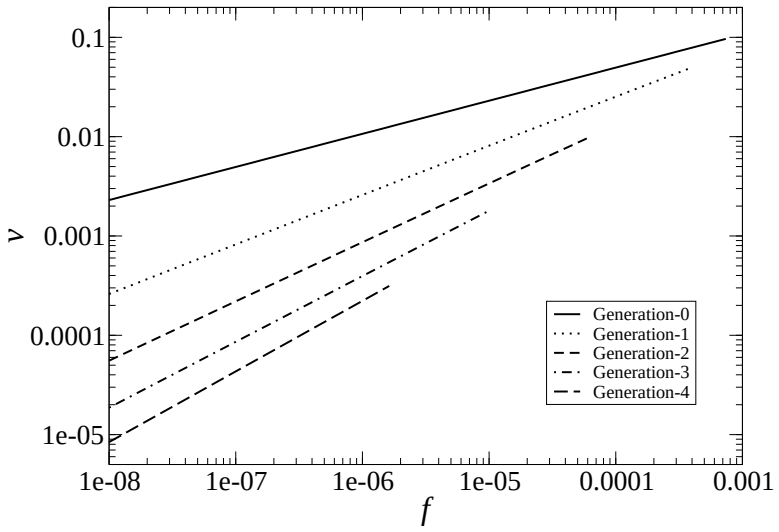


Figure 6.3: Non-dimensional volume against loading parameter for generation-0 to 4 designs shown on a log-log scale.

## 6.2 Imperfections in hierarchical frame

### 6.2.1 Analytic

#### Generation-1

Here the simplest imperfection is modelled, a single beam's thickness is perturbed from $t$ to $t + \Delta t$. The perturbed beam will be the vertical beam half way up the length of the frame with nodes at $(-\frac{L_{1,1}}{2}, \frac{L_{1,1} \pm L_{1,0}}{2})$, assuming $n$ is odd.

In the limit of small loading, the perturbed beam will experience a load of $\frac{F_{1,1}}{2}$ and have a spring constant different from all vertical beams in the frame. Thus, asymmetry will be introduced into the deformation of the frame. Globally, this deformation can be modelled as:

$$y^0_{1,1}(x) = \begin{cases} \frac{2a_{1,1}x}{L_{1,1} - \frac{L_{1,0}}{2}} & \text{if } 0 < x < \frac{L_{1,1}}{2} - \frac{L_{1,0}}{2} \\ a_{1,1} & \text{if } \frac{L_{1,1}}{2} - \frac{L_{1,0}}{2} < x < \frac{L_{1,1}}{2} + \frac{L_{1,0}}{2} \\ 2a_{1,1} - \frac{2a_{1,1}x}{L_{1,1} + \frac{L_{1,0}}{2}} & \text{if } \frac{L_{1,1}}{2} + \frac{L_{1,0}}{2} < x < L_{1,1}, \end{cases} \tag{6.43}$$

where,

$$a_{1,1} = \left( \frac{L_{1,1} - L_{1,0}}{2} - \frac{F_{1,1}\left(4\sqrt{15} + \sqrt{3}\right) k_{1,0}^{(0)} + 6k_{1,0}^{(1)}\left(n_{1,1} + 1\right)}{24 k_{1,0}^{(0)} k_{1,0}^{(0)}} \right) \frac{\Delta L_{1,0}}{2}, \quad (6.44)$$

$\Delta L_{1,0}$ is the difference in length between the perturbed beam and its unperturbed counterpart given by,

$$\Delta L_{1,0} = \frac{F_{1,0}\Delta k}{k_{1,0}^{(0)}\left(k_{1,0}^{(0)} + \Delta k\right) L_{1,0}}, \quad (6.45)$$

and $\Delta k$ is the change in spring constant associated with perturbing the beam by an amount $\Delta t$. Assuming that $L_{1,0} \ll L_{1,1}$, this deformation of the entire

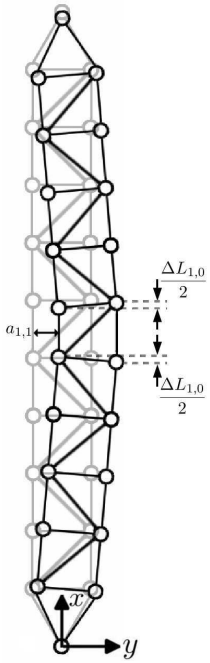


Figure 6.4: The triangular shaped deflection of a generation-1 frame caused by the weakening of the beam half way up the frame on the left, or, equivalently, strengthening of the beam half way up the frame on the right.

spaceframe can be approximated as an infinite Fourier series [80]:

$$y^0_{1,1} = \frac{8a_{1,1}}{\pi^2}\sum_{k=0}^{\infty}(-1)^k\frac{\sin((2k+1)\frac{\pi x}{L_{1,1}})}{(2k+1)^2} \qquad k \in \mathbb{Z}. \tag{6.46}$$

If the bar is then subject to a further compressive force, $F_{1,1}$, the deflection of the bar will be given by,

$$y_{1,1} = y^0_{1,1} + y^1_{1,1}. \tag{6.47}$$

where $y^1_{1,1}$ is the deformation caused by the further compression of the frame. The deflection $y^1_{1,1}$ is governed by the differential equation [21]:

$$YI_{1,1}\frac{d^2y_{1,1}}{dx^2} = -F_{1,1}(y^0_{1,1} + y^1_{1,1}). \tag{6.48}$$

Following the analysis of Timoshenko [21], it can be shown that the deformation due to compression takes the form:

$$\begin{aligned} y^1_{1,1} &= \frac{F_{1,1}}{F^c_{1,1}}\frac{8a_{1,1}}{\pi^2}\left(\frac{1}{1-\frac{F_{1,1}}{F^c_{1,1}}}\sin\left(\frac{x\pi}{L_{1,1}}\right) - \frac{1}{49}\frac{1}{3^2-\frac{F_{1,1}}{F^c_{1,1}}}\sin\left(\frac{3\pi}{L_{1,1}}\right) + \cdots\right) \\ &= A_{1,1}\sin\left(\frac{\pi x}{L_{1,1}}\right) - \cdots . \end{aligned} \tag{6.49}$$

It is seen that in the region of $F_{1,1} \approx F^c_{1,1}$ the series in Eq. (6.49) is dominated by the first term in the expansion. The nature of the bifurcation with the critical point at the Euler buckling load is known as a stable-symmetric bifurcation [81]. This is where, due to the imperfection, there is no point of failure analogous to the critical point of Euler buckling for the perfect spaceframe of length $L_{1,1}$ but instead the deflection increases rapidly as the Euler load is approached and subsequently passed.

Eq. (6.49) shows that as the Euler limit is approached, a curvature is induced

in the frame. This leads to a difference in arc length between the inner and outer beams in the spaceframe. The contribution to shortening of the inner beam due to curvature alone can be calculated, from this the extra load on that beam can be inferred. Failure of the frame is defined as the loading at which one of the (perfect) component, simple beams reach the Euler buckling limit with contributions from curvature included. The radius of curvature of the generation-1 frame, $R_{1,1}$, can be seen to obey,

$$\Theta_{1,1} R_{1,1} = L_{1,0} \tag{6.50}$$

$$\Theta_{1,1} \left( R_{1,1} - \frac{L_{1,0}}{2} \right) = L_{1,0} - \Delta L^B_{1,0}, \tag{6.51}$$

for some $\Theta_{1,1}$, where $\Delta L^B_{1,0}$ is the change in end-to-end length of the perturbed beam that is induced by the bowing of the generation-1 frame (assuming $\Delta t < 0$, if $\Delta t > 0$ this reduction in length is associated with the perfect beam opposite the perturbed beam in the structure). The radius of curvature is related to lateral displacement of the frame by:

$$\frac{1}{R_{1,1}} = \frac{|y''_{1,1}|}{\left(1 + y'^2_{1,1}\right)^{\frac{3}{2}}} \approx |y''_{1,1}|. \tag{6.52}$$

It is observed that the radius of curvature will be minimal at $x = 0.5L$; thus, the maximal value of $\Delta L^B_{1,0}$ can be related to $A_{1,1}$ through the expression:

$$\Delta L^B_{1,0} = \frac{L^2_{1,0} A_{1,1} \pi^2}{2 L^2_{1,1}}. \tag{6.53}$$

The failure of the whole frame can be seen to occur when the length of any component beam reaches the value

$$L^c_{1,0} = L_{1,0} - F^c_{1,0}/k_{1,0}, \tag{6.54}$$

where $F^c_{1,0}$ is the Euler load of the beam subjected to loading $F_{1,0}$ in the perfect frame

Including contributions from compression due to the Hookean behaviour and the compression effect of the global bowing, it can be shown that if $A_{1,1}$ exceeds a critical value, the frame will fail due to Euler buckling of the central beams. This critical value is given by the expression:

$$A^c_{1,1} = \frac{2L^2_{1,1}}{\pi^2 L^2_{1,0}} \left( \frac{\pi^2 (t^{(0)})^2}{12 L_{1,0}} - \frac{F_{1,0}}{k_{1,0}} \right). \tag{6.55}$$

Through equating the coefficient of $\sin\left(\frac{\pi x}{L}\right)$ in Eq. (6.49) and Eq. (6.55) the loading at failure of the generation-1 beam with a single imperfection can be calculated. The evolution of $A_{1,1}$ predicted by Eq. (6.49) is plotted in Fig. 6.5 against loading for various imperfection magnitudes, also shown is the figure is the critical value of $A_{1,1}$ given in Eq. (6.55).

The above analysis is only valid however for the case where the failure loading is very close to the Euler loading limit of the spaceframe. If $\Delta t$ is large enough

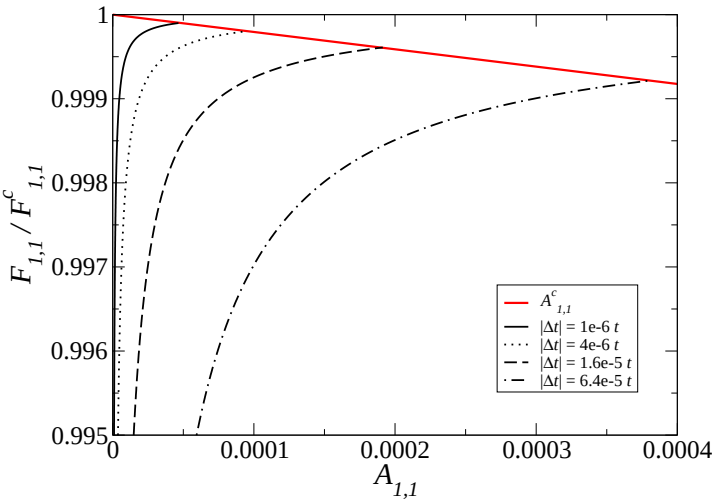


Figure 6.5: Showing the evolution of $A_{1,1}$ as predicted by Eq. (6.49) along with its critical value, from Eq. (6.55). The particular frame shown is optimised such that $n_{1,1} = 101$

(and negative), it should be found that failure occurs before the global deformation contributes significantly to the stress experienced by the perturbed beam. Failure in this case will simply follow the Euler load of the simple beam with a decreased width $t - |\Delta t|$. An important prediction of this analysis is that any asymmetric perturbation of a component beam, be it decreasing or increasing the thickness, will lead to a decrease in overall failure load of the composite structure.

Plotted in Fig. 6.6 is the value of the loading parameter at which a particular frame will fail against the magnitude of imperfection for both $\Delta t > 0$ and $\Delta t < 0$. Defining $\Lambda = 1 - \frac{F_{1,1}}{F^c_{1,1}}$ and $\xi = \frac{\Delta t}{t}$, it can be seen that for optimised frame, independent of loading for which the frame is optimised,

$$\Lambda = \kappa_{1,1}\, \xi^{0.50}, \tag{6.56}$$

where the error in the power of $\xi$ is $\pm 0.02$.

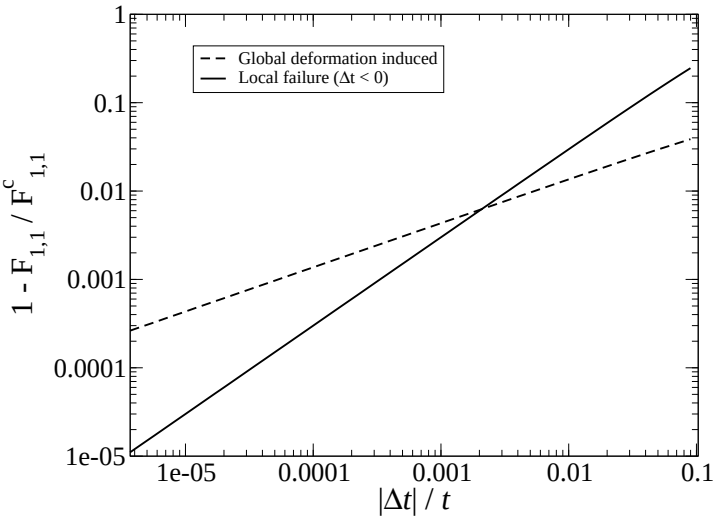


Figure 6.6: Effect of a perturbation to one central beam for a particular frame ($n = 51$). It is expected that for $\Delta t > 0$ the failure loading will always be induced by global deformation of the frame while for $\Delta t < 0$, for small $\Delta t$ global deflection will dominate while for larger $\Delta t$ the local failure mode will dominate.

### Generation-2

Here the effect of perturbing a single central beam in a generation-2 frame is established. The perturbed beam is placed at a point half way up the generation-2 frame with nodes at $\left(-\frac{L_{2,1}+L_{2,0}}{2}, \frac{L_{2,2}\pm L_{2,0}}{2}\right)$ (assuming $n$ is odd). On loading, the generation-1 subframe that contains the imperfection will deform from its initial straight configuration into a triangular wave whose deflection is given by,

$$y^0_{2,1}(x') = \begin{cases} \frac{2a_{2,1}x'}{L_{2,1}-L_{2,0}} & \text{if } 0 < x' < \frac{L_{2,1}}{2} - \frac{L_{2,0}}{2} \\ a_{2,1} & \text{if } \frac{L_{2,1}}{2} - \frac{L_{2,0}}{2} < x' < \frac{L_{2,1}}{2} + \frac{L_{2,0}}{2} \\ 2a_{2,1} - \frac{2a_{2,1}x'}{L_{2,1}+L_{2,0}} & \text{if } \frac{L_{2,1}}{2} + \frac{L_{2,0}}{2} < x' < L_{2,1} \end{cases}, \tag{6.57}$$

where $x'$ is related to the global coordinate system by, $x' = x + \frac{L_{2,1}+L_{2,0}}{2}$ and $y^0_{2,1}$ is the lateral displacement of the imperfect generation-1 frame relative to the initial, straight, configuration. The value of $a_{2,1}$ is found to be,

$$a_{2,1} = \left(\frac{L_{2,1}-L_{2,0}}{2} - \frac{F_{2,1}(4\sqrt{15}+\sqrt{3})k^{(0)}_{2,0} + 6k^{(1)}_{2,0}\left(n_{2,1}+1\right)}{24k^{(0)}_{2,0}k^{(1)}_{2,0}}\right)\frac{\Delta L_{2,0}}{2}, \tag{6.58}$$

where,

$$\Delta L_{2,0} = \frac{\Delta k_{2,0}F_{2,0}}{2k\left(k^{(0)}_{2,0} + \Delta k_{2,0}\right)L_{2,0}}. \tag{6.59}$$

It is straightforward to see that a displacement of the beam from Eq. (6.57) will cause a difference in the end-to-end length of the imperfect frame and its perfect counterpart. This difference is found to be:

$$\Delta L_{2,1} = \left(n_{2,1}+1\right)L_{2,0} - 2\sqrt{\left(\frac{n_{2,1}+1}{2}L_{2,0}\right)^2 - a^2_{2,1}} + \frac{F_{2,0}}{k_{2,0}}\left(1 - \frac{2k_{2,0}+\Delta k}{k_{2,0}\left(k_{2,0}+\Delta k\right)}\right). \tag{6.60}$$

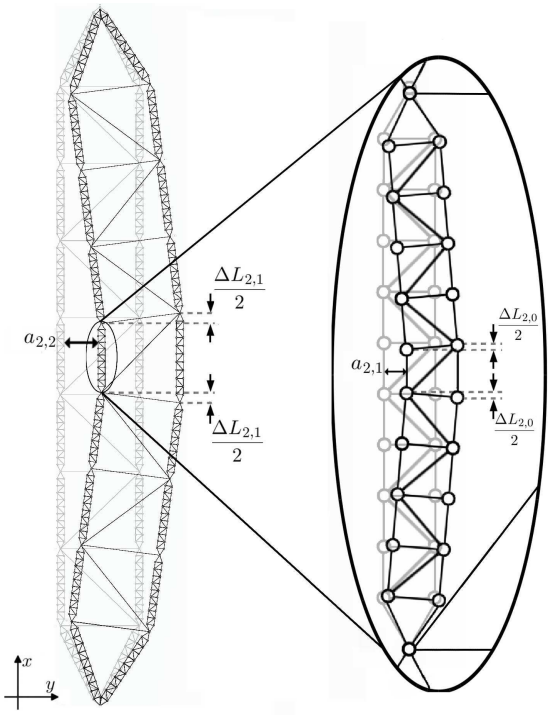


Figure 6.7: The deformation for the early stages of loading for the generation-2 frame. The perturbed beam is the simple beam half way up the enlarged generation-1 subframe on the left hand side (assuming $\Delta t < 0$).

The first two terms in Eq. (6.60) are due to the lateral displacement of the imperfect frame while the latter term is due to the central square unit cell deforming into a trapezium under loading. As shown in Fig. 6.7, a difference in end-to-end length in the central generation-1 subframes will lead to a global deflection in the generation-2 frame. This deflection will take the form:

$$y^0_{2,2}(x) = \begin{cases} \frac{2a_{2,2}x}{L_{2,2}-L_{2,1}} & \text{if } 0 < x < \frac{L_{2,2}}{2} - \frac{L_{2,1}}{2} \\ a_{2,2} & \text{if } \frac{L_{2,2}}{2} - \frac{L_{2,1}}{2} < x < \frac{L_{2,2}}{2} + \frac{L_{2,1}}{2} \\ 2a_{2,2} - \frac{2a_{2,2}x}{L_{2,2}+L_{2,1}} & \text{if } \frac{L_{2,2}}{2} + \frac{L_{2,1}}{2} < x < L_{2,2} \end{cases}, \tag{6.61}$$

where,

$$a_{2,2} = \left( \frac{L_{2,2} - L_{2,1}}{2} - \frac{F_{2,2}((4\sqrt{15} + \sqrt{3})k^{(0)}_{2,1} + 6(n_{2,2}+1)k^{(1)}_{2,1})}{24k^{(0)}_{2,1}k^{(1)}_{2,1}} \right) \frac{\Delta L_{2,1}}{2L_{2,1}}. \tag{6.62}$$

As in the case of generation-1 imperfect beam, if $L_{2,2} \ll L_{2,1}$ this can be approximated as a series:

$$y^0_{2,2} = \frac{8a_{2,2}}{\pi^2} \sum_{k=0}^{\infty} (-1)^k \frac{\sin((2k+1)\frac{\pi x}{L_{2,2}})}{(2k+1)^2}. \qquad k \in \mathbb{Z} \tag{6.63}$$

When the frame is loaded further, the evolution of this displacement will be governed by:

$$YI_{2,2}\frac{d^2 y_{2,2}}{dx^2} = -F_{2,2}(y^0_{2,2} + y^1_{2,2}). \tag{6.64}$$

As with the generation-1 frame, an expression showing the dependence of the displacement of the frame on the loading parameter can be obtained; a series solution analogous to Eq. (6.49) is found:

$$\begin{aligned} y^1_{2,2} &= \frac{F_{2,2}}{F^c_{2,2}} \frac{8a_{2,2}}{\pi^2} \left( \frac{1}{1 - \frac{F_{2,2}}{F_{2,2^c}}} \sin\left(\frac{\pi x}{L_{2,2}}\right) - \frac{1}{49} \frac{1}{3^2 - \frac{F_{2,2}}{F^c_{2,2}}} \sin\left(\frac{3\pi}{L_{2,2}}\right) + \cdots \right) \\ &= A_{2,2} \sin\left(\frac{\pi x}{L_{2,2}}\right) - \cdots . \end{aligned} \tag{6.65}$$

In the vicinity of $F_{2,2} \approx F^c_{2,2}$ this expansion will be dominated by the first term.

The evolution of the lateral displacement given in Eq. (6.65) is such that as $F_{2,2}$ approaches its critical value, a curvature is induced in the frame. As discussed in the previous section, this curvature causes an increased load to be exerted on the generation-1 subframes on the inside of the curvature. This can result in the failure of the perfect generation-1 frames around the imperfect subframe. The imperfect subframe does not exhibit a critical point on its fundamental path, however, when the first term in Eq. (6.65) dominates over latter terms the generation-1 imperfect subframe will itself exhibit a sinusoidal displacement. As seen in the previous section, this sinusoidal displacement of the generation-1 subframe acts

to increase the loading on the central vertical beams. The value of $A_{2,2}$ that implies failure of the perfect subframes towards the centre of the generation-2 frame will now be derived before comparisons with the value of loading on the imperfect subframe which results in failure of the component beams.

It is straightforward to show that the radius of curvature of the global deformation, $R_{2,2}$, using same approximation as in Eq. (6.52), is related to $A_{2,2}$ by,

$$\frac{1}{R_{2,2}} = \frac{\pi^2 A_{2,2}}{L_{2,2}^2}. \tag{6.66}$$

To obtain the decrease in end-to-end length of the generation-1 subframe on the inside of the curved generation-2 frame due to global curvature only (denoted $L_{2,1}^B$) it is observed that,

$$\Theta_{2,2} R_{2,2} = L_{2,1} \tag{6.67}$$

$$\Theta_{2,2}\left(R_{2,2} - \frac{L_{2,1}}{2}\right) = L_{2,1} - \Delta L_{2,1}^B, \tag{6.68}$$

for some value of $\Theta_{2,2}$. Combining Eqs.(6.66-6.68) it is seen that,

$$\Delta L_{2,1}^B = \frac{\pi^2 L_{2,1}^2 A_{2,2}}{2L_{2,2}^2}. \tag{6.69}$$

For large $n_{2,2}$, the generation-1 substructures in the vicinity of the imperfect generation-1 substructure will experience a compression close to that of the generation-1 imperfect substructure calculated above. These generation-1 substructures will however exhibit a critical point on their fundamental path under loading. There will therefore be a critical point for $A_{2,2}$ analogous to that calculated for the generation-1 structure in the previous section. A bound for this

value is found to be:

$$A^c_{2,2} = \frac{2L^2_{2,2}}{\pi^2 L^2_{2,1}} \left( \frac{\pi^2 Y t^{(0)} L^2_{2,0}}{2k^{(0)}_{2,1} L^2_{2,1}} - \frac{F_{2,1}}{k^{(0)}_{2,1}} \right) \tag{6.70}$$

Assuming that the generation-1 frame exhibits behaviour close to that of a linear spring, and in the limit $A_{2,2} \ll 1$ it can be assumed that the loading on the imperfect subframe is,

$$\frac{F_{2,2}}{2} + \Delta L^B_{2,1} k^{(0)}_{2,1}. \tag{6.71}$$

Thus given the loading on a imperfect generation-2 frame, through Eq. (6.65) the value of $A_{2,2}$ can be predicted. If $A_{2,2}$ reaches the value given in Eq. (6.70) failure of the perfect generation-1 subframes occurs. Given the value of $A_{2,2}$ the loading on the generation-1 imperfect subframe can be found through by Eqs. (6.69) and (6.71). Given this value of loading, using the results of the previous section, it can be predicted when the bowing of the generation-1 imperfect subframe will cause failure of its component beams. Both of these failure modes, along side simple failure of the perturbed component beam (assuming $\Delta t < 0$) are shown in Fig. 6.8.

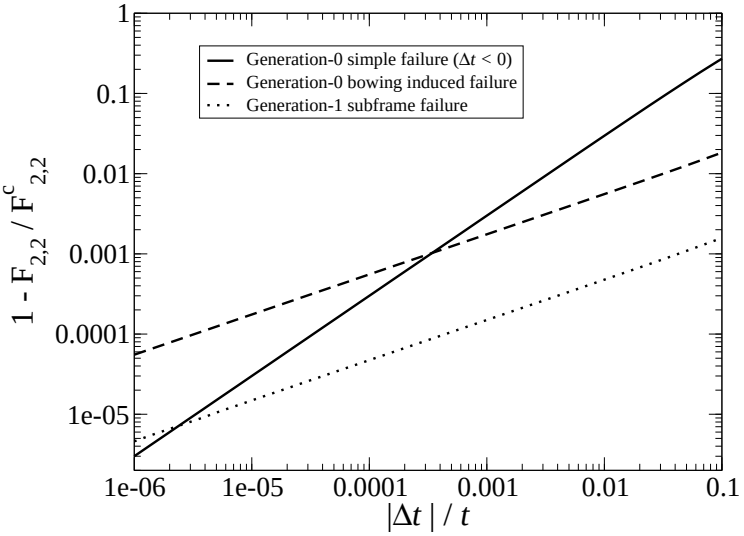


Figure 6.8: Loading at failure for a particular imperfect generation-2 frame ($n_{2,2} = n_{2,1} = 101$) against magnitude of imperfection. Shown is simple failure of weakened beam ($\Delta t < 0$), the point at which $A^c_{2,1}$ is reached (labelled generation-0 bowing induced failure) and the point of loading at which $A^c_{2,2}$ is reached (labelled generation-1 subframe failure). This particular plot is shown for $\Delta t < 0$, for $\Delta t > 0$ the functional dependence remains the same however the generation-0 bowing induced failure is translated a small amount towards increased stability.

### 6.2.2 Simulations

For finite values of $n_{1,1}$, Eq. (6.11) will not be exact. This causes the local and global failure modes to be non-coincident in the loading procedure leading to deviations from the behaviour described above. In this section, results of finite element simulations are shown against the theoretical predictions. The simulations are undertaken using the spherical arc-length method (see references [62, 63] or appendix B). Without exception, freely hinged joints are assumed at the nodes within the structure. Only generation-1 structures are investigated through simulation due to increased computational requirements for higher generations.

Eq. (6.11) becomes more accurate in the limit of large $n_{1,1}$. When $n_{1,1}$ is relatively small, it is found that this formula overestimates the stability against global buckling when compared to the results of finite element simulation. The value of $A^c_{1,1}$, as given in Eq. (6.55), is independent of $F^c_{1,1}$ and thus, $A^c_{1,1}$ is not altered by any inaccuracy in Eq. (6.11). However, the evolution of $A_{2,2}$ as predicted in Eq. (6.49), is changed considerably by any such inaccuracy. This is summarised in Fig. 6.9 where the evolution of $A_{1,1}$ found through simulation is shown for a frame optimised such that $n_{1,1} = 51$. The critical point found by simulation is 0.59% less than that predicted by Eq. (6.11). The evolution of $A_{1,1}$ can however, still be predicted by Eq. (6.49) through substitution of the critical value of the frame found through simulation in place of $F^c_{1,1}$ in Eq. (6.49), this is also shown in Fig. 6.9.

The power-law relating imperfection to reduction in failure load can be tested through simulation. As above, the inaccuracy in Eq. (6.11) must be taken into account. Through substitution of the critical point found through simulation in place of $F^c_{1,1}$ in Eq. (6.49) and subsequently equating the expression with Eq. (6.55), the failure load of a given frame with a given imperfection can be

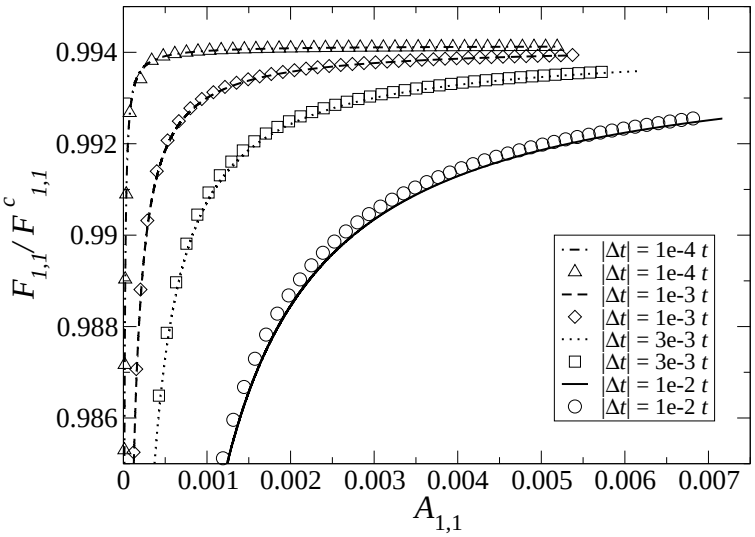


Figure 6.9: Showing agreement between analytic prediction and simulation results for the evolution of the deformation in a frame with $n = 51$. $F^c_{1,1}$ refers to that found through use of Eq. (6.11), the critical point of the generation-1 frame is seen to be predicted to be greater through use of this equation compared to finite element simulations. Plotted with lines are the analytic predictions for the evolution of the coefficient of the first term in Eq.(6.49) with increasing load, with symbols the results of simulation for the displacement of the central point of the frame in the $x$-direction.

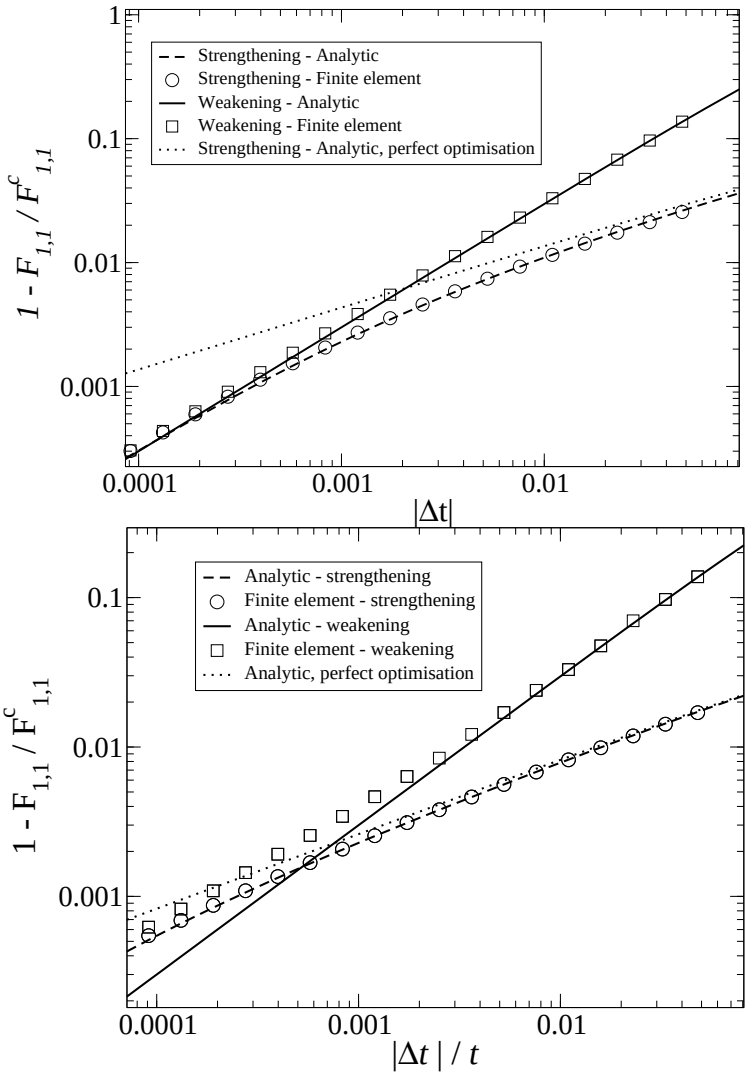


Figure 6.10: The agreement between analytic predictions for the change in failure loading against the results of finite element simulations. Also shown is the analytic result assuming Eq. (6.11) is exact. Above: the results for $n_{1,1} = 51$. Below: results for $n_{1,1} = 143$; for greater values of $n_{1,1}$ it is seen the half power-law has an increased range of validity.

predicted; this can then be tested against simulation. The results of both the corrected theory and simulation are shown in the upper plot of Fig. 6.10 alongside those predictions which are valid for coincident global and local failure mode for a frame optimised such that $n_{1,1} = 51$. Strong agreement between theory and simulation for both signs of $\Delta t$ is observed. Below in Fig. 6.10, the predictions made by analytic work and the results of finite element for a frame optimised such that $n_{1,1} = 143$ are shown; in particular it is seen, as a result of the increasing accuracy of Eq. (6.11), the half power-law has a greater range of validity.

## 6.3 Discussion

It has been shown that the principle of hierarchical design can be applied to a structure in 2-dimensions. As in 3-dimensions, increasing the hierarchical order of the structure can be seen to result in higher efficiency in the limit of low loading. The effect of a perturbation to a single, central beam in the structure has been obtained theoretically for generation-1 and 2. It is found that the behaviour of the generation-1 subframe dominates the effect of the imperfection in the generation-2 frame. This behaviour is expected to apply to 3-dimensional frames that display imperfection-insensitive behaviour at the critical point of loading. In both generation-1 and 2 of the 2 dimensional frame, a half power-law relating imperfection magnitude to reduction in loading at failure is found. It is found that any asymmetric perturbation in the frame, be it strengthening or weakening the perturbed beam, results in a reduction in loading at failure. The results of analytic work in the case of generation-1 frames are confirmed through finite element work. The effect of inaccuracies in the optimisation proceedure is also discussed.

# Chapter 7

# Conclusions and further work

Conclusions from Chapters 2-6 are summarised here.

Firstly, in Chapter 2 it was shown that through adding lateral support to a simply supported buckling beam the buckling load can be increased. It was shown that in the limit of small support strength, a single, delta function distribution is optimal. Increasing the cost of support sees a series of bifurcation events as the support distribution splits in a non-trivial manner. The first bifurcation event was analysed in detail, and it was found that there are similarities between this splitting and that found in Landau second-order phase transitions. The limit of high allowable support is to be investigated in further work.

In Chapter 3 fractal designs for high mechanical efficiency optimised to withstand a given external pressure were presented. It was shown that the scaling of material required for stability can be systematically varied through changing the generation of the structure. In the limit of low applied pressure, the optimal generation increases and the structure becomes fractal. Fractal dimensions of optimal structures were found for a range of pressures.

Chapter 4 has shown that the geometry of an adhesive interface has a large role to play in determining the force required for separation of two materials.

In particular the interface between one infinitely stiff material and a deformable surface was investigated. It was found that for a given interaction strength, the scaling of force required to separate the two materials can be manipulated through changing the hierarchical order of the interface. In future, higher generations of interface are to be investigated as should the more general problem of two deformable surfaces joined by a given interaction strength.

In Chapter 5 an example hierarchical frame was fabricated through rapid prototyping techniques before being mechanically tested. The results for one material (R05) agree particularly well with finite element work. Mechanism maps were presented illuminating the optimisation technique. Also presented in Chapter 5 was a design based on the same geometry as the fabricated design but instead constructed from hollow tubes; this was shown to yield further efficiency benefits. Further work could illuminate the effect of rigid joints in the structure through finite element work. It is also of interest to experimentally validate the scaling argument of material required for stability against loading on the structure.

Finally in Chapter 6 a 2-dimensional hierarchical frame was described. Again, in the limit of low loading it was shown that increasing the hierarchical order of the structure results in higher efficiency frames. The effect of a perturbation to a single beam thickness was investigated for the generation-1 and 2 structures. It was found that the scaling of the reduction in loading at failure against imperfection magnitude was the same for the generation-1 and 2 structures despite the increase in complexity of the structure. Further work should investigate the possible co-operative effect of imperfections in a structure and statistical investigations into the failure distributions against imperfection magnitude should be undertaken.

# Appendix A

# Alternative derivation for cylinder scaling

In Chapter 3 it was found that a fractal design is highly mechanically efficient for withstanding a given external pressure. Here a more intuitive derivation for the scaling relationship between volume required to make a stable structure under a given pressure will be given for the case of a cylinder. In order to clarify the procedure, only the scaling will be found, the numerical pre-factors can be obtained either through this method or that presented in Chapter 3.

## A.1 Generation-2

The volume of the generation-2 cylinder scaled by the volume it encloses can be shown to scale as:

$$v_c \sim \frac{t_{2,1}}{r_{2,2}}, \tag{A.1}$$

where $\sim$ is taken to mean 'scales as'. Given Eq. (3.17) and taking the values of $\alpha_{2,2} = \frac{\pi}{4}$ and $\alpha_{2,1}$ to be given in Eq. (3.23), the scaling for the two upper limits

for non-dimensional pressure ($p \equiv P/Y$) before failure due to crushing of the surfaces found to be:

$$p \sim \frac{t_{2,1} r_{2,1}^2}{r_{2,2}^3}, \tag{A.2}$$

$$p \sim \frac{t_{2,1}^3}{r_{2,1}^3}, \tag{A.3}$$

Then, setting the values of $r_{G,m}$ such that failure occurs for both levels simultaneously, it can be shown that:

$$\frac{r_{2,1}}{r_{2,2}} \sim \left(\frac{t_{2,1}}{r_{2,1}}\right)^{\frac{2}{3}}. \tag{A.4}$$

Then, it is seen,

$$\frac{t_{2,1}}{r_{2,2}} = \frac{t_{2,1}}{r_{2,1}} \frac{r_{2,1}}{r_{2,2}} \sim \left(\frac{t_{2,1}}{r_{2,1}}\right)^{1+\frac{2}{3}}. \tag{A.5}$$

Thus, from Eq. (A.3) or (A.2),

$$p \sim \frac{t_{2,1}}{r_{2,2}}^{\frac{9}{5}} \sim v^{\frac{9}{5}}, \tag{A.6}$$

or,

$$v \sim p^{\frac{5}{9}}. \tag{A.7}$$

It can be shown that the same scaling is obtained when using the equation for crush pressure at the lower hierarchical level.

## A.2 Higher Generations

In general, the volume of material used in creating a generation-$n$ structure, scaled by the volume it encloses, scales as,

$$v \sim \frac{t_{G,1}}{r_{G,G}}. \tag{A.8}$$

For the largest lengths scale, there is only one mode of failure, crush pressure of the whole cylinder. At all lower levels, there are two modes of failure: crush pressure of the exposed diamond surfaces and hoop stresses leading to short wavelength failure. The scaling of crush pressure against geometric properties of the design is the same at all length scales ($m > 1$). For $m > 1$ and $m = 1$ it is found that the upper limits for applied external pressure while retaining stability under crush pressure are given by,

$$p \sim \frac{t_{G,1} r_{G,m-1}^2}{r_{G,m}^3} \quad \text{for } 2 \leq m \leq G, \tag{A.9}$$

$$p \sim \frac{t_{G,1}^3}{r_{G,1}^3}. \tag{A.10}$$

As described in the Chapter 3, through the symmetry of the system, there is a hoop stress that will be exerted on the cylinder walls. As stated this will be assumed to be supported by the cylindrical substructures running circumferentially around the cylinder walls. It is found that each of the substructures have to support a force that will scale as,

$$F_{G,m} \sim P r_{G,G} r_{G,m}. \tag{A.11}$$

Then, as shown previously, this leads to the restrictions on $p$:

$$p \sim \frac{t_{G,1} r_{G,m-1}}{r_{G,G} r_{G,m}}, \tag{A.12}$$

$$p \sim \frac{t_{G,1}^2}{r_{G,G} r_{G,1}}. \tag{A.13}$$

Assuming at the larger length scales - for all cylinders of radius $r_{G,k+1}$ and over - the active mode of failure is the crush pressure and for all cylinders with radius $r_{G,k}$ and below the active mode of failure local failure through hoop stresses, it can be shown:

$$\frac{r_{G,m}}{r_{G,m-1}} \sim \left(\frac{r_{G,m-1}}{r_{G,m}}\right)^{\frac{2}{3}} \quad \text{for } k+1 \leq m \leq G-1, \tag{A.14}$$

$$\frac{r_{G,k}}{r_{G,k+1}} \sim \left(\frac{r_{G,k-1}}{r_{G,k}}\right)^{\frac{1}{2\left(\frac{2}{3}\right)^{G-k}}}, \tag{A.15}$$

$$\frac{r_{G,m}}{r_{G,m+1}} \sim \frac{r_{G,m-1}}{r_{G,m}} \quad \text{for } 2 \leq m \leq k-1, \tag{A.16}$$

$$\frac{r_{G,1}}{r_{G,2}} \sim \frac{t_{G,1}}{r_{G,1}}. \tag{A.17}$$

Thus, combining all the above, it can be shown that:

$$\frac{t_{G,1}}{r_{G,G}} = \frac{t_{G,1}}{r_{G,1}} \prod_{i=1}^{G-1} \frac{r_{G,i}}{r_{G,i+1}} \sim \left(\frac{t_{G,1}}{r_{G,1}}\right)^{k-1+\left(\frac{3}{2}\right)^{G-k}}. \tag{A.18}$$

As stated in the main body of this thesis, the crossover $k$ for the cylinder is found to be $G-2$ and therefore it is seen,

$$v \sim p^{1-\frac{4}{1+4G}}. \tag{A.19}$$

# Appendix B

# Spherical Arc-Length method

In this appendix the spherical arc-length method of finite element simulations is briefly described, for a more complete discussion see references [62, 63].

This method follows the path of equilibrium for a structure as loading increases. Each step along the equilibrium path is restricted to have a given arc-length with contributions from both loading and displacement. The method begins at one point on the fundamental path and a predictor step is used to calculate an estimate for where the next step will be. In general, this predictor step does not lie on the path of equilibrium and a measure how far out of equilibrium the system would be in this configuration is taken. Then a series of corrector steps are taken to minimise the out of equilibrium measure.

## B.1 Predictor step

The applied external load vector on a given structure is defined as $\boldsymbol{q_e}$, also defined is a scalar variable, $\lambda$ which describes the load level. The load applied to a structure is therefore given by $\lambda \boldsymbol{q_e}$. The set of displacements such that the structure is in equilibrium under this load is given by $\boldsymbol{d}$; the corresponding set

of internal forces in the structure are given by $\boldsymbol{q_i}$ (which, for equilibrium to be satisfied is equal to $\lambda \boldsymbol{q_e}$). For a small increment $\Delta \boldsymbol{d}$ a Taylor series about $\boldsymbol{d}$ can be obtained:

$$\boldsymbol{q_i}(\boldsymbol{d} + \Delta \boldsymbol{d}) = \boldsymbol{q_i}(\boldsymbol{d}) + \frac{\partial \boldsymbol{q_i}(\boldsymbol{d})}{\partial \boldsymbol{d}} \Delta \boldsymbol{d} + O(\Delta \boldsymbol{d}^2). \tag{B.1}$$

Assuming perfect equilibrium at both the initial configuration corresponding to displacements $\boldsymbol{d}$ and the final configuration with displacements $\boldsymbol{d}+\Delta \boldsymbol{d}$ it is found,

$$\boldsymbol{q_i}(\boldsymbol{d} + \Delta \boldsymbol{d}) - \boldsymbol{q_i}(\boldsymbol{d}) = \boldsymbol{q_e}(\boldsymbol{d} + \Delta \boldsymbol{d}) - \boldsymbol{q_e}(\boldsymbol{d}) = \Delta \boldsymbol{q_e}. \tag{B.2}$$

Defining $\boldsymbol{K_t} \equiv \frac{\partial \boldsymbol{q_i}(\boldsymbol{d})}{\partial \boldsymbol{d}}$ as the tangent stiffness matrix, and combining Eqs. (B.1 & B.2),

$$\Delta \boldsymbol{q_e} = \boldsymbol{K_t} \Delta \boldsymbol{d}. \tag{B.3}$$

If the simulation begins on a point on the equilibrium path $(\boldsymbol{d_k}, \lambda_k)$ and it is desired for the load on the structure to be incremented by an amount $\Delta\lambda_1$, using the above equation an initial predictor step for the displacement along the path of equilibrium as can be estimated as:

$$\Delta \boldsymbol{d_1} = \Delta\lambda_1 \boldsymbol{K_t}^{-1} \boldsymbol{q_e}, \tag{B.4}$$

for compatibility with later notation this is denoted $\delta \boldsymbol{d_0^I} = \boldsymbol{K_t}^{-1} \boldsymbol{q_e}$. Using this method, the arc-length of any step is set to a predefined value, here, this is denoted $\Delta l$. In general the arc-length, $\Delta S$, is defined by:

$$\Delta S^2 \equiv (\Delta \boldsymbol{d})^T \Delta \boldsymbol{d} + (\Delta\lambda)^2 \psi^2 \boldsymbol{q_e}^T \boldsymbol{q_e} = \Delta l^2, \tag{B.5}$$

where $\psi$ is introduced to scale the contributions from displacement and load in the simulations. It is seen that for $\psi \to 0$ the arc-length is dominated by the contributions from displacement, while for $\psi \to \infty$ the arc length is dominated by load. Then, given the tangent stiffness matrix at a point on the equilibrium path and a set value of $\Delta l$ one can compute the initial displacement and load increments as:

$$\Delta\lambda_1 = \pm\frac{\Delta l}{\sqrt{(\delta \boldsymbol{d_0^I})^T(\delta \boldsymbol{d_0^I}) + \psi^2 \boldsymbol{q_e^T q_e}}}, \tag{B.6}$$

$$\Delta \boldsymbol{d} = \Delta\lambda_1 \delta \boldsymbol{d_0^I}. \tag{B.7}$$

The criterion used by Crisfield [63] to resolve the sign of the above equation is,

$$\text{sign}(\Delta\lambda_1) = \text{sign}(\det(\boldsymbol{K_t})). \tag{B.8}$$

## B.2 Corrector step

It is possible that the point $(\boldsymbol{d_k} + \Delta \boldsymbol{d_1}, \lambda_k + \Delta\lambda_1)$ will not lie on the equilibrium path. In general, if the structure is not in equilibrium there will be a difference between the internal loads in the structure and the external applied loads. For a displacement $\boldsymbol{d}$ and load parameter $\lambda$, this can be quantified as:

$$\boldsymbol{r}(\boldsymbol{d}, \lambda) = \boldsymbol{q_i}(\boldsymbol{d}) - \lambda \boldsymbol{q_e}, \tag{B.9}$$

where $\boldsymbol{r}$ is referred to as the out of balance vector.

For a particular step in displacement $\Delta \boldsymbol{d_i}$ and corresponding change in loading $\Delta\lambda_i$, it can be seen that:

$$a_i = (\Delta \boldsymbol{d_i})^T \Delta \boldsymbol{d_i} + \Delta\lambda_i^2 \psi^2 \boldsymbol{q_e}^T \boldsymbol{q_e} - \Delta l^2 = 0. \tag{B.10}$$

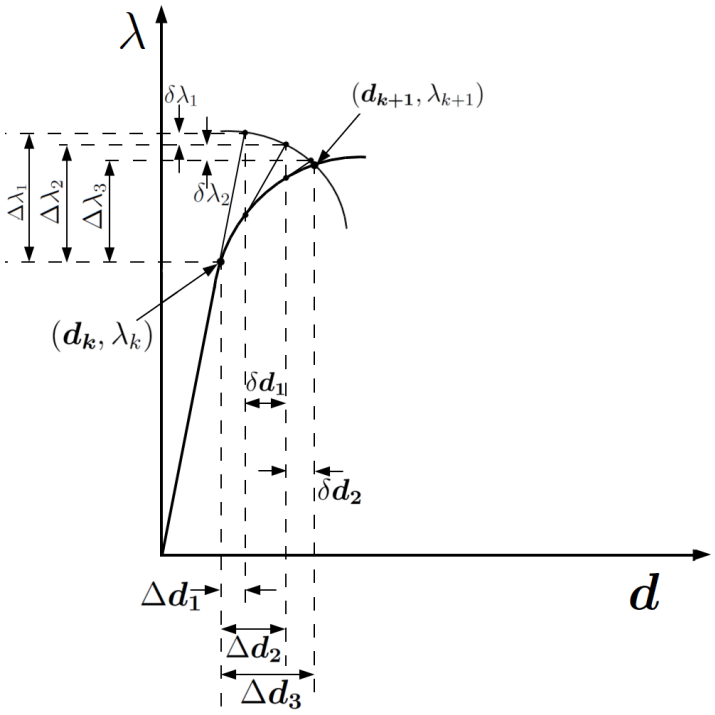


Figure B.1: Schematic of the correcting procedure used in the finite element simulation. Step shown starts at $(\lambda_k, \boldsymbol{d_k})$ and ends within a given tolerance of $(\lambda_{k+1}, \boldsymbol{d_{k+1}})$.

Then, taking truncated Taylor series of Eqs. (B.9 & B.10), one obtains,

$$\begin{aligned} \boldsymbol{r_{i+1}} &= \boldsymbol{r_i} + \frac{\partial \boldsymbol{r}}{\partial \boldsymbol{d}}\delta\boldsymbol{d_i} + \frac{\partial \boldsymbol{r}}{\partial \lambda}\delta\lambda \\ &= \boldsymbol{r_i} + \boldsymbol{K_t}\delta\boldsymbol{d_i} - \boldsymbol{q_e}\delta\lambda_i = 0, \qquad \text{(B.11)} \\ a_{i+1} &= a_i + \frac{\partial a}{\partial \boldsymbol{d}}\delta\boldsymbol{d_i} + \frac{\partial a}{\partial \lambda}\delta\lambda_i \\ &= a_i + 2(\Delta\boldsymbol{d_i})^T\delta\boldsymbol{d_i} + 2\Delta\lambda_i\delta\lambda_i\psi^2\boldsymbol{q_e}^T\boldsymbol{q_e}. \qquad \text{(B.12)} \end{aligned}$$

Then, combining these equations, one can obtain,

$$\begin{pmatrix} \delta\boldsymbol{d_i} \\ \delta\lambda_i \end{pmatrix} = - \begin{pmatrix} \boldsymbol{K_t} & -\boldsymbol{q_e} \\ 2(\Delta\boldsymbol{d}_i^T & 2\Delta\lambda_i\psi^2\boldsymbol{q_e}^T\boldsymbol{q_e} \end{pmatrix}^{-1} \begin{pmatrix} \boldsymbol{r_i} \\ a_i \end{pmatrix}. \qquad \text{(B.13)}$$

Considering Eq. (B.11) it can be shown that,

$$\delta \boldsymbol{d_i} = -\boldsymbol{K_t}^{-1}\boldsymbol{r_i} + \delta\lambda_i \boldsymbol{K_t}^{-1}\boldsymbol{q_e}, \tag{B.14}$$

this can be rewritten as:

$$\delta \boldsymbol{d_i} = \delta \boldsymbol{d_i^{II}} + \delta\lambda_i \delta \boldsymbol{d_i^{I}}, \tag{B.15}$$

where,

$$\delta \boldsymbol{d_i^{II}} = -\boldsymbol{K_t}^{-1}\boldsymbol{r_i}, \tag{B.16}$$

$$\delta \boldsymbol{d_i^{I}} = \boldsymbol{K_t}^{-1}\boldsymbol{q_e}. \tag{B.17}$$

Then all the quantities in the incremental procedure,

$$\Delta \boldsymbol{d_{i+1}} = \Delta d_i + \delta \boldsymbol{d_i} \tag{B.18}$$

$$\Delta\lambda_{i+1} = \Delta\lambda_i + \delta\lambda_i, \tag{B.19}$$

are known with the exception of $\delta\lambda_i$. The constraint that the arc-length is always equal to $\Delta l$ gives us:

$$(\Delta \boldsymbol{d_{i+1}})^T \Delta \boldsymbol{d_{i+1}} + \lambda_{i+1}^2 \psi^2 \boldsymbol{q_e}^T \boldsymbol{q_e} = (\Delta \boldsymbol{d_i})^T \Delta \boldsymbol{d_i} + \lambda_i^2 \psi^2 \boldsymbol{q_e}^T \boldsymbol{q_e} = \Delta l^2. \tag{B.20}$$

Substitution of Eq. (B.15) in the above equation yields a quadratic in $\delta\lambda_i$. This is found to be,

$$c_1(\delta\lambda_i)^2 + c_2\delta\lambda_i + c_3 = 0 \tag{B.21}$$

where,

$$c_1 = (\Delta \boldsymbol{d_i})^T \Delta \boldsymbol{d_i} + \psi^2 \boldsymbol{q_e}^T \boldsymbol{q_e} \tag{B.22}$$

$$c_2 = 2(\delta \boldsymbol{d_i})^T (\Delta \boldsymbol{d_i} + \delta \boldsymbol{d_i^{II}}) + 2\Delta\lambda_i \psi^2 \boldsymbol{q_e}^T \boldsymbol{q_e} \tag{B.23}$$

$$c_3 = (\Delta \boldsymbol{d_i} + \delta \boldsymbol{d_i^{II}})^T (\Delta \boldsymbol{d_i} + \delta \boldsymbol{d_i^{II}}) - \Delta l^2 + (\Delta\lambda_i)^2 \psi^2 \boldsymbol{q_e}^T \boldsymbol{q_e} \tag{B.24}$$

Then, in the case of two real solutions from the above equation, the vector $\Delta \boldsymbol{d_{i+1}}$ is found for both values of $\delta\lambda$ and the root which corresponds to the solution which minimises the angle between $\Delta \boldsymbol{d_i}$ and $\Delta \boldsymbol{d_{i+1}}$ is taken. This process is incremented until convergence is found.

# Bibliography


[1] J. E. Gordon, *The Science of Structures and Materials.* New York, 1988.

[2] R. Chadwich, *First Civilizations, Ancient Mesopotamia and Ancient Greece.* Equinox Publishing Ltd, 2005.

[3] G. Galilei, *Dialoghi delle due nuove scienze (Dialogues Concerning Two New Sciences).* 1638.

[4] L. Euler *Mem. Acad. Sci. Berlin*, vol. 13, no. 252, 1759.

[5] J. E. Gordon, *Structures.* Penguin Group, 1978.

[6] R. Lakes *Nature*, vol. 361, pp. 511–515, 1993.

[7] J. Aizenberg, J. C. Weaver, M. S. Thanawala, V. C. Sundar, D. E. Morse, and P. Fratzl *Science*, vol. 309, pp. 275–278, 2005.

[8] E. Baer, A. Hiltner, and H. D. Keith *Science*, vol. 235, pp. 1015–1022, 1987.

[9] N. M. Hancox, *Biology of Bone.* Cambridge University Press, 1972.

[10] C. on Synthetic Hierarchical Structures, C. on Engineering & Techincal Systems, and N. R. Council, *Hierarchical Structures in Biology as a Guide for New Materials Technology.* National Academy Press, 1994.

[11] P. Podsiadlo, E. M. Arruda, E. Kheng, A. M. Waas, L. J., K. Critchley, E. Chuang, A. K. Kaushik, H.-S. Kim, Y. Qi, S.-T. Noh, and N. A. Kotov *ACS Nano*, vol. 3, pp. 1564–1572, 2009.

[12] R. Lakes *Science*, vol. 235, pp. 1038–1040, 1987.

[13] M. M. Sundaram and G. K. Anantasuresh *Resonance*, vol. 14, pp. 849–865, 2009.

[14] B. Mandelbrot, *The Fractal Geometry of Nature*. Freeman, New York, 1983.

[15] Marshak, ed., *Perspectives in Modern Physics: Essays in Honor of Hans Bethe*. Wiley Interscience, New York, 1966.

[16] M. M. Mikulas Tech. Rep. 78687, NASA, 1978.

[17] R. S. Farr and Y. Mao *EPL*, vol. 84, no. 14001, 2008.

[18] B. Wu *Mechanics Research Communications*, vol. 25, no. 4, pp. 479–486, 1998.

[19] N. Olhoff and Åkesson *Structural Optimisation*, vol. 3, pp. 163–175, 1991.

[20] J. M. Klitchieff *Quart. Journ. Mech. and Applied Math.*, vol. 2, no. 3, pp. 257–262, 1949.

[21] S. P. Timoshenko and J. M. Gere, *Theory of Elastic Stability*. McGraw Hill, 1986.

[22] D. Bojczuk and Mróz *Structural Optimisation*, vol. 16, pp. 47–57, 1998.

[23] B. Wu *Mechanics Research Communications*, vol. 23, no. 1, pp. 29–34, 1996.

[24] R. S. Farr *Phys. Rev. E*, vol. 76, no. 056608, 2007.

[25] R. S. Farr *Phys. Rev. E*, vol. 76, no. 046601, 2007.

[26] T. W. Murphey and J. D. Hinkle *American Institute of Aeronautics and Astronautics*, no. 1903, 2003.

[27] B. Budiansky *International Journal of Solids and Structures*, vol. 36, pp. 3677–3708, 1999.

[28] J. M. T. Thompson and G. W. Hunt, *Elastic Instability Phenomena*. John Wiley & Sons, Chichester, UK, 1984.

[29] V. Tvergaard *Int. J. Solids Structures*, vol. 9, pp. 176–192, 1976.

[30] S. Kamat, B. R. Su, X., and A. H. Heuer *Nature*, vol. 405, pp. 1036–1040, 2000.

[31] B. L. Smith, T. E. Schäffer, M. Viani, J. B. Thompson, N. A. Frederick, A. Belcher, D. E. Stucky, G. D. Morse, and P. K. Hansma *Nature*, vol. 399, pp. 761–763, 1999.

[32] C. C. Pollitt *Clinical Tehcniques in Equine Practice*, vol. 3, pp. 3–21, 2004.

[33] S. M. Sarratt and D. M. Hood *AJVR*, vol. 66, no. 2, pp. 227–283, 2005.

[34] L. Landau and E. M. Lifschitz, *Course of Theoretical Physics*, vol. 4. Pergamon Press, 1994.

[35] D. J. Rayneau-Kirkhope, R. S. Farr, K. Ding, and Y. Mao *Physics Letters A*, vol. 375, pp. 67–72, 2010.

[36] M. J. Feigenbaum *J. Stat. Phys.*, vol. 1, no. 25, 1978.

[37] J. A. Pérez-Carlos, F. Olóriz, and P. Palmqvist *LETHIA*, vol. 40, pp. 253–272, 2007.

[38] C. A. Long *J. Morphology*, vol. 185, pp. 185–195, 1985.

[39] J. M. García-Ruiz, A. Checa, and P. Rivas *Paleobiology*, vol. 16, pp. 349–354, 1990.

[40] F. Olóriz, P. Palmqvist, and Pérez-Claros *LETHIA*, vol. 30, pp. 191–204, 1997.

[41] P. D. Ward *Paleobiology*, vol. 6, no. 2, pp. 168–172, 1980.

[42] W. B. Saunders *Paleobiology*, vol. 21, no. 3, pp. 343–355, 1995.

[43] K. Ebel *LETHIA*, vol. 25, no. 2, pp. 179–193, 1992.

[44] R. A. Hewitt and G. E. G. Westermann *LETHIA*, vol. 30, no. 3, pp. 205–212, 1997.

[45] Y. Li, C. Ortiz, and M. C. Boyce *PRE*, vol. 85, no. 031901, 2012.

[46] T. von Karman, *Collected works.* Butterworth, London, 1956.

[47] S. B. Batdorf, M. Stein, and M. Schildcrout Technical Note 1346, NACA, 1945.

[48] C. A. Featherston and C. Ruiz *J. Mech. Eng. Sci. Proc.*, vol. 212, no. 183, 1998.

[49] W. T. Koiter. PhD thesis, Technische Hogeschool Delf, 1945.

[50] P. K. Wright, *21st Century Manufacturing.* Prentice Hall, 2000.

[51] K.-H. Lee and G.-J. Park *Comput. Struct.*, vol. 79, p. 77, 2001.

[52] H. Yao and H. Gao *Journal of the Mechanics and Physics of Solids*, vol. 54, pp. 1120–1146, 2006.

[53] G. Huber, M. Hubert, R. Solenak, K. Mecke, K. Jacobs, S. N. Gorb, and E. Arzt *PNAS*, vol. 102, no. 45, pp. 16293–16296, 2005.

[54] N. S. Pesika, H. Zeng, K. Kristiansen, B. Zhao, Y. Tian, K. Autmn, and J. Israelachvili *Journal of Physics: Condensed Matter*, vol. 21, no. 464132, 2009.

[55] H. Gao, X. Wang, H. Yao, S. Gorb, and E. Arzt *Mechanics of Materials*, vol. 37, pp. 175–185, 2005.

[56] K. Autumn, M. Sitti, Y. A. Liang, A. M. Peattie, W. R. Hansen, S. Sponberg, T. W. Kenny, R. Fearing, J. N. Israelachvili, and R. J. Full *Proc. Natl. Acad. Sci. USA*, vol. 19, pp. 12252–12256, 2002.

[57] K. Autumn and A. M. Peattie *Intergrative and Comparative Biology*, vol. 42, pp. 1081–1090, 2002.

[58] A. K. Geim, S. V. Dubonos, I. V. Grigorieva, K. S. Novoselov, A. A. Zhukov, and Y. Shapovl *Nature Materials*, vol. 2, pp. 461–463, 2003.

[59] B. Yurdumakan, N. R. Raravikar, A. M. Pulickel, and A. Dhinojwala *Chemical Communications*, vol. 30, pp. 3799–3801, 2005.

[60] A. J. C. Ladd, J. H. Kinney, and T. M. Breunig *PRE*, vol. 55, pp. 3271–3275, 1997.

[61] M. J. Paszek, D. Boettiger, V. M. Weaver, and D. A. Hammer *PLoS Computational Biology*, vol. 55, no. e1000604, 2009.

[62] E. Riks *Int. J. Solids Structures*, vol. 15, pp. 529–551, 1979.

[63] M. A. Crisfield *Computers and Structures*, vol. 13, pp. 55–62, 1981.

[64] M. A. Crisfield, *Finite Element Analysis of Solids and Structures.* John Wiley and sons, Ltd, England, 1991.

[65] J. McLaughlin and N. J. Wyshinski *Acta Arithmetica*, vol. 116, no. 1, pp. 63–79, 2005.

[66] J. Currey, *The Mechanical Adaptations of Bones*. Princeton, New Jersey, 1984.

[67] J. L. Katz *Biomech.*, vol. 4, pp. 455–473, 1971.

[68] K. Piekarski *J. App. Phys.*, vol. 41, pp. 215–223, 1970.

[69] G. W. Kooistra, V. Deshpande, and H. N. G. Wadley *J. App. Mech.*, vol. 74, pp. 259–268, 2007.

[70] R. Hague, S. Mansour, N. Saleh, and R. Harris *Journal of Material Science*, vol. 39, pp. 2457–2464, 2004.

[71] G. V. Salmoria, C. H. Ahrens, M. Fredel, V. Soldi, and A. T. N. Pires *Polymer Testing*, vol. 24, pp. 157–162, 2005.

[72] www.envisiontec.de, *EnvisionTEC R05 and RC25 (Nanocure) Techincal Data*. 22 November 2010.

[73] T. A. Schaedler, A. J. Jacobsen, A. Torrents, A. E. Sorensen, J. Lian, J. R. Greer, L. Valdevit, and W. B. Carter *Science*, vol. 334, 2011.

[74] A. J. Jacobsen, W. Barvosa-Carter, and S. Nutt *Advanced Materials*, vol. 19, pp. 3892–3896, 2007.

[75] N. Saleh, N. Hopkinson, R. J. M. Hague, and S. Wise *Rapid Prototyping Journal*, vol. 10, pp. 305–315, 2004.

[76] Y. Tsompanakis, N. D. Lagaros, and M. Papadrakakis, eds., *Structural Design Optmisation Considering Uncertainties*. Taylor & Francis, London, 2008.

[77] M. Ohsaki and K. Ikeda, *Stability and Opimistaion of Structures.* Springer, 2007.

[78] K. Ikeda, K. Murota, and I. Ilishakoff *Computers and Structures*, vol. 59, pp. 463–469, 1996.

[79] J. Roorda, *Buckling of Elastic Structures.* Solid Mechanics Division, University of Waterloo Press, 1980.

[80] K. F. Riley, M. P. Hobson, and S. J. Bence, *Mathematical Methods of Physics and Engineering.* Cambridge Univeristy Press, 1998.

[81] K. Ikeda and K. Murota, *Imperfect Bifurcation in Structures and Materials: Engineering Use of Group-Theoretic Bifurcation Theory.* Springer, 2002.